TECHNISCHE
UNIVERSITÄT
WIEN

GEO

MASTERARBEIT

VODCA2AGB - A novel approach for the estimation of global AGB stocks based on vegetation optical depth data and random forest regression

zur Erlangung des akademischen Grades

Master of Science

im Rahmen des Studiums

Geodäsie und Geoinformation

eingereicht von

Thomas Unterholzner BSc
Matrikelnummer 01526600

ausgeführt am Department für Geodäsie und Geoinformation
der Fakultät für Mathematik und Geoinformation
der Technischen Universität Wien

Betreuung
Betreuer: Univ.Prof. Dr.rer.nat. Wouter Arnoud Dorigo, MSc
Mitwirkung: Dipl.-Ing. Ruxandra Maria Zotta, Samuel Scherrer Msc

Wien, am 13. June 2023

_____   _____
(Unterschrift VerfasserIn)   (Unterschrift BetreuerIn)

Statement of authorship

I declare that I have written this thesis on my own and that information, which has been directly or indirectly taken from other sources, is cited accordingly. All stated information is in agreement with truth or fact to the best of my knowledge.

Vienna, Tuesday 13th June, 2023

Abstract

Aboveground biomass (AGB) plays an important role in the Earth's carbon cycle, both as a source and sink of carbon, and therefore its monitoring is critical in the fight against climate change.
In the past, several AGB maps on global and regional scales have been created to provide an estimate of stocks at a certain point in time. However, most of these maps are static and thus do not allow for monitoring the change in biomass.

As an alternative to current approaches, vegetation optical depth (VOD) could be used to monitor global AGB dynamically. VOD is a measure of the attenuation of microwave signals traveling through the vegetation canopy. It has a linear relationship with vegetation water content, which in turn is related to biomass and vegetation water status. Previous studies have already proven the feasibility of AGB estimation based on L-band VOD (L-VOD) using nonlinear univariate parametric regression approaches. However, due to the high complexity of the global AGB-VOD relationship, this approach might be better suited for regional AGB estimation.
To overcome this problem, a novel approach for global AGB estimation relying on multivariate non-parametric random forest regression (RF) was developed and tested. For this purpose, RF models were trained on an annual reference AGB product, and predictions were compared with a hold-out test set as well as an independent AGB map. The RF models rely on a set of different feature combinations, including data from VOD, leaf area index (LAI), land cover (LC) and sun induced fluorescence (SIF). The prediction accuracy was assessed via R^2 scores, with results ranging from 0.79 to 0.96 %. The largest increase in model performance was observed when land cover information was used in combination with VOD. Prediction accuracy was the lowest over dense and high vegetation, such as broadleaf evergreen forests, and conversely, the best results were achieved for sparse and low vegetation, like crops and shrubs, which is in line with previous studies. Overall, the thesis showed promising results for the future application of AGB estimation based on VOD and random forest regression.

Contents

List of Figures

List of Tables

1. Introduction

Monitoring of vegetation properties is vital for the understanding of water, carbon, and energy cycles (Rodríguez-Fernández et al., 2018). According to Denman et al. (2007), about 20 % of total anthropogenic carbon dioxide emissions in the 1990s were caused by land use change, mostly tropical deforestation. More recent estimates of relative carbon emissions from deforestation and forest degradation are lower (12 % of total emissions) (Werf et al., 2009). The reason for this is an increase in overall emissions due to increased fossil fuel combustion, while emissions from deforestation and forest degradation have remained relatively constant (Werf et al., 2009). Tropical forests alone are expected to emit 87 to 130 PgC between 2000 and 2100 under the assumption that the current rate of deforestation stays constant (Moutinho and Schwartzman, 2005). Land use and land cover change (LULCC) contributed approximately 1.4 (range: 0.4 to 2.3) PgC yr^{-1} and 1.6 (0.5 to 2.7) PgC yr^{-1} to the CO_2 emissions for the 1980s and 1990s, respectively (Denman et al., 2007). In the past two decades, the emissions declined slightly to 1.1 $\pm$ 0.7 PgC yr^{-1} for the period from 2011 to 2020 (Friedlingstein et al., 2010). As one can see from the above numbers, the uncertainty in the LULCC emissions is quite high, in fact, LULCC is the component with the highest uncertainty within the global carbon budget (Houghton et al., 2012). This uncertainty originates from ambiguities in the rates of deforestation and reforestation, as well as ambiguities in the carbon density of the land area affected by LULCC (Houghton et al., 2012).

Another source of uncertainty in the carbon budget is the possible positive effect of CO_2 fertilization. Increased atmospheric CO_2 concentrations can lead to increased levels of photosynthesis and plant growth, removing carbon from the atmosphere and storing it in terrestrial ecosystems (Walker et al., 2021). There is evidence for a positive carbon sink as a result of increased CO_2 concentrations (Walker et al., 2021). The magnitude of this carbon sink is however unclear (Walker et al., 2021).

To better assess the impact of the above-mentioned effects on the carbon budget, it is important to have a good overview of the carbon stored in vegetation. An important parameter in this regard is aboveground biomass (AGB), which is the biomass above ground consisting of stems, stumps, branches, seeds, bark and foliage (Liang and Wang, 2020a). AGB can be monitored through the use of remote sensing data (Baccini et al. (2012), Bouvet et al. (2018), Saatchi et al. (2011), Xu et al. (2021), Avitabile et al. (2016)).

Several AGB maps with varying spatial and temporal resolutions have been created using a set of different methods. Saatchi et al. (2011) used a combination of in-situ and satellite "Light Detection and Ranging" (LiDAR) data in conjunction with microwave and optical satellite imagery to create a "benchmark" map of biomass carbon stocks for the early 2000s.
Other maps using a combination of in-situ data, LiDAR and satellite imagery are the maps created by Baccini et al. (2012), Xu et al. (2021), and Avitabile et al. (2016), where the latter is a combination of the maps from Baccini et al. (2012) and Saatchi et al. (2011).
A different approach concerning the mentioned studies was taken by Bouvet et al. (2018) for the mapping of AGB in the savannas and woodlands of Africa. Contrary to the previously mentioned approaches, Bouvet et al. (2018) did not use optical LiDAR data and instead used a combination of

AGB estimates from field measurements and the 2010 L-band PALSAR mosaic created by JAXA. The AGB estimates were derived by relating radar backscatter to AGB, using a forward model, and subsequently inverting the model to get AGB estimates.

A common trait of the above-mentioned maps is their static nature, which makes dynamic AGB monitoring impossible. The only study that created a time series of AGB maps was Xu et al. (2021). Xu et al. (2021) proposed the application of a self-improving machine learning algorithm together with forest inventory, airborne laser scanning (ALS), and optical and microwave satellite data to create global AGB maps for the years 2000 to 2019. Even though the maps from Xu et al. (2021) already cover a longer time period and thus allow for dynamic AGB monitoring, alternative simpler approaches might be of interest.

A possible alternative to the maps of Xu et al. (2021) could be offered by AGB datasets based on vegetation optical depth (VOD), due to its high temporal resolution and the fact that it is almost unaffected by cloud cover (Moesinger et al., 2020). Previous studies have already achieved good results for VOD-based AGB estimation using "nonlinear univariate parametric regression" (Liu et al. (2015), Fan et al. (2019)). However, due to the complex global non-linear relationship between VOD and AGB, caused by different land cover types (Rodríguez-Fernández et al., 2018), other multivariate approaches might be better suited.
A commonly used multivariate nonlinear and nonparametric method is random forest regression (RF). A random forest is an ensemble method that fits a quantity of decision tree classifiers on different sub-samples of the dataset and applies averaging to increase the predictive accuracy and manage overfitting (Pedregosa et al., 2011). Results from previous studies indicate that RF is better suited to capture the complex global VOD-AGB relationship than simpler regression approaches (Schmidt et al., 2023).

1.1. Objective of this thesis

This thesis seeks to develop a novel approach for global AGB estimation by applying random forest regression models in combination with VOD and other remote sensing data. Furthermore, this work aims to compare the new approach to older already existing approaches relying on nonlinear univariate parametric regression.

Considering this, this thesis aims to answer the following questions: What is the relationship between individual VOD bands and different AGB reference datasets? How does the prediction performance of the univariate regression approach compare to the performance of the RF models? Which input features have the largest influence on the prediction performance? What are the strengths and weaknesses of the models depending on different land cover types?

2. Data

In this thesis, different types of data, including VOD, LAI, LC, SIF and AGB data were used (Table 1, Figure 1, 2, 3). LC was selected because it is related to the amount of AGB present in a given area, whereas LAI and SIF were used to include information about vegetation structure and function. The datasets were all resampled to a common resolution of 0.25° x 0.25° using averaging. All datasets except for Baccini and Avitabile-AGB (Baccini et al. (2012), Avitabile et al. (2016)) consist of yearly time series with varying temporal coverage (Table 1).

Dataset	Datatype	Spatial coverage	Temporal coverage	Data source	Temporal resolution	Parameter
VODCA	Microwave	Global	1987-2020	Moesinger et al. (2020)	Yearly	Vegetation optical depth (VOD)
VODCA v2: L-band	Microwave	Global	2010-2020	Zotta et al. (2023, in preparation)	Yearly	Vegetation optical depth (VOD)
Xu-AGB	Optical	Global	2000-2019	Xu et al. (2021)	Yearly	Aboveground biomass (AGB)
MODIS LAI	Optical	Global	2000-2020	Myneni, Knyazikhin, and Park (2015)	Yearly	Leaf area index (LAI)
ESA CCI LC	Optical	Global	2000-2020	ESA (2017)	Yearly	Plant functional types (PFTs)
SIF (SCIAMACHY, GOME-2)	Optical	Global	2002-2018	Wen et al. (2021)	Yearly	Sun induced fluorescence (SIF)
Baccini-AGB	Optical	Tropics+Subtropics	2002-2010	Baccini et al. (2012)	static	Aboveground biomass (AGB)
Avitabile-AGB	Optical	Tropics+Subtropics	1995-2010	Avitabile et al. (2016)	static	Aboveground biomass (AGB)

Table 1: Overview of the datasets used in this thesis.

2.1. Vegetation optical depth - VOD

Vegetation optical depth (VOD) is a measure of the attenuation of microwave signals while they travel through the vegetation canopy (Frappart et al., 2020). It can be retrieved from microwave measurements using both active and passive methods (Frappart et al., 2020) and has a linear relationship with vegetation water content (VWC, $kg \times m^{-2}$), which is linked to biomass and vegetation water status (Frappart et al., 2020).

In the past, L-band VOD (L-VOD) was used as input to regression models predicting AGB from VOD retrievals (Liu et al., 2015; Frappart et al., 2020). However, based on findings from Dou et al. (2023), multiple frequencies might be better suited for predicting AGB. The reason for using VOD products with multiple frequencies is the different interactions between vegetation and microwave radiation, depending on the frequency and vegetation type (Dou et al., 2023). L-band, for example, shows higher reliability for tree-dominated vegetation types, while the shorter X-band is better suited for shrublands (Dou et al., 2023).

Vegetation Optical Depth Climate Archive - VODCA

The Vegetation Optical Depth Climate Archive (VODCA) is a series of VOD products distinguished by their respective spectral bands (C-, X- and Ku-band) and temporal coverage (Moesinger et al., 2020). The products are created by combining VOD retrievals from different satellite sensors (TMI, SSM/I, AMSR-E, AMSR2 and Windsat) using the Land Parameter Retrieval Model (Schalie et al., 2017), which results in a VOD product with reduced noise compared to the input datasets (Moesinger et al., 2020). VODCA has a spatial resolution of 0.25° x 0.25° (Moesinger et al., 2020) and daily temporal resolution (Moesinger et al., 2019). For this thesis, the yearly average of VODCA was used as input for the models.

In addition to Ku, X, and C-band, a preliminary L-VOD product based on observations from the

"Soil Moisture Active Passive" (SMAP) and "Soil Moisture and Ocean Salinity" (SMOS) mission was used (Zotta et al., 2023, in preparation). This L-VOD is however not yet publicly available.

Furthermore, the yearly standard deviation, the 25% and 75% quantiles, and the variance of the VODCA products were also used as additional information for the models.

2.2. Aboveground biomass - AGB

Aboveground biomass (AGB) is the biomass consisting of stems, stumps, branches, seeds, bark, and foliage and is typically expressed in mass per unit area (like $Mgha^{-1}$ or kgm^{-2}) (Liang and Wang, 2020b).

For this thesis, AGB data from Xu et al. (2021), Baccini et al. (2012), and Avitabile et al. (2016) was used:

2.2.1. Xu-AGB

The dataset created by Xu et al. (2021) consists of yearly AGB maps spanning the period from 2000 to 2019. The maps were created using a self-improving machine learning algorithm (SIMLA) in conjunction with input data from forest inventories (mainly from the temperate and boreal regions), airborne laser scanning (ALS) data for tropical forests around the globe, satellite LiDAR inventory data containing the height structure of global vegetation and time series of microwave and optical satellite images for the years 2000 to 2019 (Xu et al., 2021). The ALS and forest inventory data were converted to above and belowground biomass by applying allometric models, which then were employed as training data for the SIMLA algorithm, to create biomass estimates from the microwave and optical satellite data (Xu et al., 2021). The method used by Xu et al. (2021) is in agreement with an Intergovernmental Panel on Climate Change (IPCC) Tier 3 approach for the estimation of carbon stock change (Xu et al., 2021).

2.2.2. Baccini-AGB

Baccini et al. (2012) predicted the carbon density (in Mg C ha^{-1}) of AGB across the tropics (tropical America, Africa and Asia) with a spatial resolution of 500 m. The maps were created using a combination of field data, spaceborne LiDAR data and multispectral satellite imagery (Baccini et al., 2012). According to Baccini et al. (2012), the overall mass of aboveground carbon in live woody vegetation across tropical Africa, America, and Asia is 64.5 (± 8.4), 117.7 (± 8.4), and 46.5 (± 3.0) Pg C, respectively. The confidence interval of the estimates is 95% (Baccini et al., 2012). On a national level Brazil, the Democratic Republic of Congo and Indonesia have the highest AGB estimates with 53.2, 22.0 and 18.6 Pg C, respectively (Baccini et al., 2012).

2.2.3. Avitabile-AGB

Avitabile et al. (2016) created a pan-tropical AGB map by combining the two AGB maps of Baccini et al. (2012) and Saatchi et al. (2011).

Saatchi et al. (2011) created a "benchmark" map of biomass carbon stocks, including all tropical forests, using a mix of field data, satellite LiDAR samples, and additional optical and microwave satellite images (Saatchi et al., 2011).

The fusion model used to create the combined map is buildt on bias removal and weighted linear averaging of the original two maps (Baccini-AGB, Saatchi-AGB), aiming to create an output map with higher accuracy than each of the respective input maps (Avitabile et al., 2016). The validation of the fused map showed a decrease of the root mean square error (RMSE) of 15-21% compared to the input maps (Avitabile et al., 2016), and even more important, almost unbiased estimates with a mean bias of 5 Mg dry mass per ha, compared to the bias of 21 and 28 Mg dry mass per ha of the Saatchi and Baccini maps, respectively (Avitabile et al., 2016).

2.3. Leaf area index - LAI

LAI is a measure for the quantity of leaf area per unit ground area (Chen and Cihlar, 1996). It gives information on the ground area covered with plants and is a crucial structural vegetation property (Liang and Wang, 2020a). Processes like canopy interception, evapotranspiration, and gross photosynthesis are proportional to it (Liang and Wang, 2020a).

MODIS-LAI

The LAI data for this thesis is obtained from the Moderate Resolution Imaging Spectroradiometer (MODIS) on board the Terra and Aqua satellites and consists of 8-day composite LAI images with a 500-meter pixel size (Myneni, Knyazikhin, and Park, 2015). However, for this thesis, the resolution was upscaled to 0.25° x 0.25° using averaging, and the yearly average was used subsequently. The LAI data from MODIS is created by making use of the information about vegetation structural types, sun-sensor geometry, as well as spectral information of MODIS red (648 nm) and near-infrared (NIR, 858 nm) (Myneni, Knyazikhin, and Park, 2015).

2.4. Plant functional types - PFTs

The PFT concept involves combining various characteristics of multiple plant species into a few functional groups, usually less than 15 (Poulter et al., 2011). These functional groups are identified based on their physiognomy, phenology type, climate zone, and photosynthetic pathway (Poulter et al., 2011). Each PFT is defined as a combination of growth form and leaf characteristics such as type (needle-leaved or broadleaved) and longevity (deciduous or evergreen) (Forkel et al., 2019). It allows for a fractional representation of plant coverage, for example, the PFT class Tree-BD represents the fractional coverage of broadleaf deciduous trees in a given pixel (Forkel et al., 2019).

ESA CCI-LC

The ESA CCI land cover product is part of the European Space Agency's Climate Change Initiative (ESA, 2017). The purpose of the ESA CCI project is to provide the next generation of geophysical parameters obtained from satellite observations, in conjunction with quantified uncertainties, in order to provide the possibility to check each parameter against the requirements of the Global Climate Observing System (GCOS) and the Climate Modelling Community (CMC) (ESA, 2017). A vital property of the ESA CCI LC maps is their consistency in time (ESA, 2017). To achieve this consistency, the annual LC maps are not created independently, but are obtained from a basis land cover map that is made with the help of the Medium Resolution Imaging Spectrometer (MERIS) FR and RR archive from 2003 to 2012 (ESA, 2017). FR stands for full resolution and RR for reduced resolution. The ESA CCI LC maps are most accurate for broadleaved evergreen forest, rainfed cropland, bare areas, permanent snow and ice, water bodies, and urban areas (Li et al., 2018). Classes like mosses and lichens, forests flooded with fresh water, and sparse vegetation have the lowest accuracies, as well as mosaic classes of natural vegetation (Li et al., 2018). One of the key priorities of the ESA CCI LC maps was the improved description of LC characteristics regarding PFT model requirements (ESA, 2017). For this purpose, LC-PFT conversion tables were generated for different climate zones (ESA, 2017).

2.5. Sun Induced Fluorescence - SIF

Sun induced fluorescence is the part of the solar radiation that is re-emitted by vegetation (Schlau-Cohen and Berry, 2015). The effect of fluorescence is caused by excitation effects and has emission peaks located at 685 and 730 nm (Joiner et al., 2013). The remaining fractions of the incoming radiation are either used for photosynthesis or dispersed as heat (Schlau-Cohen and Berry, 2015). Measuring fluorescence across wide areas can give information about the gross primary production (GPP) of vegetation (Schlau-Cohen and Berry, 2015).

SIF from SCIAMACHY and GOME-2

The sun induced fluorescence (SIF) data from Wen et al. (2021) is a monthly global dataset with a pixel size of 0.05° x 0.05°. The SIF (740 nm) data is obtained from the Global Ozone Monitoring Experiment 2 (GOME-2) instruments on the Metop-A satellite and the Scanning Imaging Absorption Spectrometer for Atmospheric Cartography (SCIAMACHY)(Wen et al., 2021). The initial data retrieved from the GOME-2 instruments and SCIAMACHY is downscaled to the 0.05° x 0.05° pixel size by applying a random forest algorithm, and subsequently, a harmonization of the data was performed using a cumulative distribution function (CDF) (Wen et al., 2021). The product has high spatial and temporal consistency with the original 740 nm SIF data from SCIAMACHY and GOME-2 (Wen et al., 2021). For this thesis, the SIF data were downsampled to a 0.25° x 0.25° pixel size and the yearly average was used subsequently.
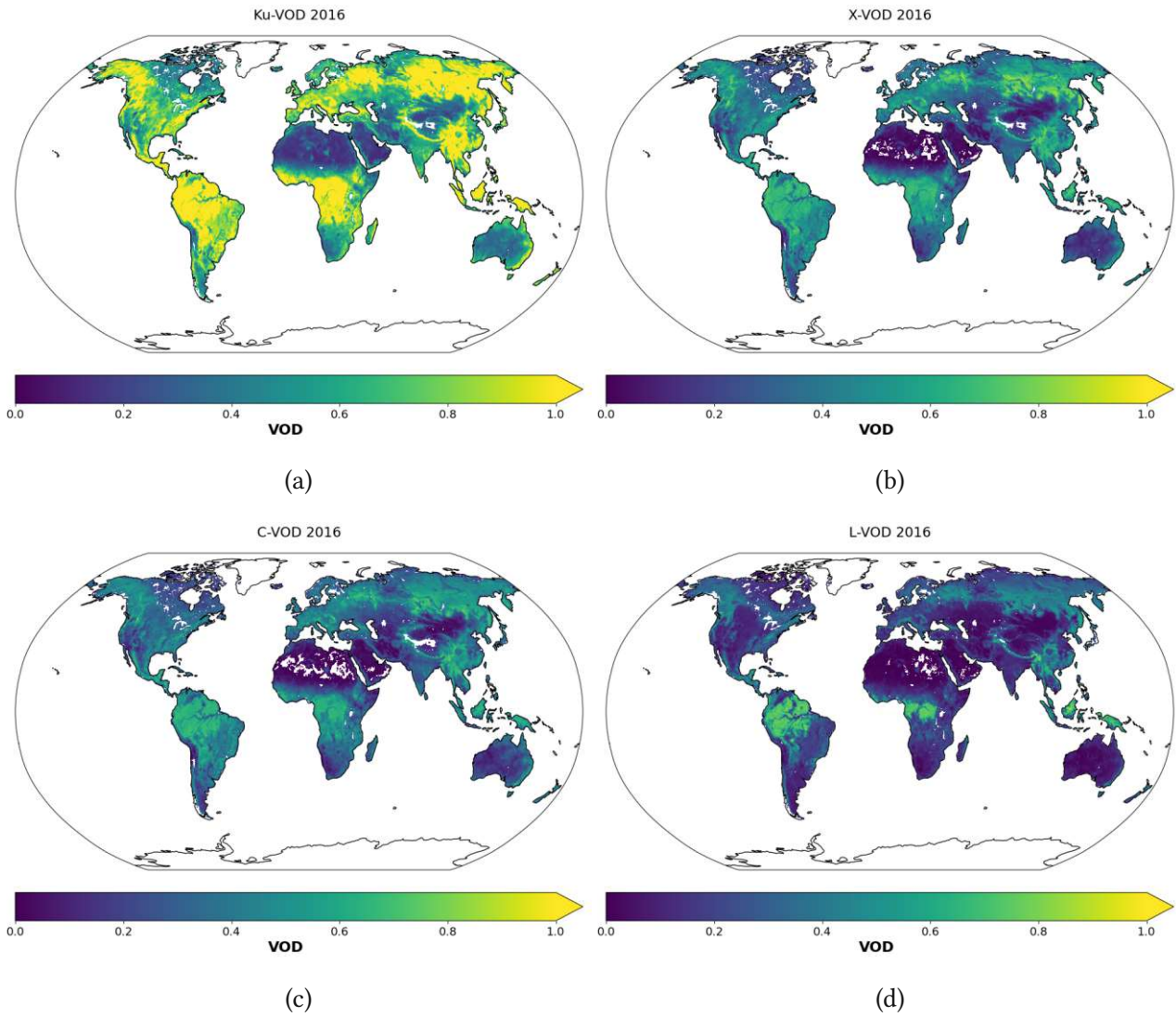
Figure 1: Yearly means of the different frequency bands of the VODCA dataset (Moesinger et al., 2020) for the year 2016. a) Ku-band, b) X-band, c) C-band, d) L-band.
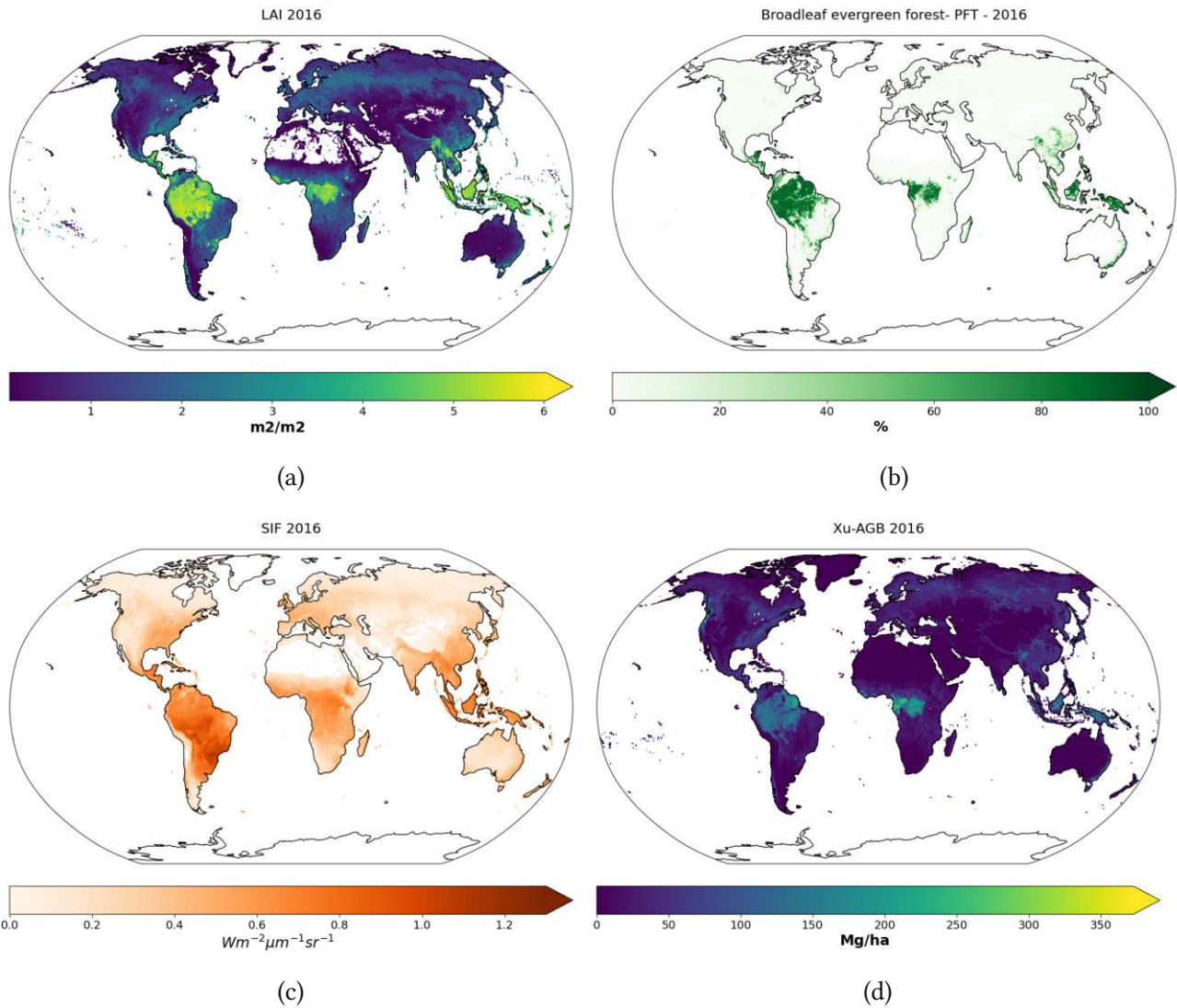
Figure 2: Yearly means of optical auxiliary data for the year 2016: a) LAI (Myneni, Knyazikhin, and Park, 2015), b) Land Cover (ESA, 2017), c) SIF (Wen et al., 2021) and AGB reference data: d) Xu-AGB (Xu et al., 2021).
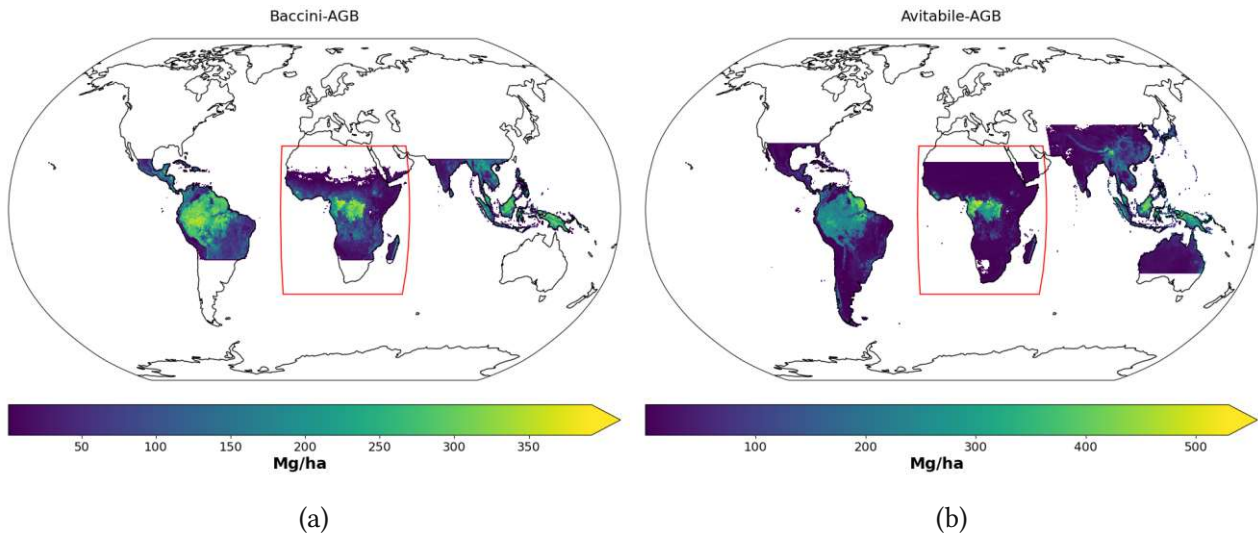
Figure 3: Static AGB reference maps: a) Baccini-AGB (Baccini et al., 2012), b) Avitabile-AGB (Avitabile et al., 2016). The red line indicates the border of the study area used for the analysis in this thesis.

3. Methods

3.1. Correlation analysis between VODCA and AGB

Just like in the study by Rodríguez-Fernández et al. (2018), the first step was to create 2D-Histogramms and calculate correlation coefficients (Pearson's r, Spearman's ρ and Kendall's τ) between the different VODCA products and the AGB maps from Baccini et al. (2012), Avitabile et al. (2016) and Xu et al. (2021). Additionally, the temporal per-pixel correlation between the different VOD bands and Xu-AGB was also calculated to get information about the location-dependent relationship between VOD and AGB.

Pearson correlation

The Pearson correlation coefficient is a measure of the linear relationship among two sets of data and has a value between -1 and 1, where 1 means perfect positive linear relationship, 0 means no linear relationship, and -1 means perfect negative linear relationship (Virtanen et al., 2020). It assumes a normal distribution of the data (Virtanen et al., 2020). The Pearson correlation coefficient is calculated as follows (Virtanen et al., 2020):

$$r = \frac{\sum(x_i - m_x)(y_i - m_y)}{\sqrt{\sum(x_i - m_x)^2 \sum(y_i - m_y)^2}} \tag{1}$$

where m_x and m_y are the mean values of the two variables.

Spearman correlation

The Spearman's rank correlation coefficient expresses the correlation between the ranks of two sets of data and is computed by using ranks instead of actual values in the formula for the Pearson correlation coefficient (Kokoska and Zwillinger, 2000). The formula for the Spearman correlation coefficient can therefore be written as follows:

$$\rho = \frac{\sum(d_x - m_{d_x})(d_y - m_{d_y})}{\sqrt{\sum(d_x - m_{d_x})^2 \sum(d_y - m_{d_y})^2}} \tag{2}$$

where d_x and d_y are the respective ranks of the two datasets and m_{d_x} and m_{d_y} are the mean values of the respective ranks.

Kendall correlation

The Kendall correlation is used to describe the correlation between ordinal data (Virtanen et al., 2020). It gives information about the degree of agreement between rankings of two datasets, where values near 1 demonstrate good agreement and values near -1 show strong disagreement (Virtanen et al., 2020). The definition according to Virtanen et al. (2020) of Kendall's τ is:

$$\tau = \frac{2 \times (P - Q)}{n^2 \times (m - 1)/m} \tag{3}$$

P represents the number of concordant pairs and Q is the number of discordant pairs (Virtanen et al., 2020). The variable n refers to the overall number of samples, whereas m represents the count of unique values in dataset 1 or 2, depending on which one is smaller (Virtanen et al., 2020).

3.2. Application of the univariate parametric regression approach by Rodríguez-Fernández et al. (2018)

To predict AGB as a function VOD, the VOD bands were binned using a bin-width of 0.05 and subsequently the mean, the 5th and 95th percentile of the AGB distribution were calculated for each bin, resulting in three AGB point curves per VOD band. The points from these curves were then used to fit two functions per curve, predicting AGB as a function of VOD. This curve-fitting was done using the function applied by Liu et al. (2015):

$$AGB = a \times \frac{arcatan(b(VOD - c)) - arctan(-bc)}{(arcatan(\infty) - arcatan(-bc))} + d \tag{4}$$

and a logistic function from Rodríguez-Fernández et al. (2018):

$$AGB = \frac{a}{1 + e^{(-b(VOD - c))}} + d \tag{5}$$

where a, b, c and d are the function parameters adjusted to fit the data.

3.3. Predicting AGB from VOD using random forest and univariate parametric regression

To compare the random forest approach to the univariate parametric regression approach from previous studies (Liu et al. (2015), Fan et al. (2019)), several different models were developed. Models were created both for the prediction of unknown locations and unknown time periods, relying on different input data. An overview of the model configurations is given in Table 2.

Model name	Model features	Train/Test Mask	Years:Train	Years:Test	Prediction Type
Liu-UL	VOD	YES	2010-2019	2010-2019	*unknown locations*
Log-UL	VOD	YES	2010-2019	2010-2019	*unknown locations*
RF-UL(VOD)	VOD	YES	2010-2019	2010-2019	*unknown locations*
RF-UL(VOD, LAI)	VOD, LAI	YES	2010-2019	2010-2019	*unknown locations*
RF-UL(VOD, LAI, LC)	VOD, LAI, LC	YES	2010-2019	2010-2019	*unknown locations*
RF-UL(VOD, LAI, LC, SIF)	VOD, LAI, LC, SIF	YES	2010-2018	2010-2018	*unknown locations*
RF-UL(VOD, VOD-statistics)	VOD, VOD-statistics	YES	2010-2019	2010-2019	*unknown locations*
RF-UL(VOD, VOD-statistics, LAI)	VOD, VOD-statistics, LAI	YES	2010-2019	2010-2019	*unknown locations*
RF-UL(VOD, VOD-statistics, LAI, LC)	VOD, VOD-statistics, LAI, LC	YES	2010-2019	2010-2019	*unknown locations*
RF-UL(VOD, VOD-statistics, LAI, LC, SIF)	VOD, VOD-statistics, LAI, LC, SIF	YES	2010-2018	2010-2019	*unknown locations*
Liu-UT	VOD	NO	2010, 2017, 2018	2011-2016, 2019	*unknown time periods*
Log-UT	VOD	NO	2010, 2017, 2018	2011-2016, 2019	*unknown time periods*
RF-UT(VOD)	VOD	NO	2010, 2017, 2018	2011-2016, 2019	*unknown time periods*
RF-UT(VOD, LAI)	VOD, LAI	NO	2010, 2017, 2018	2011-2016, 2019	*unknown time periods*
RF-UT(VOD, LAI, LC)	VOD, LAI, LC	NO	2010, 2017, 2018	2011-2016, 2019	*unknown time periods*
RF-UT(VOD, LAI, LC, SIF)	VOD, LAI, LC, SIF	NO	2010, 2017, 2018	2011-2016	*unknown time periods*
RF-UT(VOD, VOD-statistics)	VOD, VOD-statistics	NO	2010, 2017, 2018	2011-2016, 2019	*unknown time periods*
RF-UT(VOD, VOD-statistics, LAI)	VOD, VOD-statistics, LAI	NO	2010, 2017, 2018	2011-2016, 2019	*unknown time periods*
RF-UT(VOD, VOD-statistics, LAI, LC)	VOD, VOD-statistics, LAI, LC	NO	2010, 2017, 2018	2011-2016, 2019	*unknown time periods*
RF-UT(VOD, VOD-statistics, LAI, LC, SIF)	VOD, VOD-statistics, LAI, LC, SIF	NO	2010, 2017, 2018	2011-2016	*unknown time periods*

Table 2: Overview of the different model configurations used for the prediction of unknown locations (UL) and time periods (UT).

3.3.1. Random forest approach

Definition

A random forest is an ensemble method that fits a quantity of decision tree classifiers on different sub-samples of the dataset and applies averaging to increase the predictive accuracy and manage overfitting (Pedregosa et al., 2011). The behavior of the generalization error of a random forest is such that it converges to a limit when the quantity of trees in the forest gets large (Breiman, 2001). The generalization error of a random forest is dependent on the power of each tree it contains and the correlation between the trees (Breiman, 2001).

Hyperparameter Optimization

The hyperparameter optimization of the random forest regressor was done using the GridSearchCV function from the scikit-learn package (Pedregosa et al., 2011), with the following parameters:

- estimator: RandomForestRegressor(n_estimators = 100)

- param_grid: {*min_samples_split*: [10, 20, 50, 100]}

- cv: cv_split_train

A random forest regressor with 100 trees was used as the estimator and the cross-validation parameter (cv) was created using a custom function that creates 5 folds containing train and test indices for cross-validation.

Subsequently, different models were trained to predict AGB with different sets of input variables (Table 2), by using the reference datasets from Xu et al. (2021) in both testing and training.

3.3.2. Univariate parametric regression approach

Just as in section 3.1, functions were fitted (Equation 4, 5) to predict AGB (Xu et al., 2021) from L-VOD (Moesinger et al., 2020), except that this time the curve fitting was not done on single years but on the entire training datasets of the respective model configurations.

3.3.3. Train/Test split

For the models predicting unknown locations, the train/test split of the model input datasets was done with a static train/test mask (Figure 4a, 4b) of randomly distributed boxes, splitting each dataset into 75% training and 25% testing data for each available year (Table 2).
The distribution of the different dominant land cover classes in the training and testing data was checked to ensure that the models are not overfitting to a specific class. This assessment was done for each RF model by plotting the percentages of the different land cover classes in the training and testing data (Figure 5).

For models predicting unknown time periods, on the other hand, the train/test split was simply done by arbitrarily selecting certain years for training and testing. The years 2010, 2017 and 2018 were selected for training and the years 2011-2016 and 2019 for testing (Table 2).

(a)   (b)
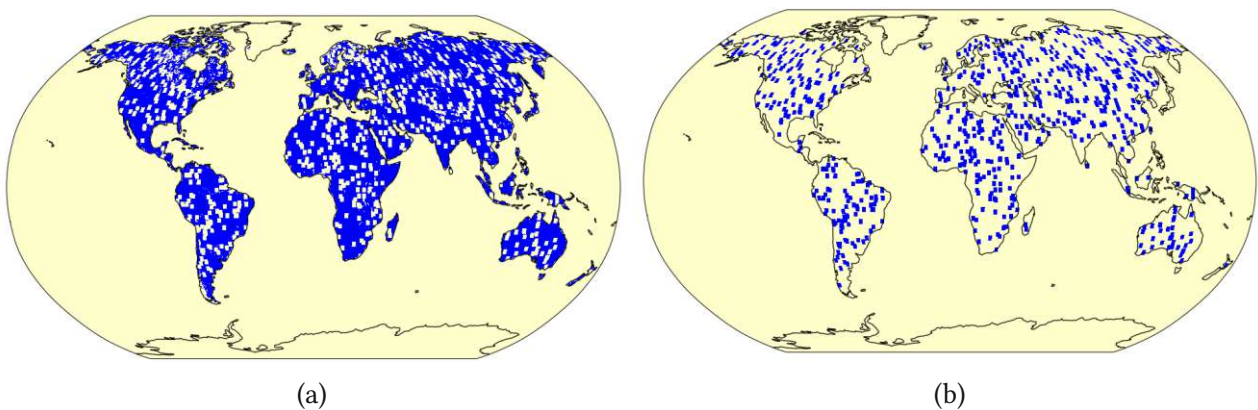
Figure 4: Train (a) and test (b) areas used for the training and testing of the RF models making predictions for unknown locations. The blue area represents the selected areas used for training and testing, respectively. The boxes are randomly distributed over the global grid. The training area accounts for ca. 75% and the test area for ca. 25% of land pixels.
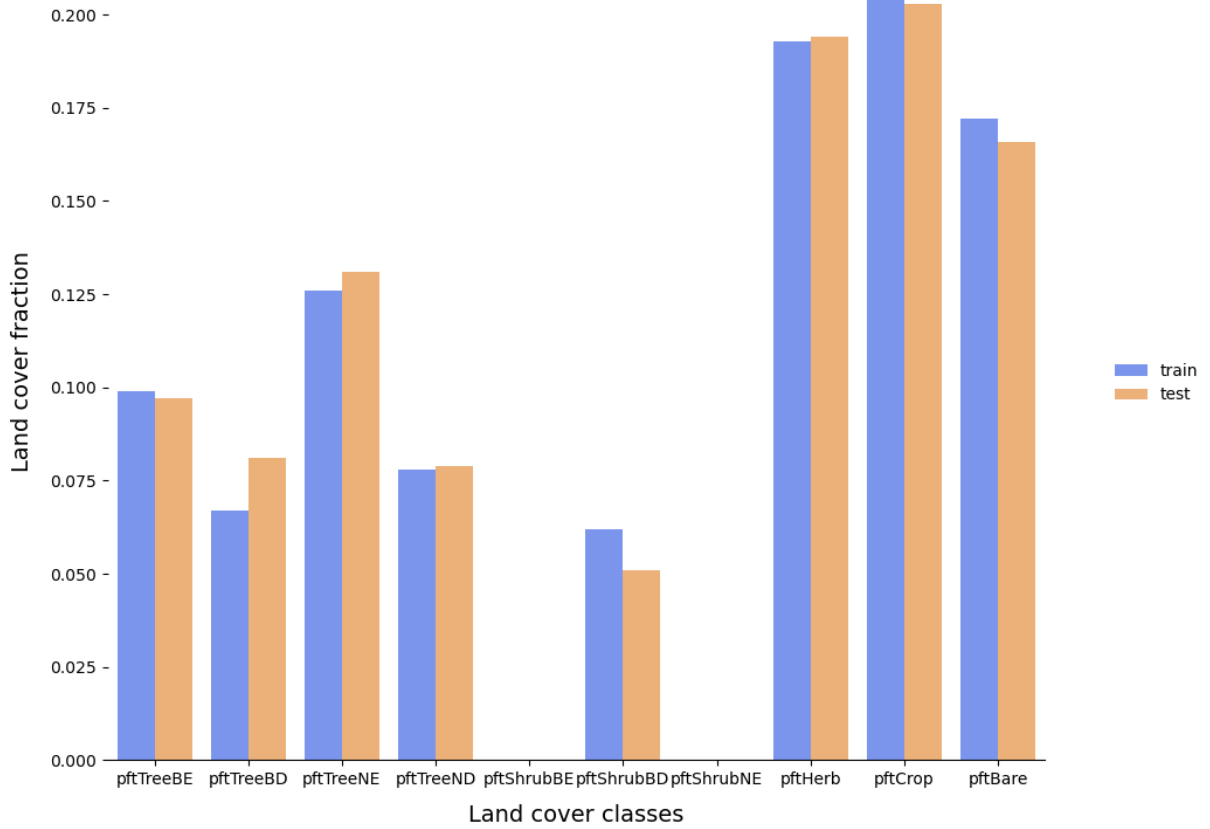
Figure 5: Normalized distribution of dominant land cover classes in the training and testing data for the RF models making predictions for unknown locations.

3.4. Model evaluation

3.4.1. Performance

The prediction accuracy of the models was assessed by calculating R^2 scores between the predicted AGB values and the reference AGB values from Xu-AGB. The R^2 score, also known as the coefficient of determination, is defined as the fraction of variance that is explained by the individual predictors in the model (Pedregosa et al., 2011). The best possible score that can be achieved is 1.0, and the score can also be negative if the model is arbitrarily worse (Pedregosa et al., 2011). The R^2 score, used by Pedregosa et al. (2011), for a set of predicted values $\hat{y}_i$ and corresponding true reference values y_i is calculated as follows:

$$R^2(y, \hat{y}) = 1 - \frac{\sum_{i=1}^{n}(y_i - \hat{y}_i)^2}{\sum_{i=1}^{n}(y_i - \bar{y})^2} \tag{6}$$

where n is the number of samples and $\bar{y} = \frac{1}{n}\sum_{i=1}^{n} y_i$.

Furthermore, in addition to the R^2 scores, correlation coefficients between predicted AGB and

Baccini-AGB were calculated to assess the performance against an independent reference dataset.

3.4.2. Predictor contribution

To find the most important input variables of the models, partial dependence plots (PDP) and feature importance plots were generated.

Using the scikit-learn package from Pedregosa et al. (2011), feature importances were expressed as the mean decrease in impurity (MDI), which is calculated as the weighted average of the single tree's enhancement inside the splitting criterion generated by every single variable for each model feature (Loecher, 2022).

The partial dependence plots (PDP) are calculated with the help of the scikit-learn package (Pedregosa et al., 2011), which bases its calculation of the PDPs on Molnar (2022), Goldstein et al. (2013) and Hastie, Tibshirani, and Friedman (2009). The partial dependence can be described as the anticipated target response as a function of the respective input features in the model (Hastie, Tibshirani, and Friedman, 2009).

If X_s is a set of input features that we are interested in, and X_c is its complement (all features that are not in X_s), then the partial dependence (by Pedregosa et al. (2011)) at a point x_s in X_s is defined as:

$$pd_{X_s}(x_s) \overset{def}{=} \mathbb{E}_{X_c}[f(x_s, X_c)] = \int f(x_s, x_c)p(x_c)dx_c \tag{7}$$

with $f(x_s, x_c)$ being the response function for a specific sample that has its values defined by x_c for the features in X_c, and by x_s for the features in X_s.

3.4.3. Spatiotemporal patterns

Additionally, to analyze the location-dependent model performance, annual residual maps were calculated between the predicted AGB maps for unknown time periods and Xu-AGB.

3.5. Assessment of change patterns in predicted AGB

For the model predictions of unknown time periods, global AGB time series per land cover class were computed for each model and compared to a reference time series from Xu-AGB. The time series was only calculated for map locations where data was available for all years, leading to smaller spatial coverage because of the missing data in some years. Furthermore, per-pixel changes of AGB were calculated for the Amazon basin between the first and last year of the time series and compared to per-pixel changes of the reference data from Xu-AGB. This was done to assess the ability of the models to capture the AGB changes for individual pixels.
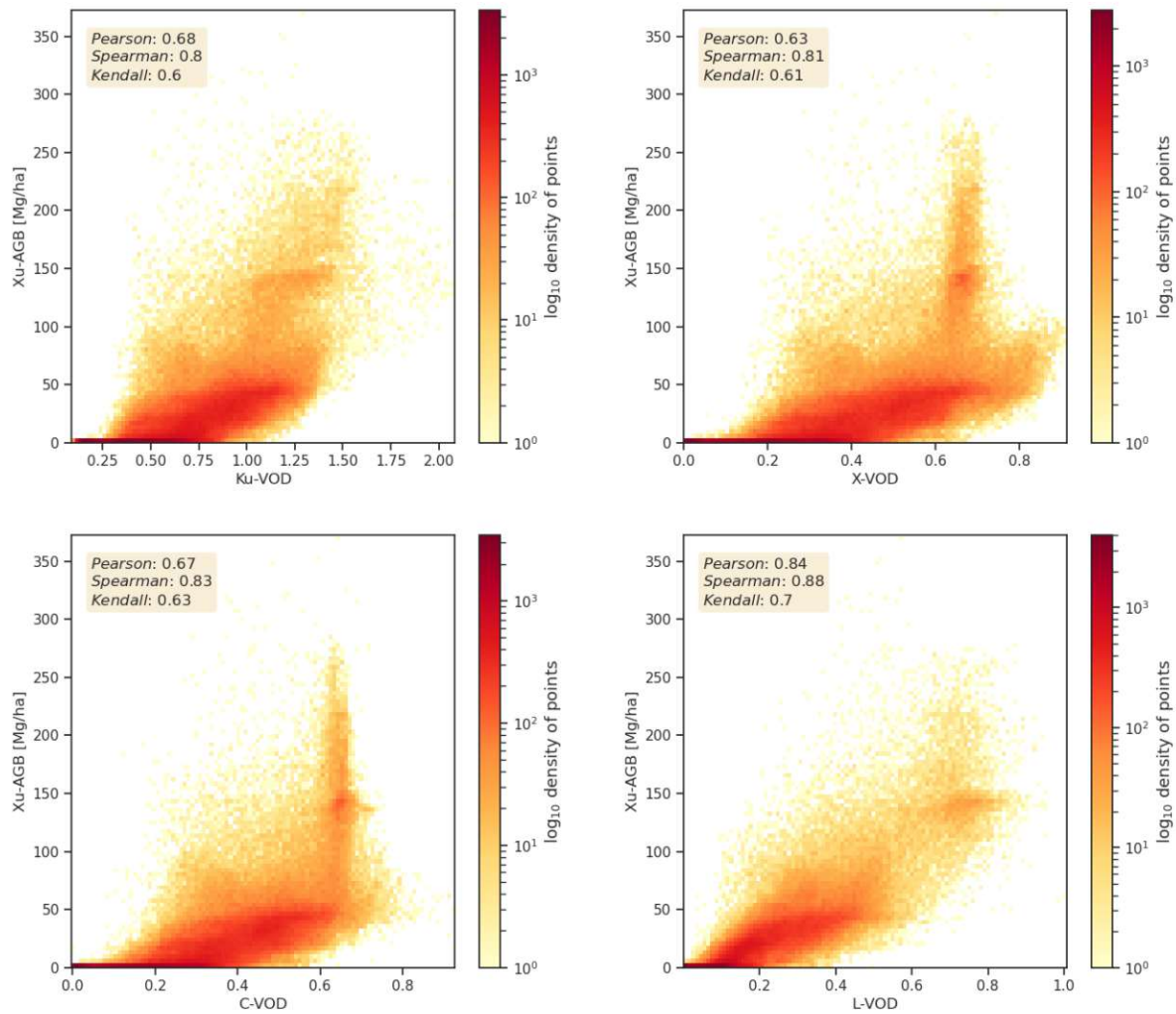
4. Results

4.1. VODCA-AGB relationship

Figure 6: Relationship between individual VODCA bands (Moesinger et al., 2020) and AGB from Xu et al. (2021) for the year 2012.

	R				ρ				τ			
	Ku	X	C	L	Ku	X	C	L	Ku	X	C	L
Xu-AGB 2011	0.67	0.63	0.66	0.87	0.79	0.80	0.82	0.87	0.59	0.60	0.62	0.69
Xu-AGB Africa 2011	0.71	0.64	0.67	0.91	0.87	0.88	0.88	0.91	0.67	0.68	0.69	0.73
Xu-AGB 2012	0.68	0.63	0.67	0.84	0.80	0.81	0.83	0.88	0.60	0.61	0.63	0.70
Xu-AGB Africa 2012	0.72	0.65	0.68	0.90	0.88	0.88	0.89	0.91	0.68	0.69	0.70	0.73
Avitabile-AGB 2011	0.62	0.54	0.57	0.85	0.81	0.82	0.82	0.82	0.63	0.63	0.64	0.63
Avitabile-AGB 2012	0.63	0.55	0.57	0.85	0.81	0.82	0.81	0.82	0.63	0.63	0.62	0.63
Baccini-AGB 2011	0.82	0.75	0.78	0.91	0.90	0.90	0.91	0.86	0.73	0.74	0.74	0.69
Baccini-AGB 2012	0.82	0.75	0.77	0.90	0.89	0.90	0.90	0.86	0.72	0.73	0.72	0.68

Table 3: Correlation coefficients between VODCA bands (Moesinger et al., 2020) and the AGB maps from Avitabile et al. (2016), Baccini et al. (2012), and Xu et al. (2021). The term Xu-AGB Africa refers to the African subset of Xu et al. (2021) that was used for the comparison against Baccini-AGB and Avitabile-AGB. Results L-VOD are highlighted in yellow.

Globally, the highest correlation values (Pearson, Spearman, Kendall) between VODCA and Xu-AGB are observed for L-VOD (Table 3, Figure 6, A.1), which was expected based on results from Dou et al. (2023). When Baccini-AGB is compared to VODCA for Africa, Spearman and Kendall correlation values of the higher frequency bands (Ku, X, C) are slightly higher compared to L-VOD. For the other AGB-Products (Xu-AGB, Avitabile-AGB), this is not the case. Ku-VOD shows higher Pearson correlation values than X and C-VOD, which is surprising since generally the sensitivity of VOD to AGB decreases with increasing frequency (Chaparro et al., 2018).

The correlation results are quite similar to the results of Rodríguez-Fernández et al. (2018) for the SMOS L-VOD products (Table 5). For the African continent, the Pearson correlation between L-VOD and Xu-AGB is slightly lower compared to the Pearson correlation in Rodríguez-Fernández et al. (2018) between SMOS-IC and Baccini-AGB. However, if the Pearson correlation between L-VOD and Avitabile-AGB is compared to the Pearson correlation between Xu-AGB and L-VOD, the Pearson correlation between L-VOD and Avitabile-AGB is lower. The rest of the Pearson correlation coefficients in Rodríguez-Fernández et al. (2018) between other SMOS L-VOD products (SMOS LEVEL 2 and 3) and the respective AGB-Maps (Baccini-AGB, Avitabile-AGB) are also lower. The same pattern is also visible when comparing Spearman and Kendall correlation coefficients.
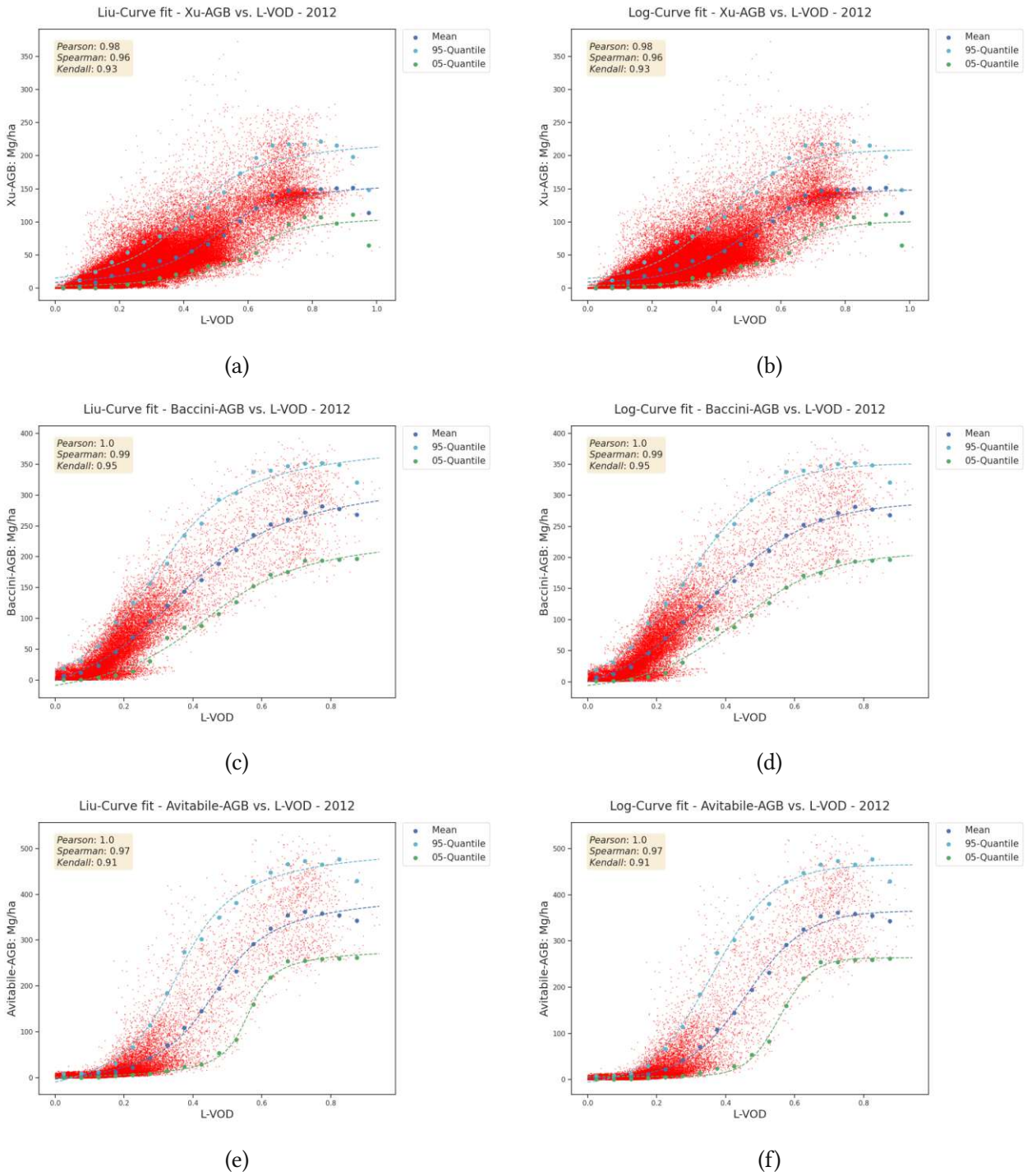
Figure 7: AGB-functions fitted to the mean, 5th and 95th percentile AGB values inside the bins (width 0.05) for different combinations of AGB-data (Baccini et al. (2012), Avitabile et al. (2016), Xu et al. (2021)) and L-VOD (Moesinger et al., 2020). Additionally, the correlation values between the functions and the respective points are displayed. Note: Xu-AGB has a global extent, whereas Baccini and Avitabile-AGB are limited to Africa.

27

The correlation coefficients (Pearson, Spearman, Kendall) between the lines of the fitted mean functions and respective mean points (Figure 7, section 3.2), used to fit the functions, are very similar to the study by Rodríguez-Fernández et al. (2018). The Pearson correlation is the highest, followed by Spearman and Kendall (Figure 7). The correlation coefficients (Figure 7) between L-VOD and AGB are slightly higher for Baccini and Avitabile-AGB compared to Xu-AGB. The reason for this might be the smaller extent of Baccini and Avitabile-AGB, which might lead to less variability in the AGB-VOD relationship.
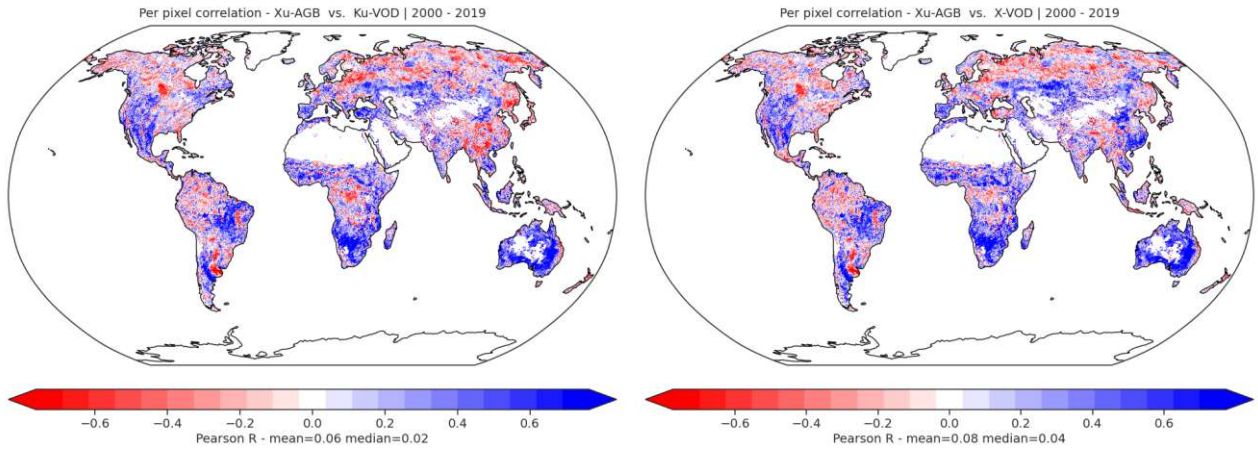
(a) Temporal correlation (Pearson's r) between Ku-VOD and Xu-AGB for the years 2000-2019.

(b) Temporal correlation (Pearson's r) between X-VOD and Xu-AGB for the years 2000-2019.
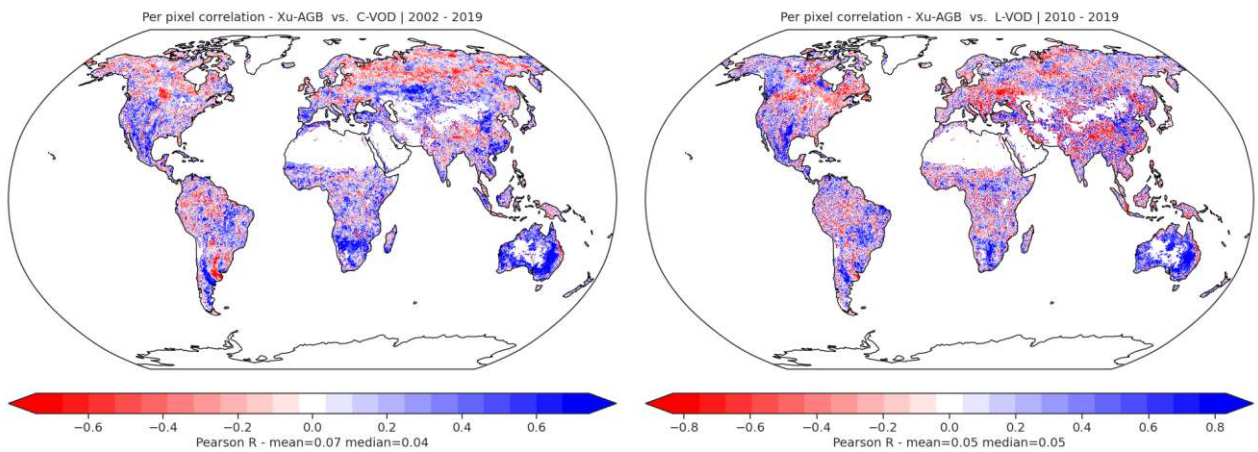
(c) Temporal correlation (Pearson's r) between C-VOD and Xu-AGB for the years 2002-2019.

(d) Temporal correlation (Pearson's r) between L-VOD and Xu-AGB for the years 2010-2019.

The temporal correlation between VODCA and Xu-AGB shows mostly negative correlation for densely vegetated areas like forests, while sparse vegetation types like shrubs exhibit positive correlation (Figure 8a, 8b, 8c, 8d).

If we look at the per-pixel correlation (Figure 8a, 8b, 8c, 8d) between VODCA and Xu-AGB we can detect different patterns. For rainforests, correlation patterns are quite mixed throughout the globe (Figure 8a, 8b, 8c, 8d). Regarding rainforests, Ku-VOD shows the clearest pattern (Figure 8a), with the majority of rainforests exhibiting negative correlation, except for Asian rainforests. The negative correlation found mostly in densely vegetated areas like forests seems to decrease with decreasing band frequency. For the positive correlation in sparse vegetation types, the same holds. Correlation patterns of L-VOD (Figure 8d) are much noisier compared to the other VODCA products, which is likely due to the shorter time series. However, patches of positive correlation can be seen for areas with sparse vegetation, with the largest of these patches located in Australia, Africa and South America.

4.2. Model evaluation

4.2.1. Performance

Model name	$R^2[\%]$	Model name	$R^2[\%]$
Liu-UL	71.87	Liu-UT	69.61
Log-UL	71.82	Log-UT	69.81
RF-UL(VOD)	79.95	RF-UT(VOD)	79.48
RF-UL(VOD, LAI)	83.28	RF-UT(VOD, LAI)	84.50
RF-UL(VOD, LAI, LC)	89.80	RF-UT(VOD, LAI, LC)	96.16
RF-UL(VOD, LAI, LC, SIF)	90.54	RF-UT(VOD, LAI, LC, SIF)	96.03
RF-UL(VOD, VOD-statistics)	82.80	RF-UT(VOD, VOD-statistics)	83.21
RF-UL(VOD, VOD-statistics, LAI)	85.50	RF-UT(VOD, VOD-statistics, LAI)	87.26
RF-UL(VOD, VOD-statistics, LAI, LC)	90.43	RF-UT(VOD, VOD-statistics, LAI, LC)	95.88
RF-UL(VOD, VOD-statistics, LAI, LC, SIF)	91.04	RF-UT(VOD, VOD-statistics, LAI, LC, SIF)	95.90

Table 4: R^2 scores for different RF models for predictions of unknown locations (UL) and unknown time periods (UT).

Overall, the best prediction performance was achieved by the RF models using land cover information (Table 4). All the RF models, using only VOD, outperformed the univariate regression approach applied by Rodríguez-Fernández et al. (2018). Both for model predictions of unknown locations and model predictions of new time periods, the prediction performance of the univariate regression approaches (Table 4) is very similar. The same is the case for the base RF model using only VOD data.

Once the other model features are added, we can see that those models predicting unknown time periods show a stronger improvement than models predicting unknown locations, with the strongest increase in prediction performance, for both model types, being achieved by adding land cover information (Table 4). The addition of VODCA statistics to the models also results in a significant increase in prediction performance in most cases. However, the models making predictions for unknown time periods that use LC have almost identical prediction performance with or without VODCA statistics.
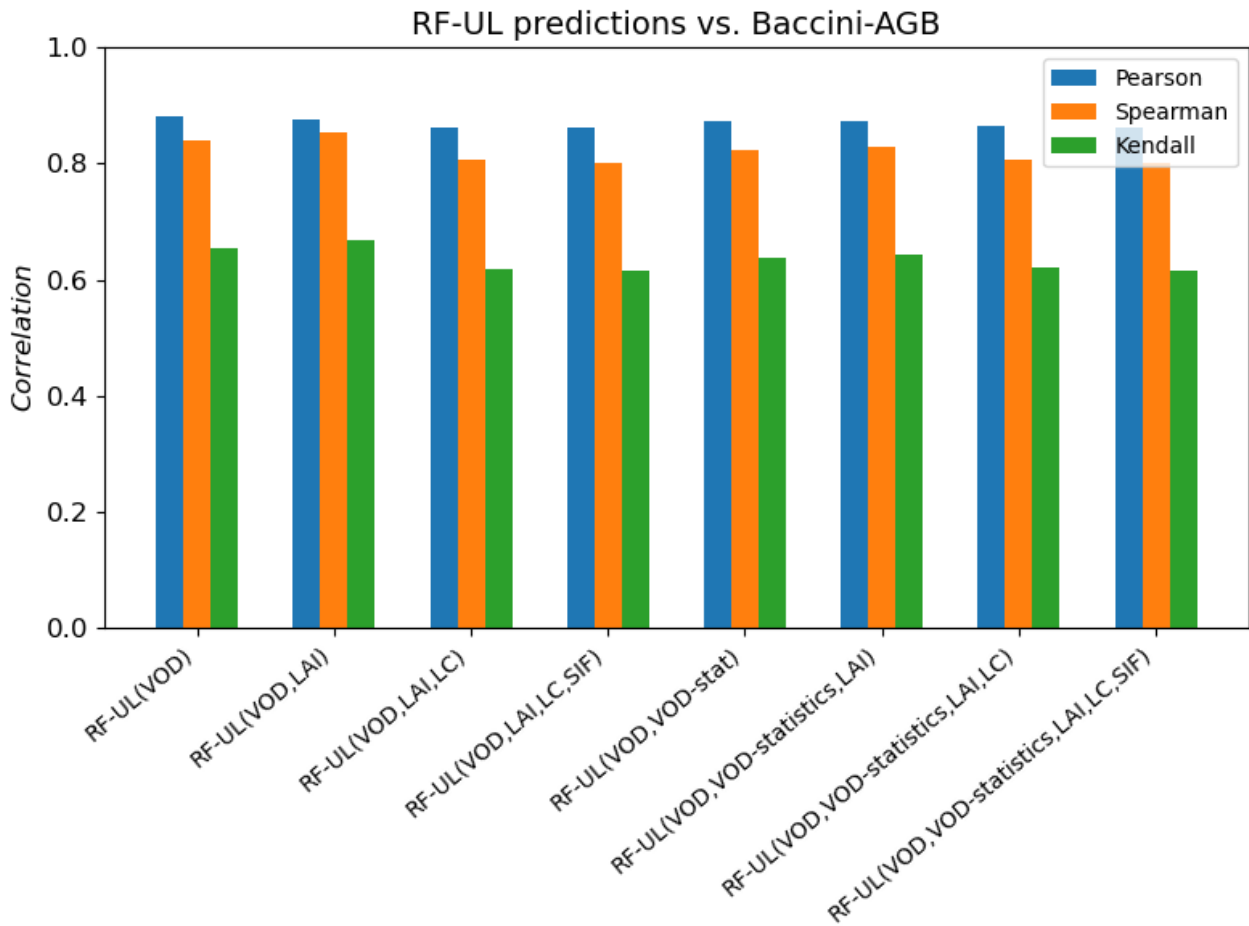
Figure 9: Correlation between AGB from Baccini et al. (2012) and predicted AGB from the different RF models making predictions for unknown locations.

The spatial correlation between the AGB values from Baccini-AGB and the predicted AGB estimates from the different models making predictions for unknown locations is almost identical for all models (Figure 9). In general, the Pearson correlation coefficient is the highest, followed closely by the Spearman correlation coefficient. The Kendall correlation values are much lower than the other two.

4.2.2. Predictor contribution

Regarding the feature importances (FI) of the RF models for the predictions of unknown time periods (Figure 10, 11), we can see that mean L-VOD is most important for the base model, relying only on the 4 VOD bands (Figure 10a). However, once statistical VOD information is added, the 75th percentile of L-VOD (L-VOD75) is the most important feature, while other statistics have only a small effect (Figure 11a). When LAI is used without LC, LAI is the most important feature before L-VOD (Figure 10b, 11b). However, once LC is added, mean L-VOD is again more important than LAI (Figure 10c, 11c, 10d, 11d). Overall the broadleaf evergreen forest LC class is the most important feature, followed by L-VOD75, mean L-VOD, LAI, and the bare soil LC class(Figure 10d, 11d). Higher

31

frequency VOD bands (Ku, X, C) showed only an impact as long as LC was not added to the model. SIF showed a moderate impact on the model, much larger than the higher frequency bands, but still much lower than the above-mentioned LC, LAI and mean L-VOD feature (Figure 10d, 11d).

The feature importances of the models for the predictions of unknown locations show a very similar pattern (Figure A.10, A.11).

Figure 10: Feature importances of RF models making predictions for unknown time periods (RF-UT) in terms of mean decrease in impurity: a) RF-UT(VOD), b) RF-UT(VOD, LAI), c) RF-UT(VOD, LAI, LC) and d) RF-UT(VOD, LAI, LC, SIF)
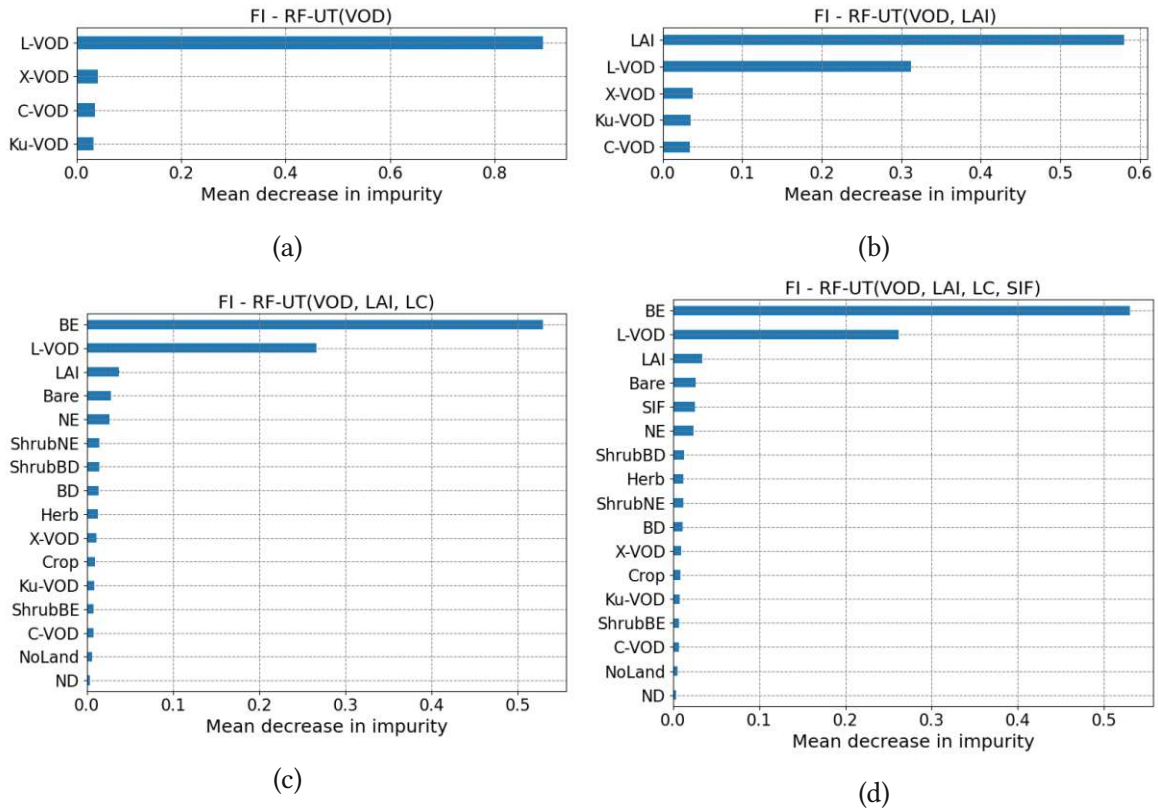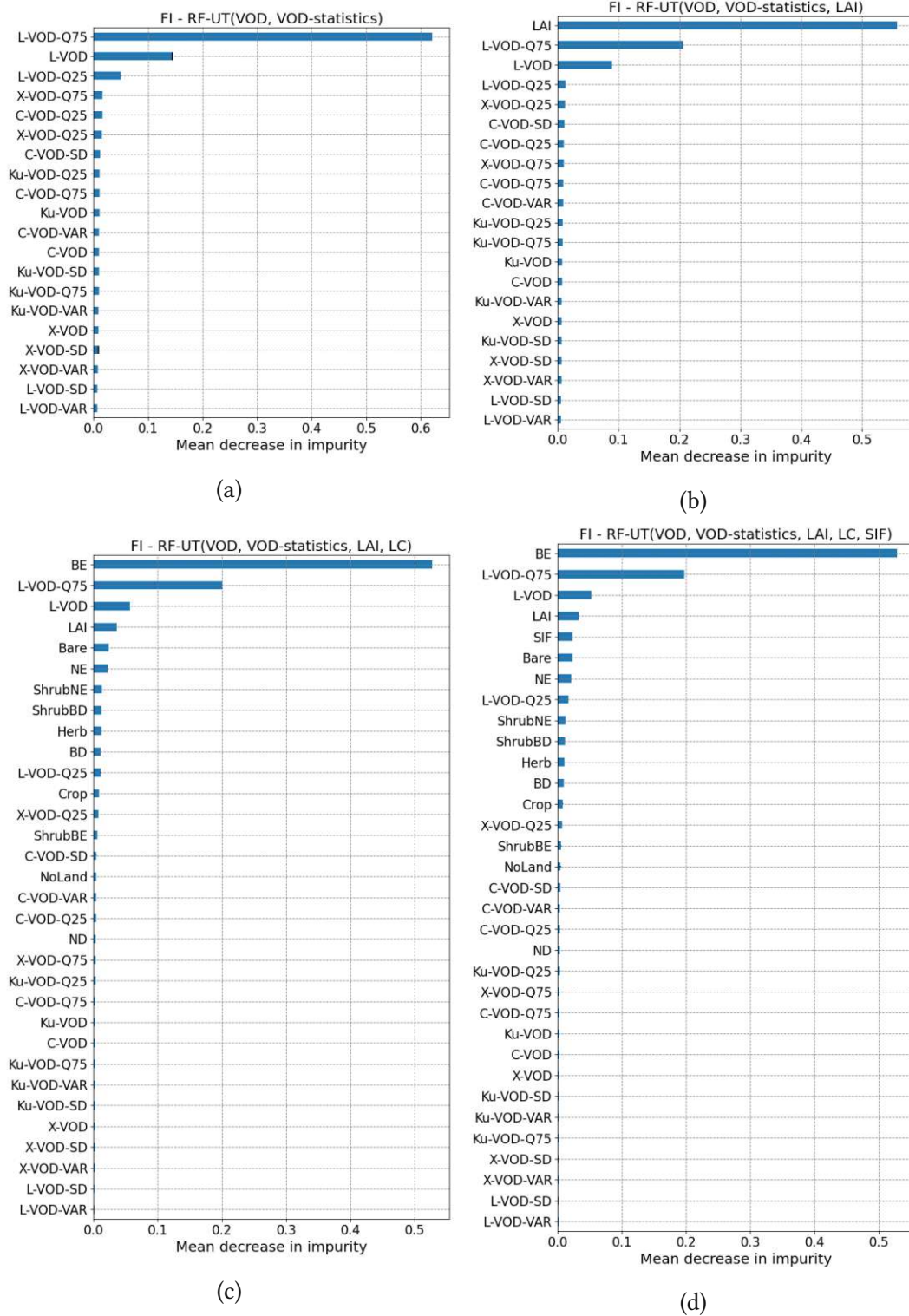
Figure 11: Feature importances of RF models making predictions for unknown time periods (RF-UT) in terms of mean decrease in impurity: a) RF-UT(VOD, VOD-statistics), b) RF-UT(VOD, VOD-statistics, LAI), c) RF-UT(VOD, VOD-statistics, LAI, LC) and d) RF-UT(VOD, VOD-statistics, LAI, LC, SIF)

The partial dependencies of the RF models making predictions for unknown time periods exhibit a similar pattern as the feature importance plots. Just like in the feature importance plots, mean L-VOD shows the highest partial dependence for the base model that uses only VODCA bands (Figure 12). After the addition of LAI to the model, the partial dependence of LAI is the highest (Figure 13), but only as long as LC is not added to the model (Figure 14, 15 - partial dependence of mean L-VOD again higher than LAI). Similar to the feature importance plots, the broad leaf evergreen LC class shows the highest partial dependence. The addition of VODCA statistics seems to result in a strong reduction of the partial dependence of mean L-VOD, and L-VOD75 takes up the role of the latter (Figure 16).

The partial dependencies of the models making predictions for unknown locations show a similar pattern as the partial dependencies of the models making predictions for unknown time periods (Figure A.12, A.13, A.14, A.15, A.16).

Figure 12: Partial dependencies of the model features used for RF-UT(VOD).

Figure 13: Partial dependencies of the model features used for RF-UT(VOD, LAI).

PDP - RF-UT(VOD, LAI, LC)

Figure 14: Partial dependencies of the model features used for RF-UT(VOD, LAI, LC).
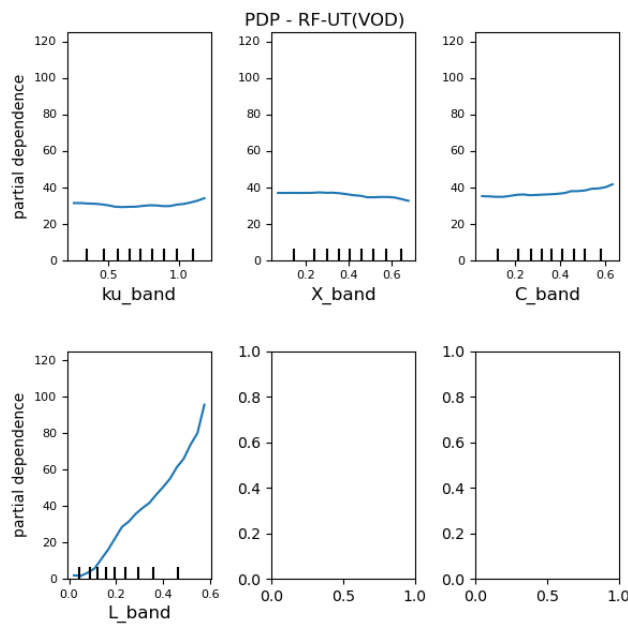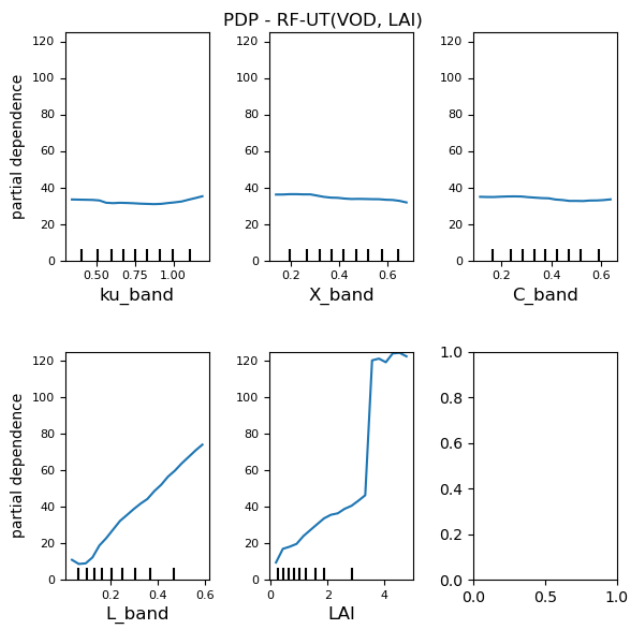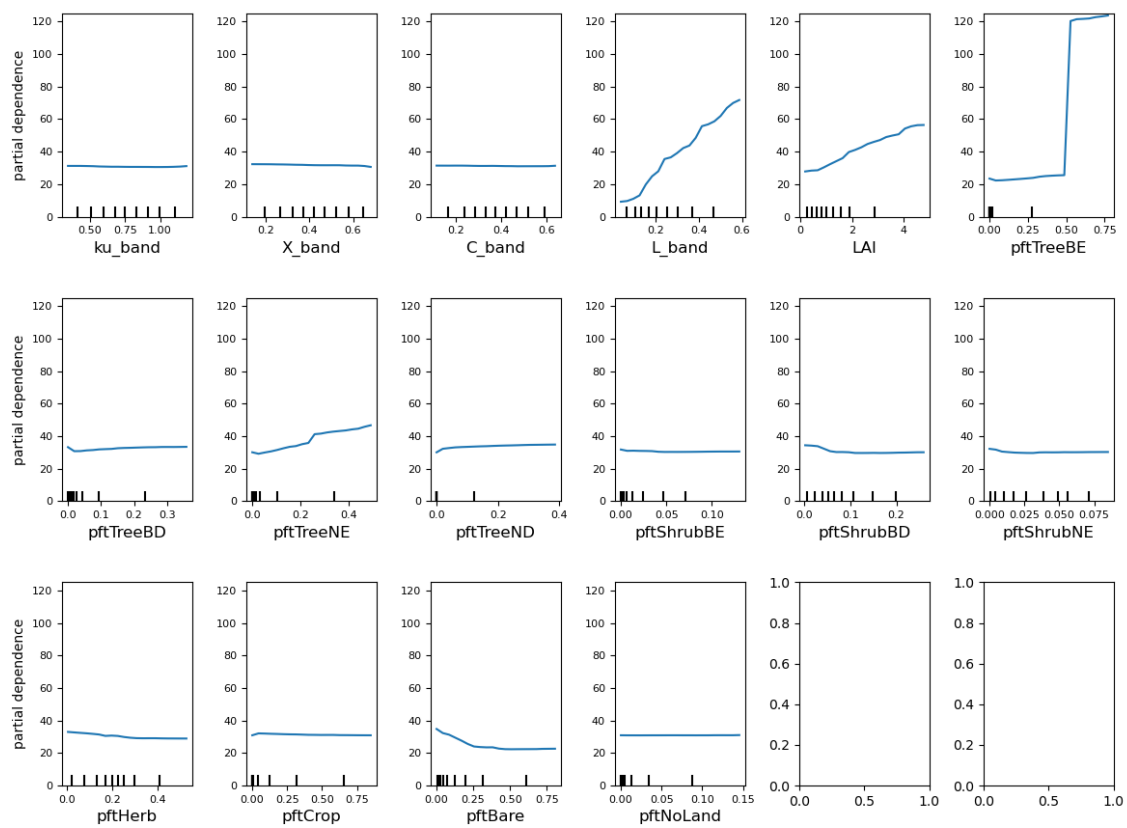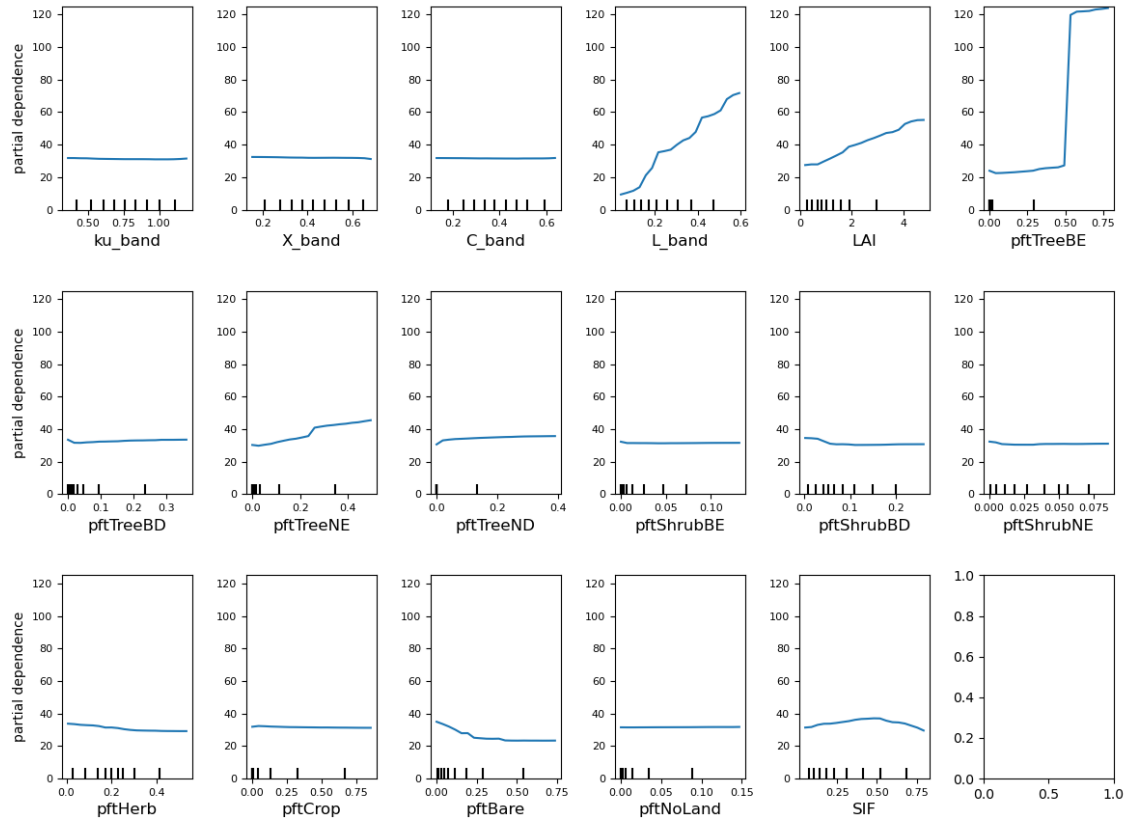
PDP - RF-UT(VOD, LAI, LC, SIF)

Figure 15: Partial dependencies of the model features used for RF-UT(VOD, LAI, LC, SIF).
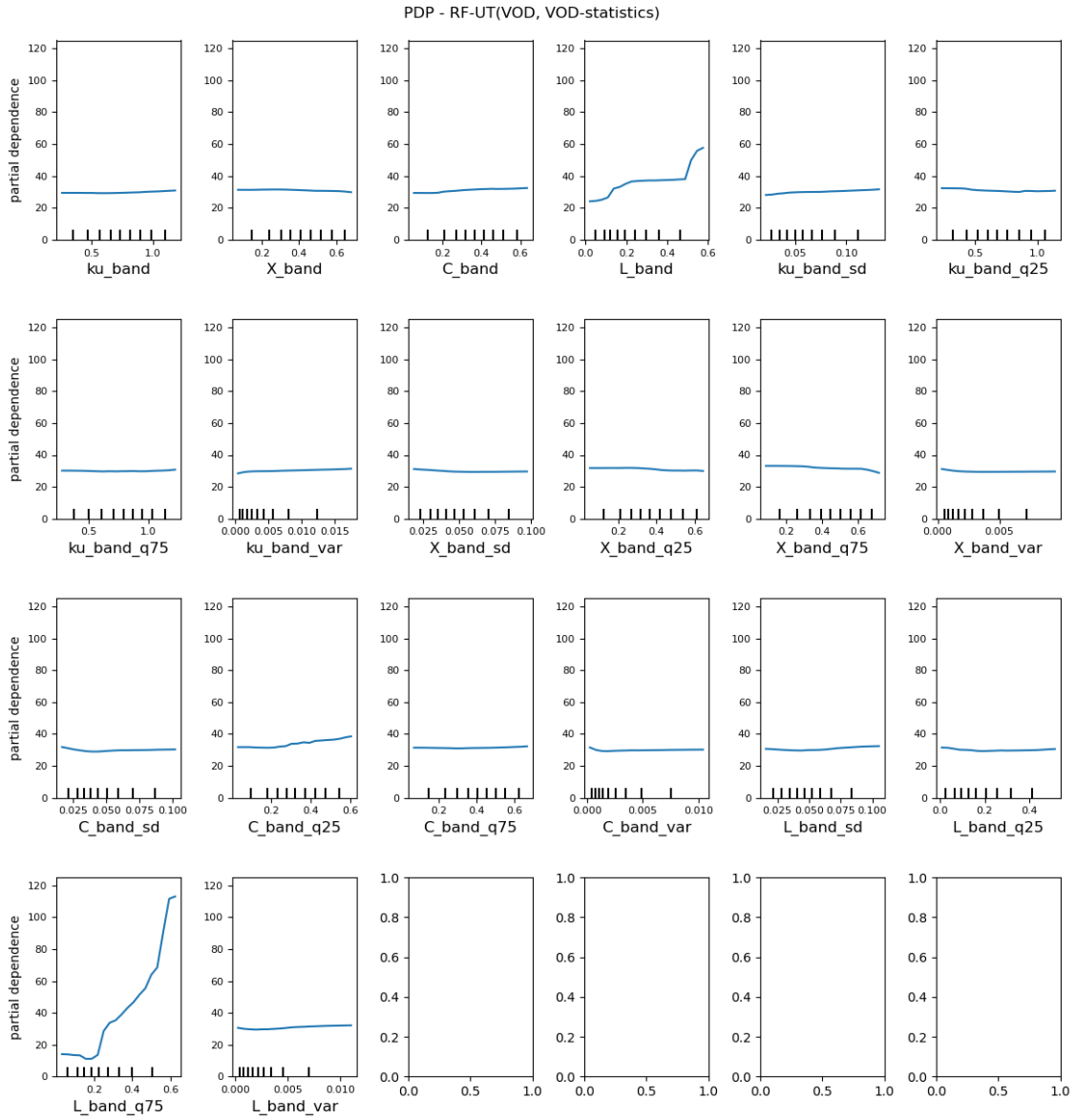
Figure 16: Partial dependencies of the model features used for RF-UT(VOD, VOD-statistics).

4.2.3. Spatiotemporal patterns

Models for the prediction of unknown time periods that rely only on VODCA bands exhibit a strong bias against the reference data from Xu-AGB, especially for the Amazon and the African rainforests. Inside the Amazon rainforest, it is even possible to see the Amazon River in the form of a strong negative bias (Figure 17a, 18a). AGB in general is underpredicted in forested areas throughout the globe. Adding LAI to the model only seems to reduce the magnitude of the bias, while the distribution of the bias remains similar (Figure 17b, 18b). The addition of LC information to the models results in significant bias reduction in all regions (Figure 17c, 18c), however, patches of land in the Amazon and African rainforest still exhibit considerable negative and positive bias. Including SIF doesn't seem to reduce the bias significantly (Figure 17d, 18d). The usage of VODCA statistics together with the 4 VODCA bands results in visible bias reduction, especially in North American forests (Figure 17a, 18a), and also in the Amazon and African rainforests, the bias is reduced in some areas. The same pattern can be seen if we compare the models RF-UT(VOD, LAI) and RF-UT(VOD, VODCA-statistics, LAI) (Figure 17b, 18b). However, once LC is added to the model features, no significant difference between the models with and without VODCA statistics is observable in terms of residuals (Figure 17c, 18c).

The RF models making predictions for unknown locations strongly underestimate AGB for all tropical rainforests and also for deciduous broadleaf forests when compared to Baccini-AGB. For deciduous broadleaf forests, the bias is not as pronounced as for the rainforests (Figure 19, 20). AGB estimates for low vegetation classes (crops, herbs, shrubs), on the other hand, show much lower underestimation against Baccini-AGB, and below the Horn of Africa, there is even a patch of land that is slightly overestimated.

Figure 17: Residuals between AGB predictions and reference data from Xu-AGB (Xu et al., 2021) for the year 2016: The models used were RF models for the predictions of unknown time periods (RF-UT) with different model feature combinations: a) VOD, b) VOD+LAI, c) VOD+LAI+LC, d) VOD+LAI+LC+SIF.

Figure 18: Residuals between AGB predictions and reference data from Xu-AGB (Xu et al., 2021) for the year 2016: The models used were RF models for the predictions of unknown time periods (RF-UT) with different model feature combinations: a) VOD+VOD-statistics, b) VOD+VOD-statistics+LAI, c) VOD+VOD-statistics+LAI+LC, d) VOD+VOD-statistics+LAI+LC+SIF.
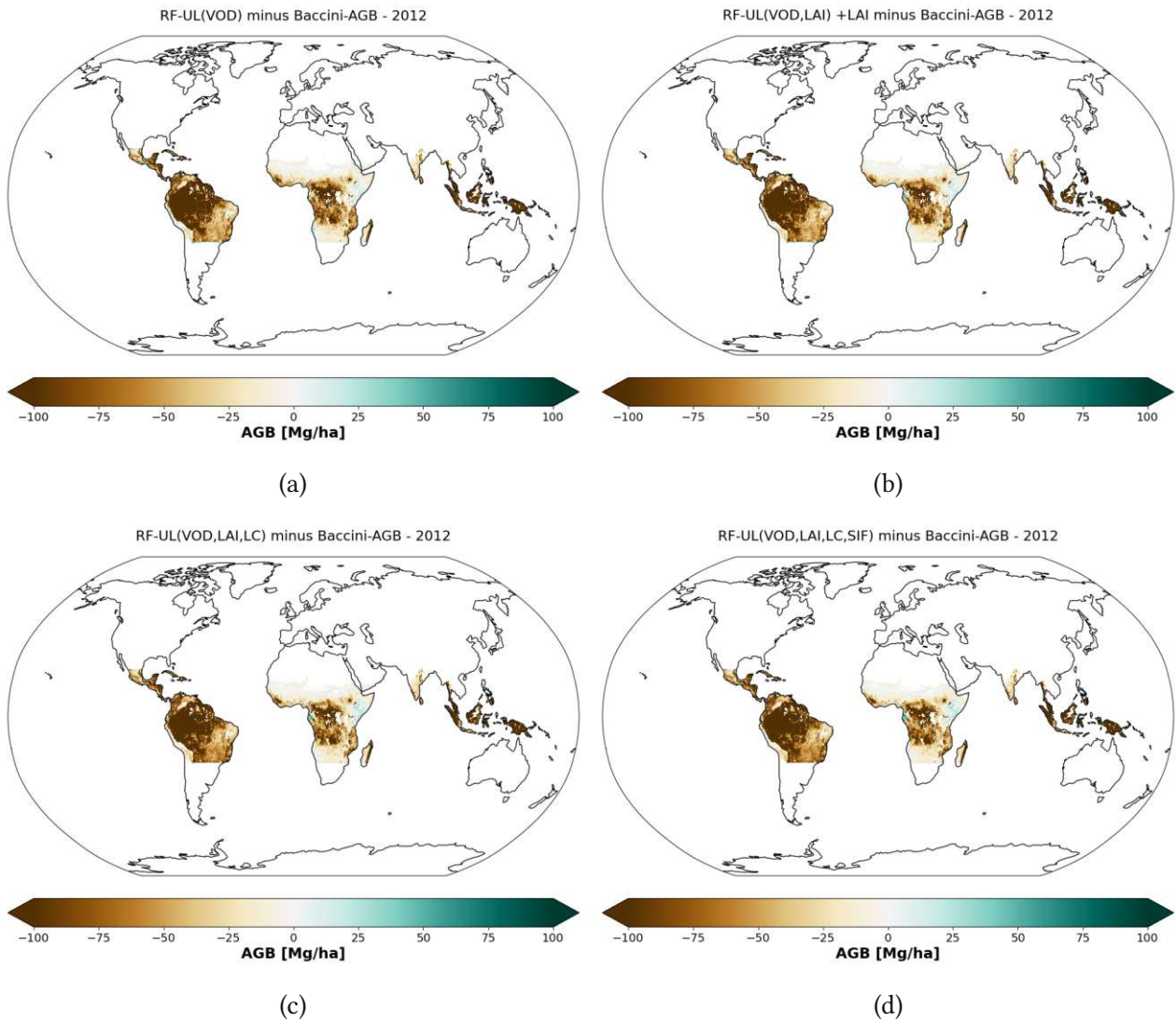
Figure 19: Residuals between AGB predictions and reference data from Baccini-AGB (Baccini et al., 2012) for the year 2016: The models used were RF models for the predictions of unknown locations (RF-UL) with different model feature combinations: a) VOD, b) VOD+LAI, c) VOD+LAI+LC, d) VOD+LAI+LC+SIF.
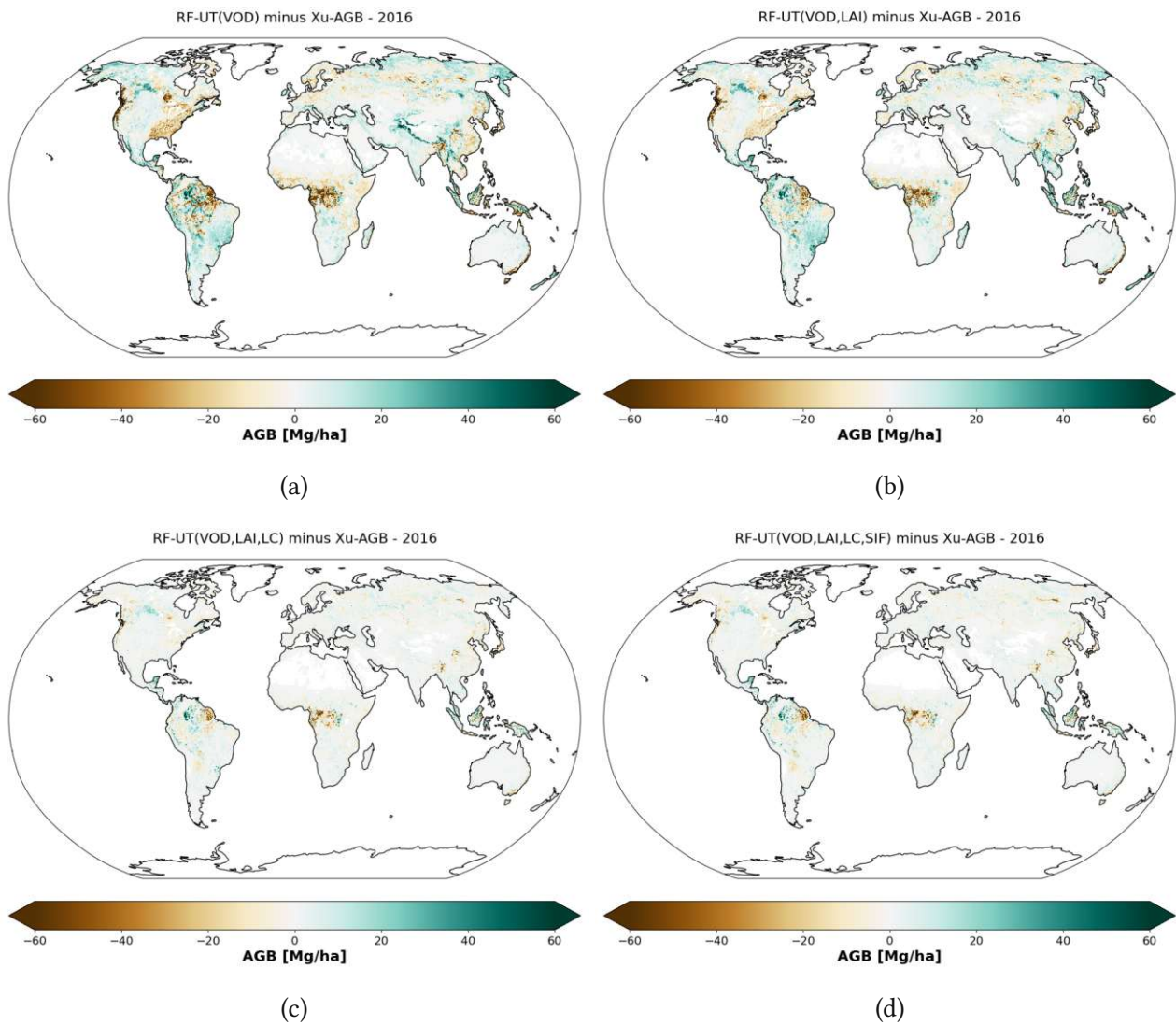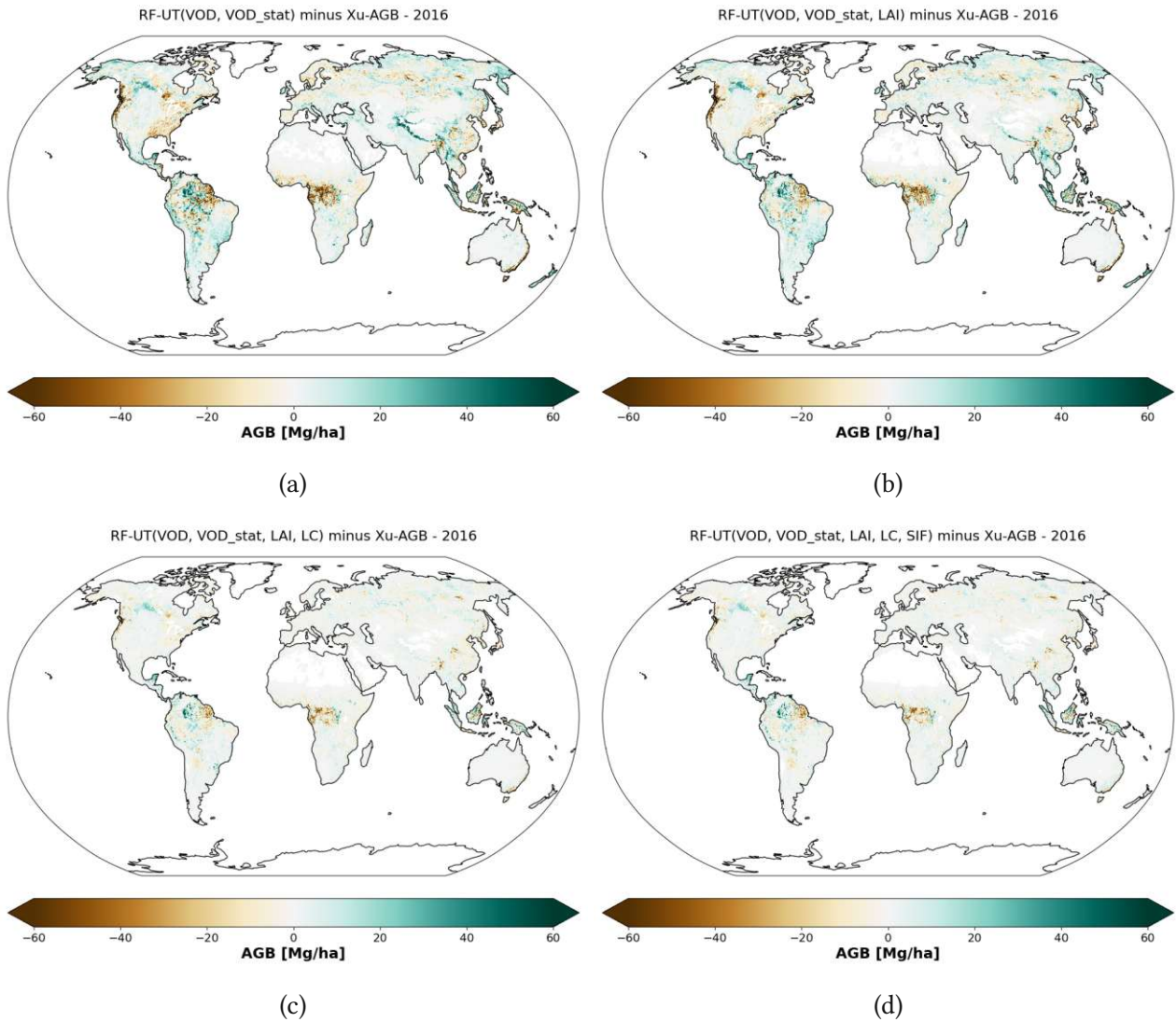
Figure 20: Residuals between model AGB predictions and reference data from Baccini-AGB (Baccini et al., 2012) for the year 2016: The models used were RF models for the predictions of unknown time periods (RF-UL) with different model feature combinations: a) VOD+VOD-statistics, b) VOD+VOD-statistics+LAI, c) VOD+VOD-statistics+LAI+LC, d) VOD+VOD-statistics+LAI+LC+SIF.
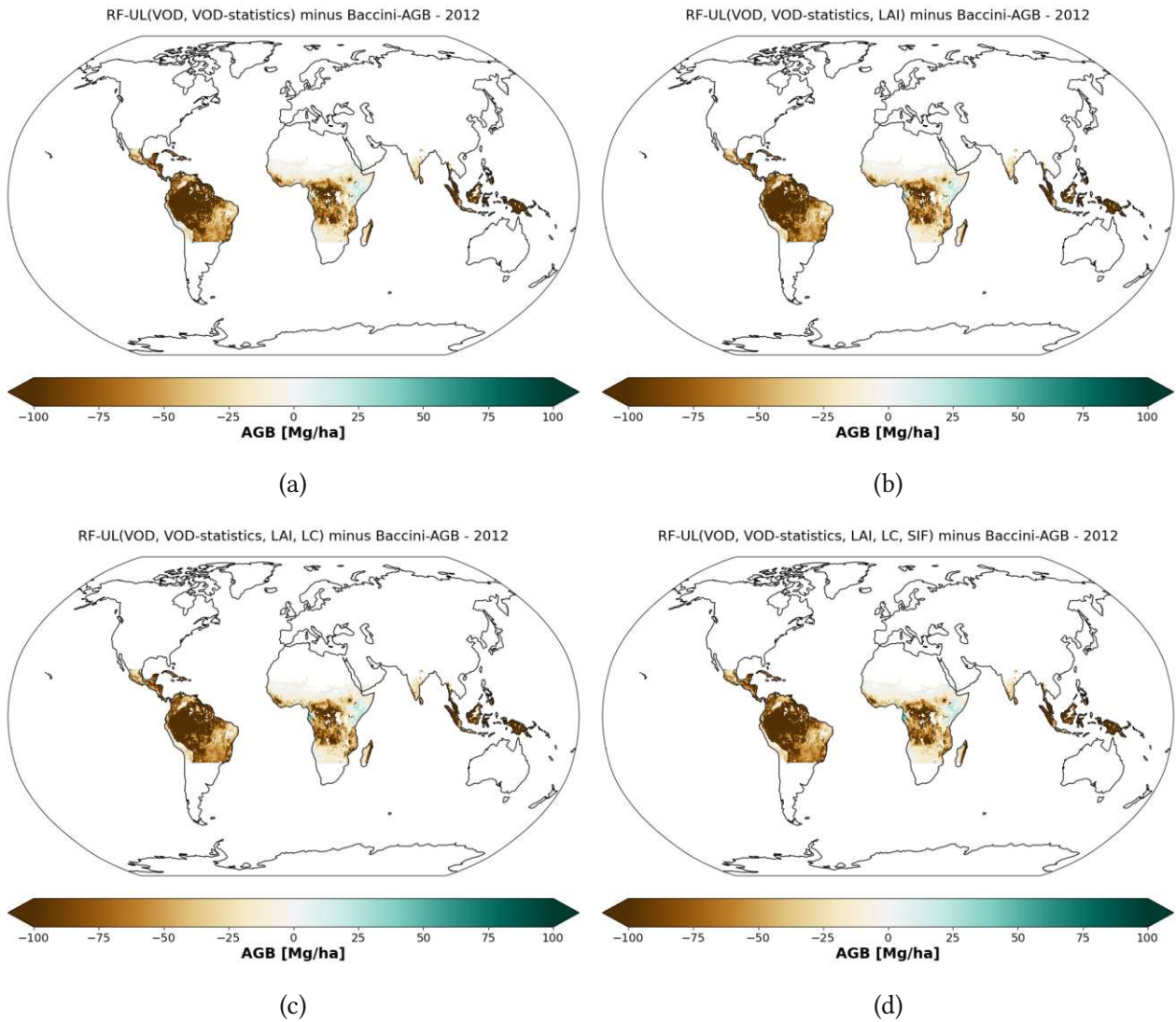
4.3. Assessment of change patterns in predicted AGB

In general, AGB estimates for low vegetation show a much better agreement with the reference data than estimates for high and dense vegetation (Figure 21, 22). The best agreement can be observed for crops, closely followed by shrubs. Conversely, the lowest agreement between predictions and reference data exists for forests, especially for the broadleaf evergreen class.

If we look at the AGB change within the broadleaf evergreen class, we can see that the curves for the base models are quite far from the reference both in terms of pattern and magnitude of change (Figure 21, 22). Both the model using VODCA statistics and the model using only VODCA get very similar results. By adding extra variables, the magnitude step by step approaches similar levels as the reference, and also the pattern becomes more similar. The models that get closest to the reference are the models relying on a combination of VOD, VOD statistics, LAI and LC.

The broad leaf evergreen class has a strong jump in the predicted AGB change in 2015 (Figure 21). A possible explanation for this could be flood events (Espinoza et al., 2022) since no correction was done for them in the VOD data. Therefore, this anomaly is likely the result of artifacts in the VOD data and not caused by real AGB change.

For the deciduous broadleaf class, the best match is again found for the models using LC information. The pattern and magnitude are quite similar for this class. The agreement of the magnitude of the AGB change between predictions and reference is however visibly lower compared to the broadleaf evergreen class.

For needle leaf forests, the best agreement both for total AGB and yearly AGB change can be found for the models using LC without SIF.

The same is the case for shrubs and crops. The agreement both for total AGB and yearly AGB change is good for both of these classes. The bare soil class shows very good agreement for both total AGB and yearly AGB change for the models using LC.

Overall, the models using additional LC information show the best results. Models relying only on VOD or VOD+VOD statistics show the largest differences between predictions and reference data. Overall we have some classes with a good agreement (bare soil, needle leaf, shrubs, crops), decent agreement (broadleaf deciduous), and low agreement (broadleaf evergreen).
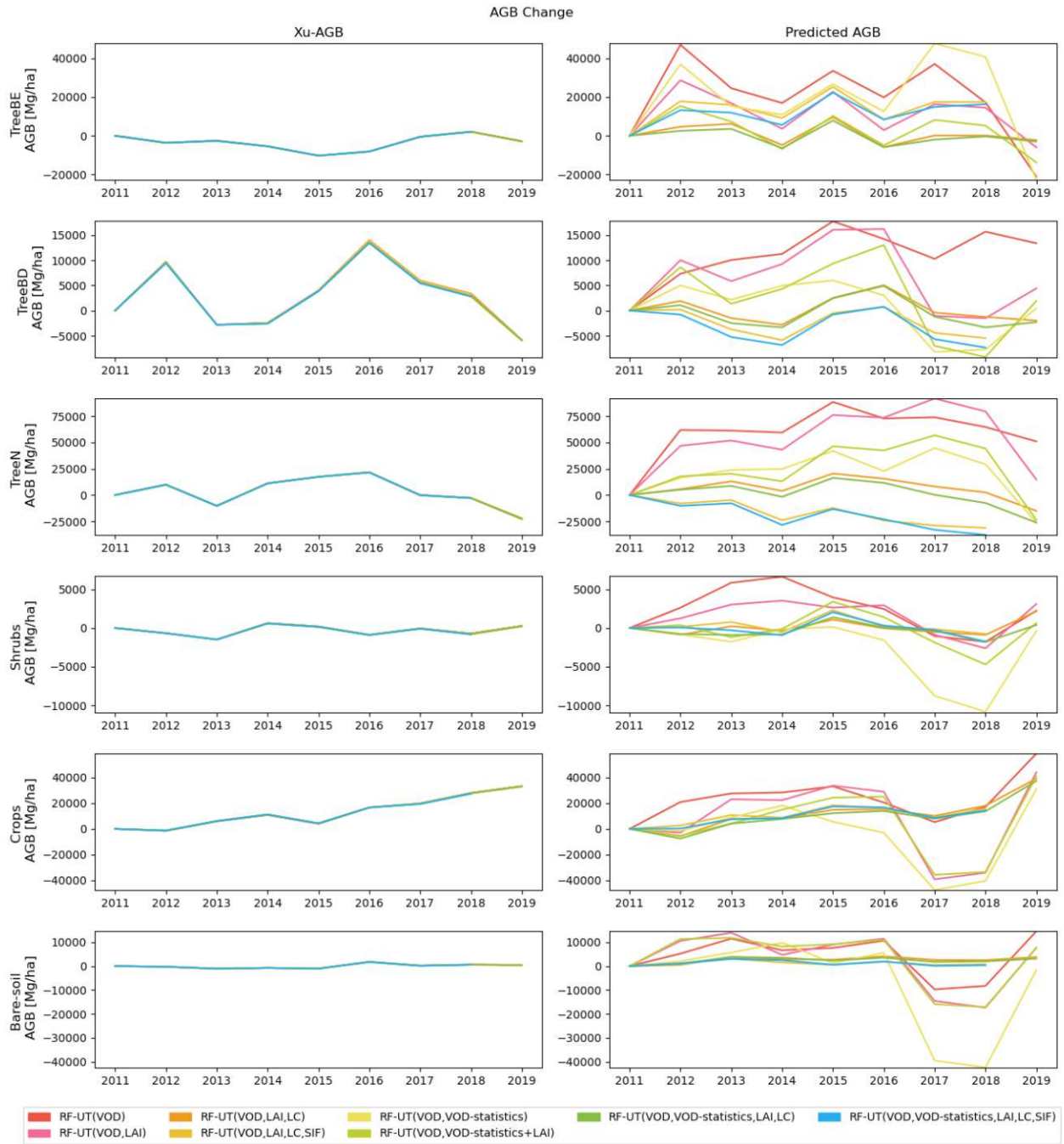
Figure 21: Comparison of yearly the AGB change per dominant land cover class from model predictions of unknown time periods and reference data from Xu et al. (2021).
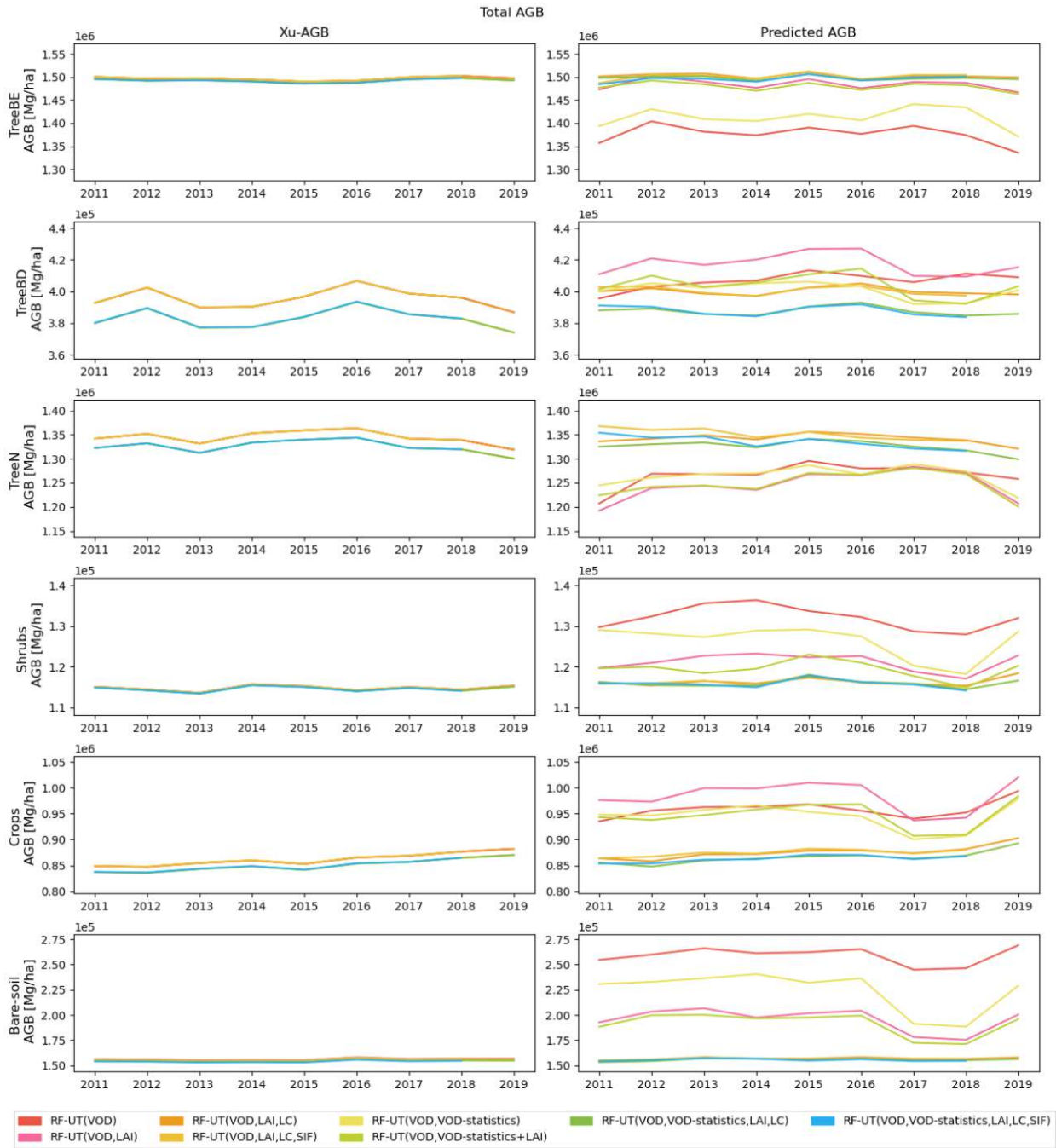
Figure 22: Comparison of yearly the total AGB per dominant land cover class from model predictions of unknown time periods and reference data from Xu et al. (2021).

The per-pixel AGB changes for the Amazon region (Figure 23, 24, 25) show large differences between reference data and the model predictions made for unknown time periods, both in terms of magnitude and the spatial distribution of changes. The agreement is lowest for the simpler models using a combination of VOD, VOD statistics, and LAI (Figure 23a, 24a, 23b, 24b), and even

though the other models using additional (Figure 23c, 25a, 24c, 25b) features show slightly better agreement, they are still far from the reference data.

Figure 23: Comparison of temporal per-pixel AGB changes in the Amazon region between Xu-AGB (Xu et al., 2021) and model predictions: a) RF-UT(VOD), b) RF-UT(VOD, LAI), c) RF-UT(VOD, LAI, LC). The AGB change for Xu-AGB can be seen in d).

Figure 24: Comparison of temporal per-pixel AGB changes in the Amazon region between Xu-AGB (Xu et al., 2021) and model predictions: a) RF-UT(VOD, VOD-statistics), b) RF-UT(VOD, VOD-statistics, LAI), c) RF-UT(VOD, VOD-statistics, LAI, LC). The AGB change for Xu-AGB can be seen in d).
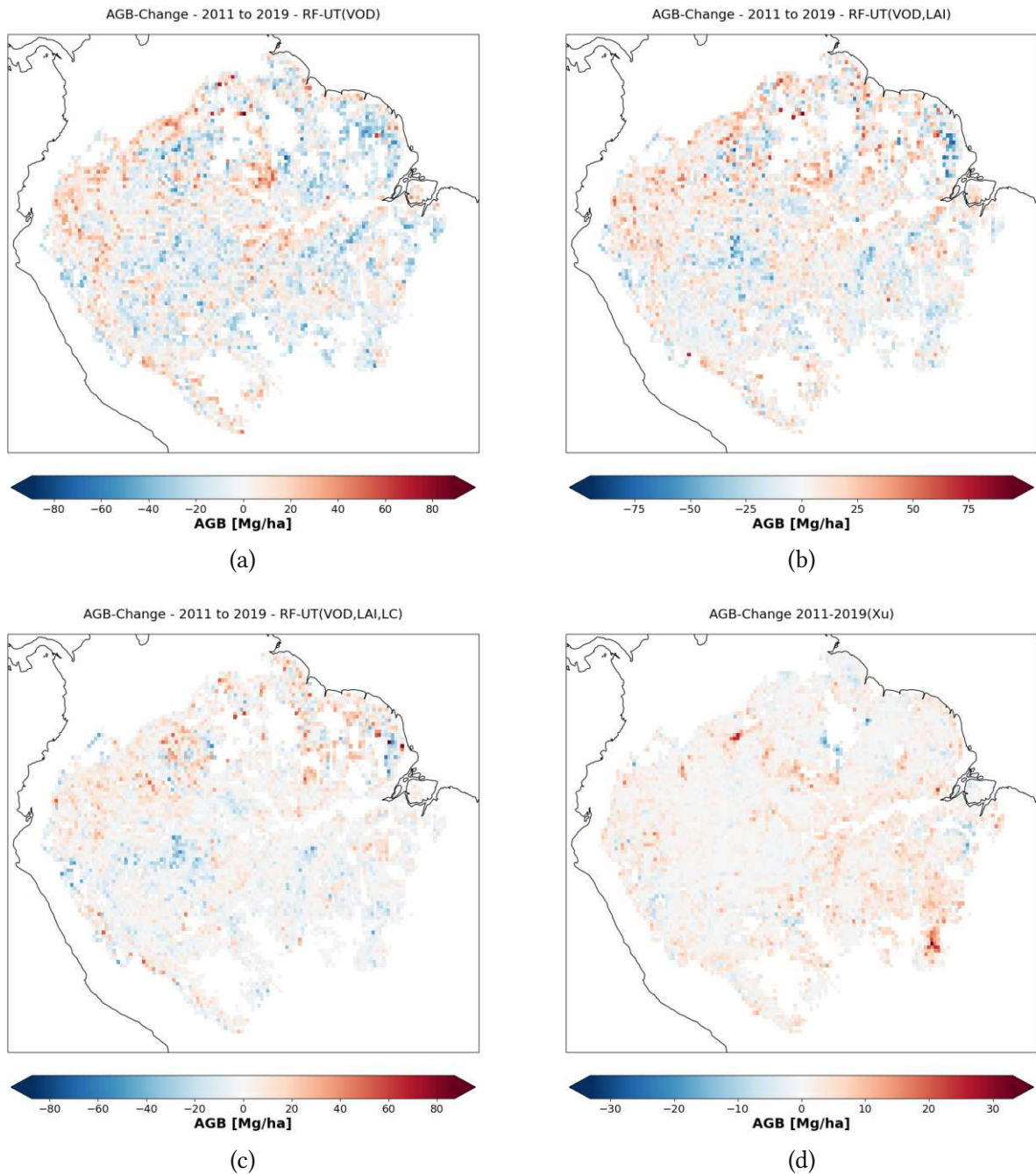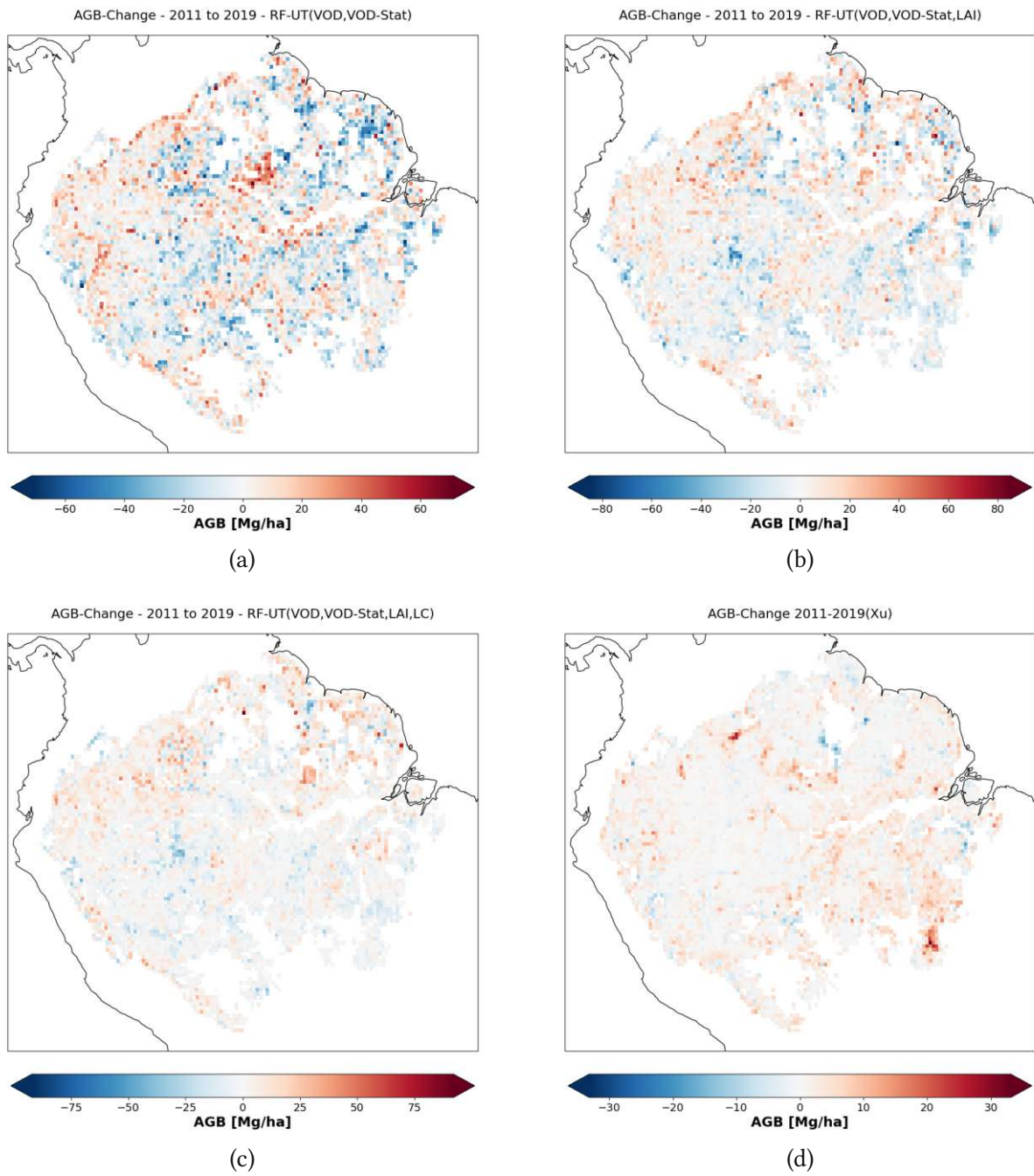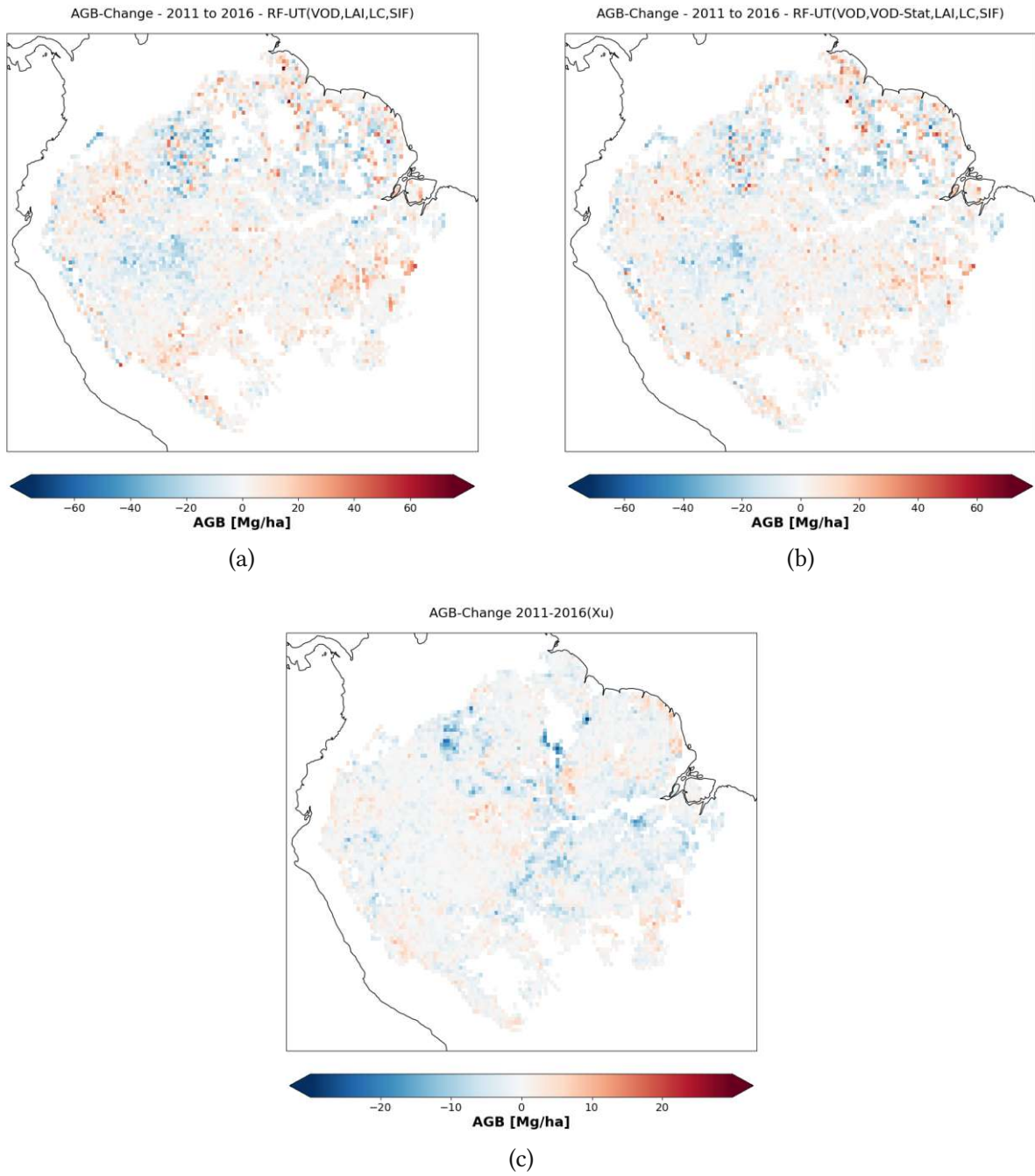
Figure 25: Comparison of temporal per-pixel AGB changes in the Amazon region between Xu-AGB (Xu et al., 2021) and model predictions: a)RF-UT(VOD, LAI, LC, SIF), b) RF-UT(VOD, VOD-statistics, LAI, LC, SIF). The AGB change for Xu-AGB can be seen in d).

5. Discussion

5.1. Univariate regression approach vs. random forest approach

If we compare the R^2 scores (Table 4), the non-parametric RF approach clearly outperforms the univariate parametric regression approach by Rodríguez-Fernández et al. (2018), even in the univariate setup using only L-VOD as a predictor variable.

Global linear, monotonic, and bivariate regressions have difficulties to capture the relationship between VOD and AGB (Schmidt et al., 2023). In order to capture the relationship, non-linear interactions among different ecosystem properties have to be considered (Schmidt et al., 2023). Therefore, this might explain why the RF approach outperformed the univariate regression approach by Rodríguez-Fernández et al. (2018). Furthermore, some RF models also rely on additional predictor variables, thus increasing the prediction accuracy even more. In particular, land cover information proves to be very beneficial for the prediction, as can be seen in Table 4.

Fan et al. (2019) conducted a similar study to Rodríguez-Fernández et al. (2018) by calculating R^2 scores between predictions from univariate regression models and reference AGB values for the tropics. The R^2 scores achieved by Fan et al. (2019) are similar to the performance of some RF models (using only VOD, LAI) in this work, but lower than the more complex models used here. The results are however much better compared to the univariate regression approach in this thesis. The better results obtained by Fan et al. (2019) might be explained by the fact that Fan et al. (2019) used a smaller study area, which could result in less land cover variation. This is important because the VOD-AGB relationship per LC class is linear, but nonlinear on a global scale (Rodríguez-Fernández et al., 2018). This is consistent with the fact that LC is the most important feature for the models using LC information (Figure A.10, 10, A.11, 11).

The fact that RF models with less complex feature constellations (only VOD, LAI, VOD statistics) already achieve similar R^2 scores globally as Fan et al. (2019) for the tropics shows strong support for the random forest approach.

Liu et al. (2015) also used a univariate regression approach to predict total AGB values for different biomes globally. Their results are comparable to the results achieved in this thesis for the AGB time series per land cover (Figure 22), although the calibration and evaluation of the models were done on different AGB datasets. In this study, the same dataset was used for both calibration and evaluation. Moreover, Liu et al. (2015) relied on an alternative approach to establish the VOD-AGB relationship by only using low-uncertainty locations on the reference AGB map.

The similar performance of the univariate regression approach and the RF models might be explained by averaging effects when calculating total AGB over a certain biome. It is therefore plausible that RF models and univariate regression models can achieve similar results for the estimation of total AGB over large areas. In fact, Liu et al. (2015) analyzed the effect of aggregation on random errors and found the latter to be reduced when aggregation was applied.

5.2. Residuals between predicted and reference AGB

The residual maps (Figure 17, 18) show a strong underestimation of AGB in the tropics, especially in the Amazon and Congo basins. This is in line with findings from previous studies (Fan et al. (2019), Avitabile et al. (2016)), which identified the tropics as the area with the highest prediction uncertainties, with an RMSE up to 60 $MgCha^{-1}$ for some areas (Fan et al., 2019). These high uncertainty areas (Congo basin, Eastern Amazon basin, Borneo), described by Avitabile et al. (2016), overlap with the low-performance areas in our results (Figure 17, 18). The low performance areas in the models also largely overlap with high-uncertainty areas in Xu-AGB (Xu et al., 2021), especially for the RF models not using land cover information.

In addition to dense vegetation, the presence of water bodies in the VOD observation footprint and residual atmospheric effects might also reduce the model performance. Water bodies in the observation footprint can lead to an underestimation of VOD (Liu et al., 2013), which subsequently could compromise the AGB estimation. Historical flood records (Espinoza et al., 2022) for the port of Manaus (Amazon basin) show pronounced flood events during the time period of interest. The effect of these flood events can possibly be seen in the Amazon region, where it is possible to see parts of the stream in the form of strong underestimation on some residual maps (Figure 17a, 18a).

Another reason for reduced performance in tropical areas might be the complete saturation of higher frequency VOD bands due to high vegetation density, thus limiting the information that can be extracted from these bands. This effect might be the reason why the best model performance could be observed for low vegetation types, like shrubs and crops. Conversely, L-VOD does not reach saturation until AGB values of approximately 350 Mg ha^{-1} for Africa and South America (Vittucci et al., 2019).

5.3. Predictor Contribution

The feature importances plots showed that LAI is more important than L-VOD if LC information is not included in the model. This is valid both for the AGB prediction of unknown time periods and unknown locations. A possible reason for this could be that LAI is better at representing different land cover differences in the models than L-VOD. In fact, LAI seems to make a clearer distinction between areas with broadleaf evergreen forests and other land cover types compared to L-VOD (Figure 1d, 2a). Since the broad leaf evergreen LC class was identified as the most important model feature, this might explain why LAI is more important than L-VOD for some models. Interestingly, for the models making predictions for unknown time periods, the addition of VODCA statistics only improves models without LC information, which is not the case for the models making predictions for unknown locations, where all models are improved by the addition of VODCA statistics. A reason for this could be uncertainties in the LC layers of the models making predictions for unknown time periods.

In general, differences in reliability exist for VOD-based biomass estimation depending on geographic location and band frequency (Dou et al., 2023). A global assessment regarding this was made by Dou et al. (2023), who found that while VOD is reliable for approximately two-thirds of

the global land surface, there are reliability issues in the Amazon region. Additionally, they found big differences in reliability between different VOD bands, depending on the vegetation type. While L-VOD is best suited for broadleaf evergreen forests, deciduous broadleaf forests, woody savannas and savannas, higher frequency X-VOD is superior for shrublands. On top of this, Dou et al. (2023) also tested the reliability of different VOD aggregation methods and found that the 95% percentile of nighttime VOD is best suited for capturing inter-annual biomass change, regardless of the VOD band (L-VOD, X-VOD). Considering that in this thesis, this was not done for the VOD data, there might be potential to improve the model performance by using the 95% percentile of VOD instead of the 75% percentile.

5.4. Model Validation

The results of the model validation are quite good, considering that only a time span between 9 and 10 years was available to train and test the models (Figure 21-9).

The time series comparison (Figure 22) of total AGB between the model predictions for unknown time periods and the reference data shows different results depending on the prominent land cover type. Low vegetation classes perform better, just like for the bias maps (Figure 17a, 18a), which was expected from previous studies (Dou et al. (2023), Avitabile et al. (2016), Liu et al. (2015)).

One possible problem regarding the models predicting unknown time periods might be that the models were trained on a total of 3 years, of which only 2 years had global coverage. It is therefore possible that the dominant land cover distribution between training and testing data is different for the models making predictions for unknown time periods, which could lead to overfitting for certain land cover types, thus distorting the results. More consistent spatial coverage was however not possible due to missing data for L-VOD before 2015.

Incomplete spatial coverage for certain years might also affect the time series comparison since only areas with consistent coverage could be used. Since this is dependent on the data availability, there are differences for the individual models regarding the land area that was used to calculate the time series. This inconsistent spatial coverage is likely the reason why there are multiple graphs for the reference data time series (Figure 22), depending on the model input features. This is because the spatial extent for the time series calculation had to be adapted to the different spatial coverage of the individual model features.

Furthermore, this is probably the reason why the agreement between reference data and prediction is so far off for the years that were used for the model training (2017, 2018).

Considering the validation of the model predictions for unknown locations, we can say that all the models show an equally good correlation with the reference map from Baccini et al. (2012). Interestingly, the simpler RF models (VOD, VOD+VOD-statistics, VOD+LAI, VODCA+LAI+VOD-statistics) show slightly better results than the models with more complex feature constellations, however, the difference is not significantly large.

5.5. Future Improvements and Challenges

One of the main shortcomings of this work is the missing uncertainties for the AGB maps, which allow the reliability assessment of the AGB predictions. Xu et al. (2021) already calculated

uncertainty maps in their study, which could be used for this purpose.

In general, uncertainties in AGB estimation can be assessed in different ways. Liu et al. (2015) expressed the uncertainties per biome as the ratio between half the range of the 90% confidence interval (5th percentile - 95th percentile) and the mean AGB value per biome. Other studies have calculated the uncertainties as cross-validated root mean square error (RMSE) (Brandt et al. (2018), Fan et al. (2019)) or correlation coefficients (Fan et al., 2019).

A possible source for uncertainties is error propagation from the reference AGB map (Brandt et al. (2018), Fan et al. (2019)), an issue that can be avoided by using field surveys, LiDAR data, and very high-resolution satellite imagery to establish the VOD-AGB relationship (Brandt et al. (2018)). This was not possible in this study because of missing data. Other sources of uncertainties might also be the VOD retrieval algorithm itself (Brandt et al., 2018).

It is possible to assess the total uncertainties as the combination of internal and external uncertainties (Fan et al., 2019). Internal uncertainties can be associated with sampling and calibration errors (Fan et al., 2019), while external uncertainties are associated with the reference AGB maps (Fan et al., 2019).

In general, uncertainties are higher for individual pixels and are significantly reduced when a larger spatial extent is considered (Avitabile et al., 2016). For example, the uncertainties at the pixel level averaged over all continental regions were estimated to be $\pm 30\%$, while at national levels, the uncertainties were reduced to $\pm 1\%$ (Avitabile et al., 2016). This effect might also explain why it was impossible to reproduce per-pixel AGB changes from Xu et al. (2021) with our model estimates (Figure 23, 24, 25).

Other problems are the small temporal coverage of L-VOD, which creates limits for model training and testing. Furthermore, the spatial coverage of L-VOD is inconsistent throughout the observation period because of the different spatiotemporal coverage of SMOS and SMAP.

Another possible impact might come from water bodies in the VOD observation footprints. Even though an effort was made to correct for this by using a static water mask, flood events were not masked out and could therefore impact the VOD signal.

The coarse resolution of the VOD data leads to a lot of different influences on the VOD signal for single pixels (Brandt et al., 2018). VOD is generally better suited to capture large-scale temporal variations in AGB than to capture changes for individual pixels (Brandt et al., 2018). This could however change with the introduction of new Sensors.

Since a lot of the used model features are quite highly correlated with each other, multicollinearity between the different model features is also something that should be dealt with in future studies.

6. Conclusions and outlook

In this thesis, a new approach for global annual AGB estimates, based on random forest regression, was developed. The approach was tested against AGB reference data both for model predictions of unknown locations and model predictions of unknown time periods. The newly developed AGB models were compared to an older approach for AGB estimation based on nonlinear univariate parametric regression, showing the superiority of the new approach.

Analysis of global residual distributions and time series comparison showed that the best prediction results are achieved for areas with low and sparse vegetation, like shrubs and crops. Conversely, the lowest performance was observed for high and dense vegetation like broadleaf evergreen forests. The model predictions showed some very promising results when compared to reference data, with maximum R^2 scores of ca. 90 % for models making predictions for unknown locations and ca. 96 % for models making predictions for unknown time periods. The evaluation of the individual predictor contributions identified L-VOD and land cover information as the most important features for AGB prediction, consistent with previous studies. In fact, land cover information has such a strong impact that it should be included in future models when available.

Overall the new approach shows good potential for the monitoring of global AGB stocks, however, there are still some steps to be taken to improve the models. These steps include the extension of the L-VOD observation period, as well as the inclusion of new sensors with higher spatial resolution to improve the estimation of AGB changes for individual pixels. The correction for flood events should also be implemented since only static water masks were used in this thesis. Additionally, uncertainties of the AGB estimates have to be calculated to increase the comparability of the approach to other methods.

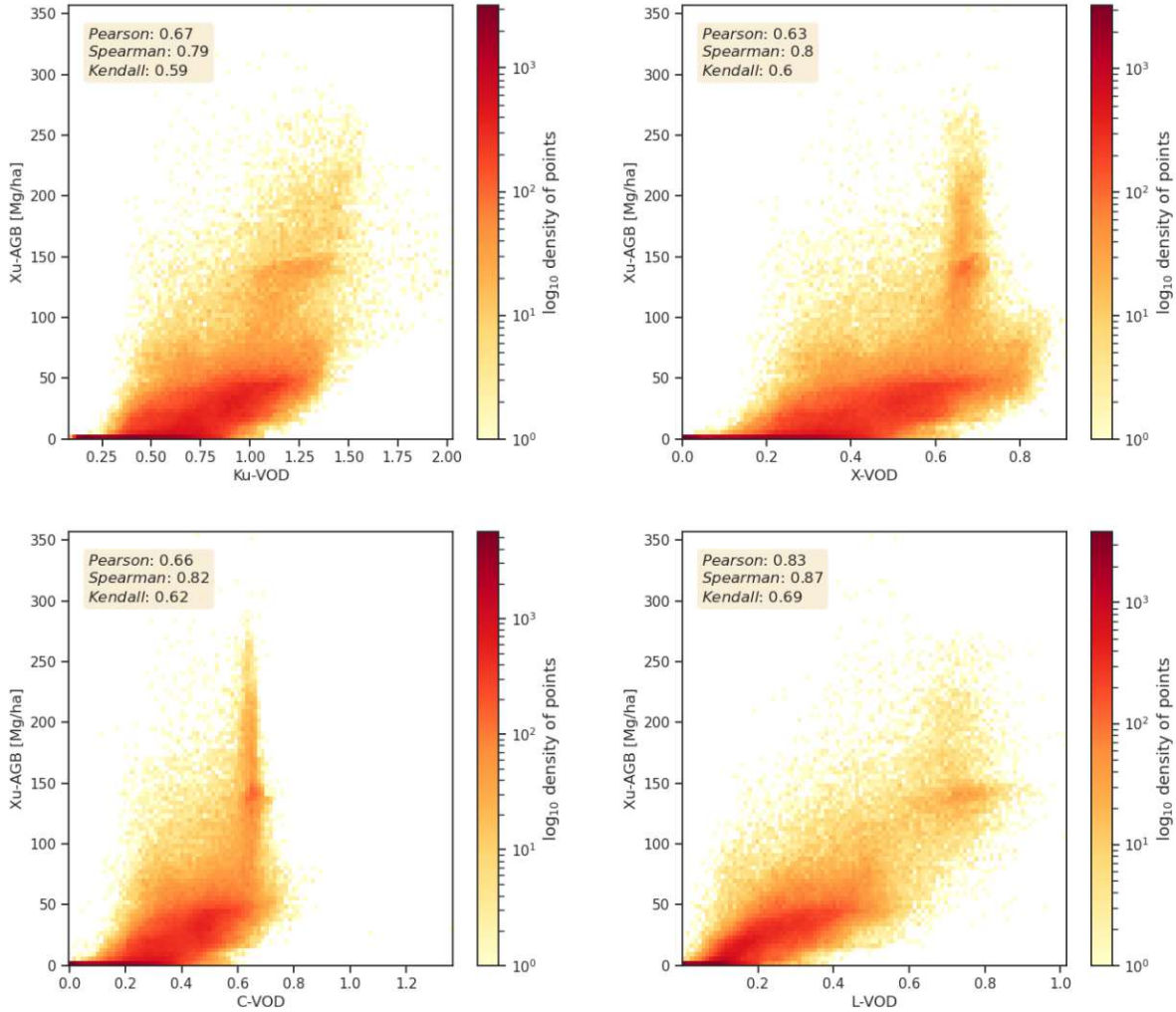# A. Appendix

VODCA-AGB relationship

Figure A.1: Relationship between individual VODCA bands (Moesinger et al., 2020) and AGB from Xu et al. (2021) for the year 2011.
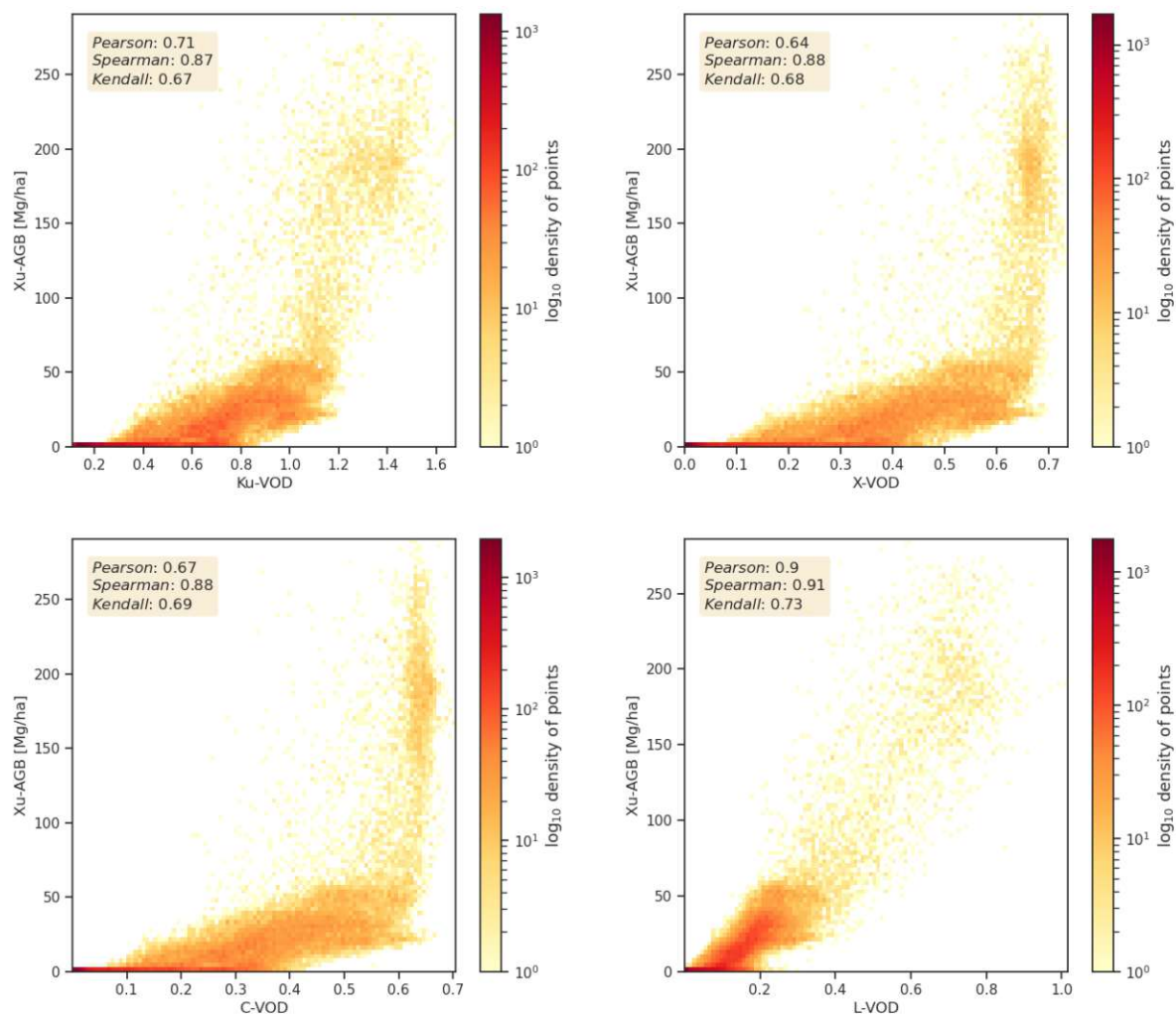
Figure A.2: Relationship between individual VODCA bands (Moesinger et al., 2020) and AGB from Xu et al. (2021) for the year 2011 on the African continent.
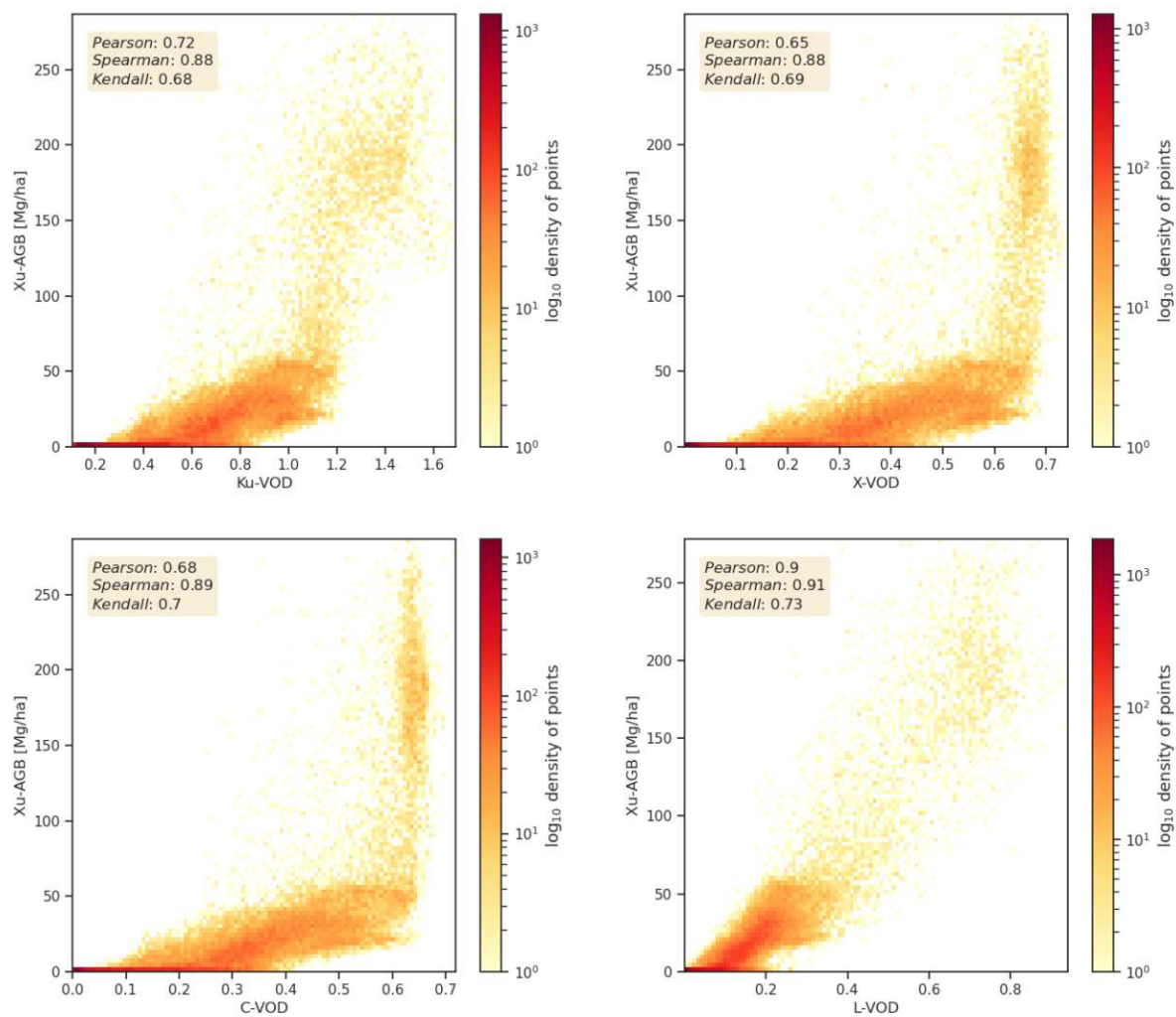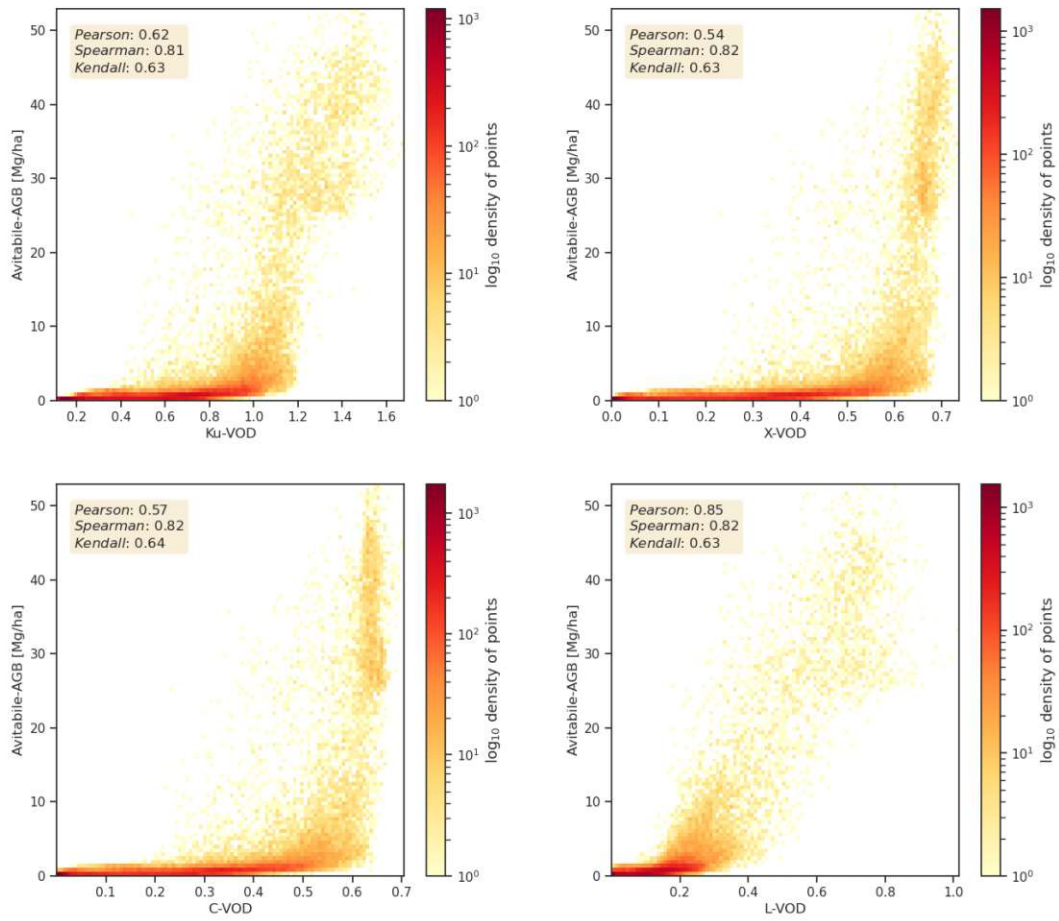
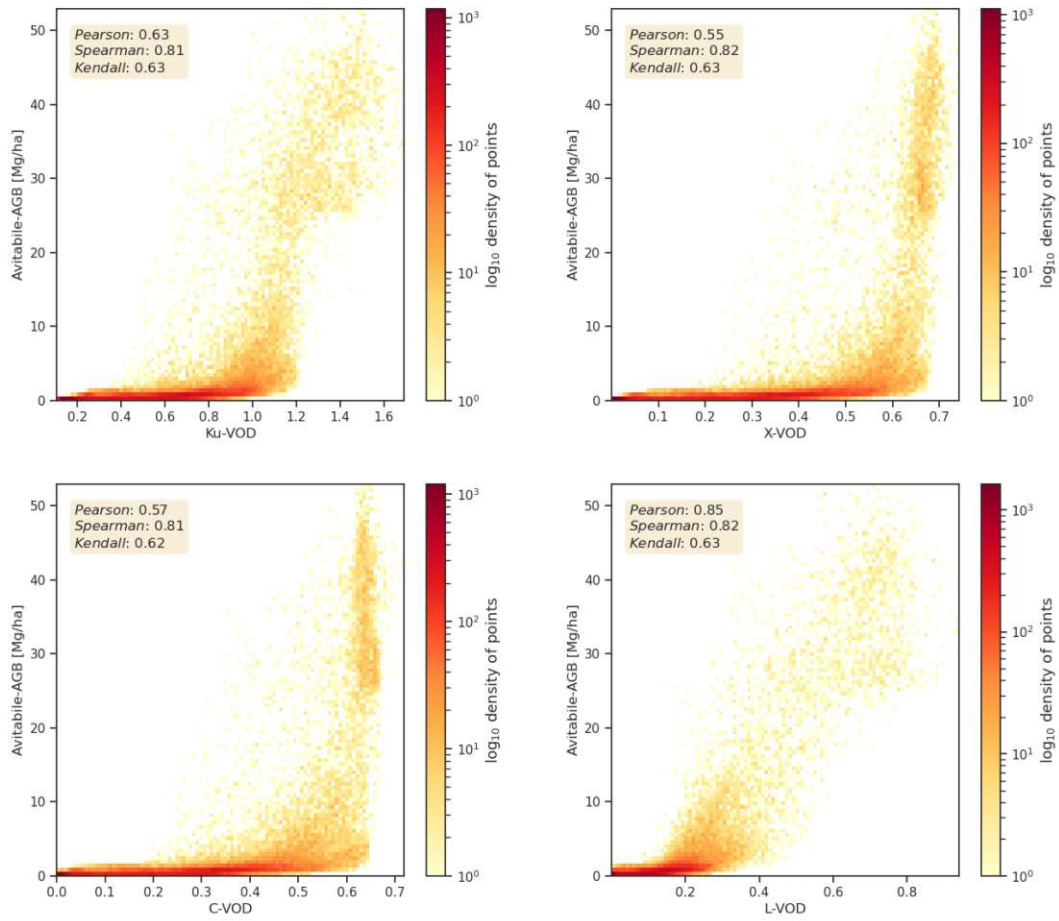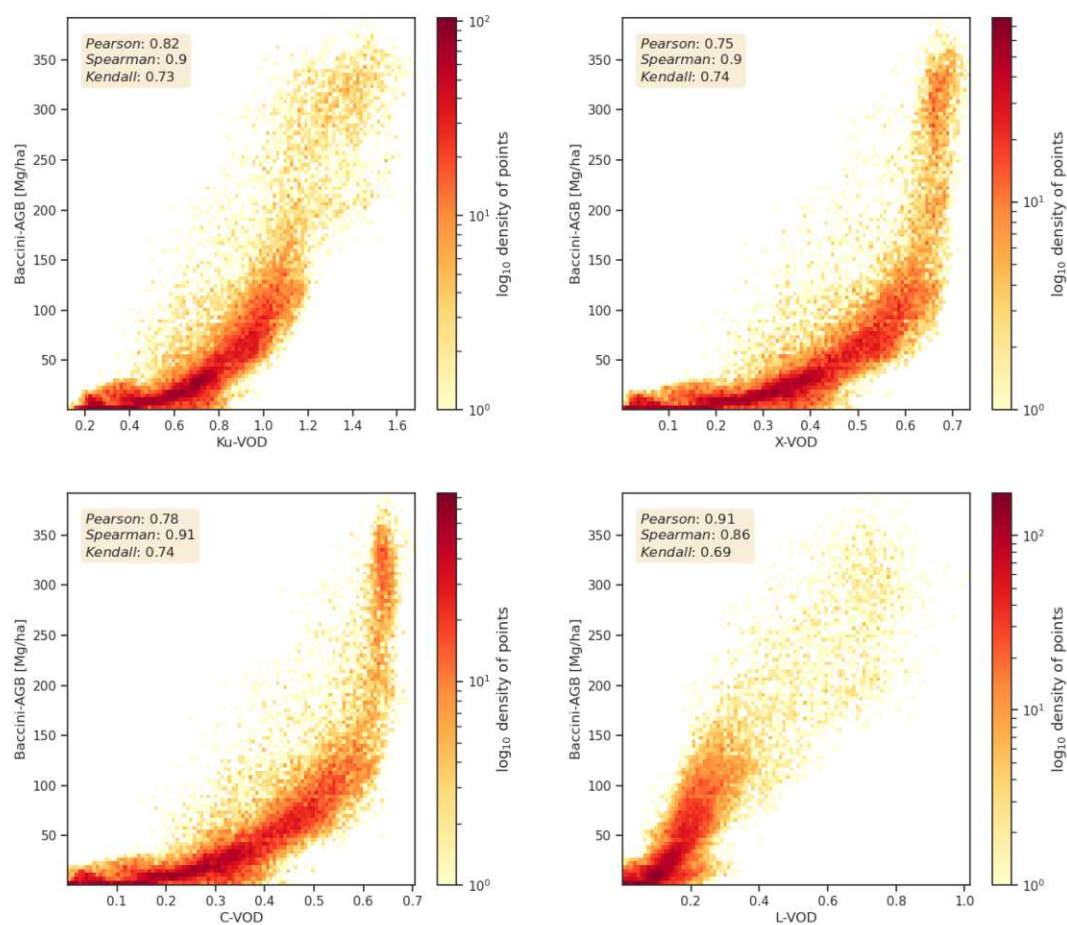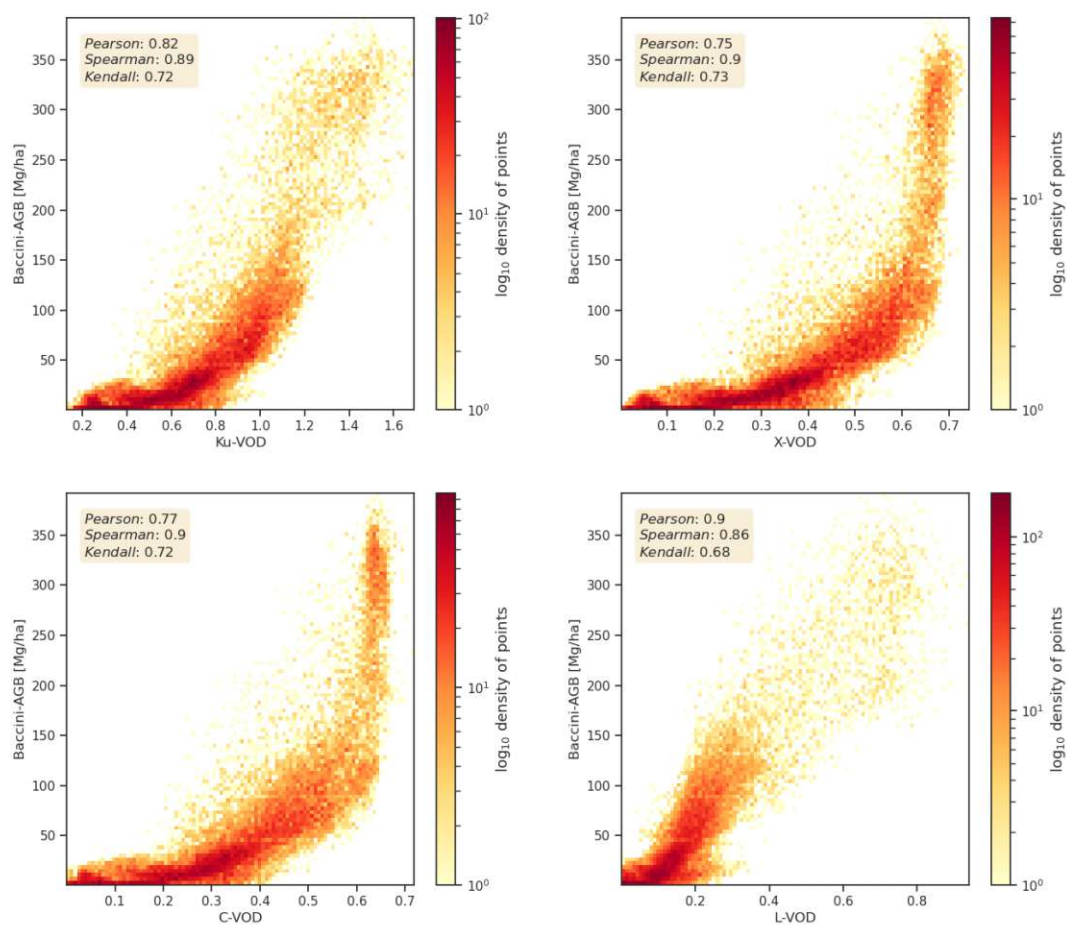Figure A.3: Relationship between individual VODCA bands (Moesinger et al., 2020) and AGB from Xu et al. (2021) for the year 2012 on the African continent.

Figure A.4: Relationship between individual VODCA bands (Moesinger et al., 2020) and AGB from Avitabile et al. (2016) for the year 2011 on the African continent.

Figure A.5: Relationship between individual VODCA bands (Moesinger et al., 2020) and AGB from Avitabile et al. (2016) for the year 2012 on the African continent.
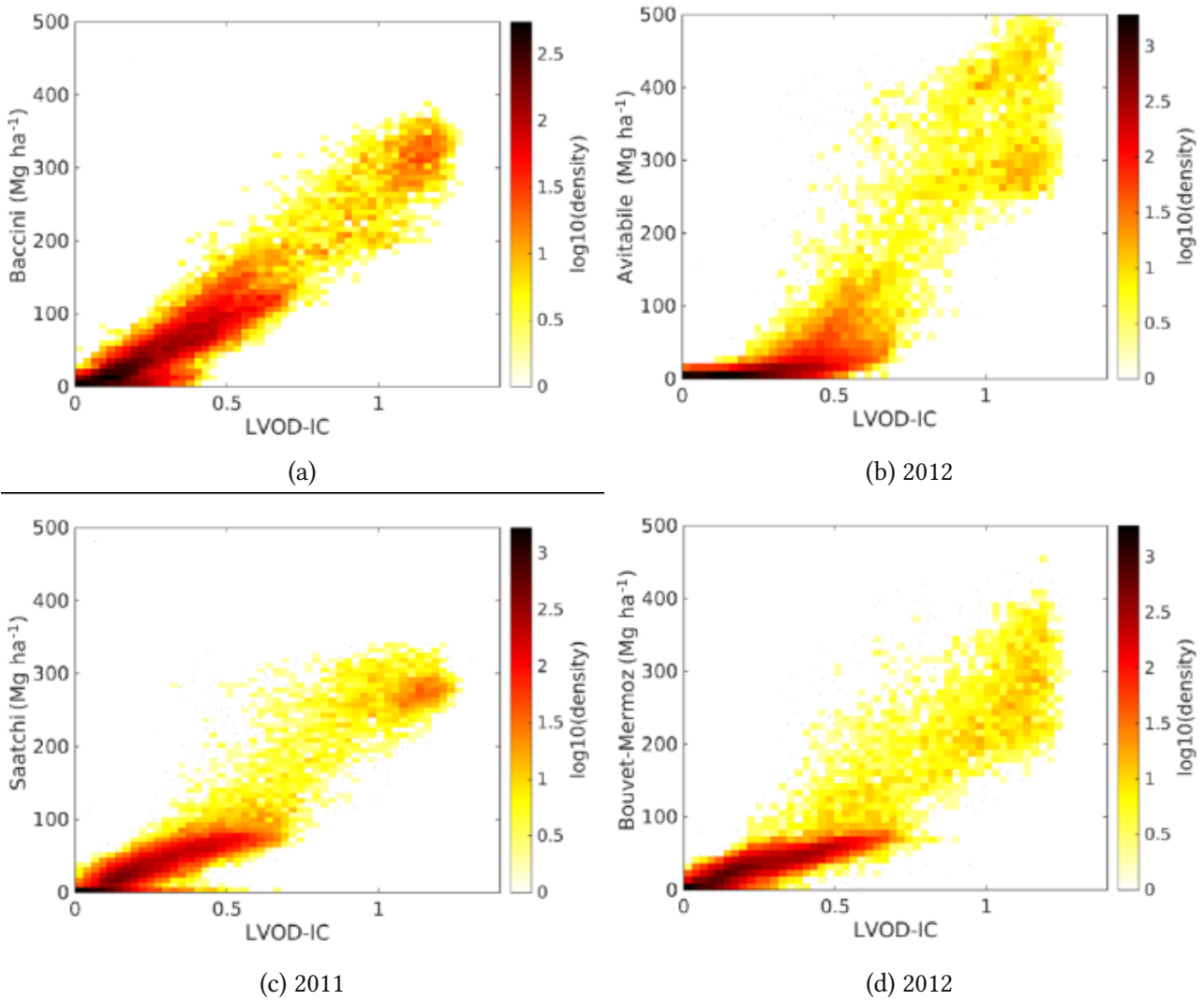
Figure A.6: Relationship between individual VODCA bands (Moesinger et al., 2020) and AGB from Baccini et al. (2012) for the year 2011 on the African continent.

Figure A.7: Relationship between individual VODCA bands (Moesinger et al., 2020) and AGB from Baccini et al. (2012) for the year 2012 on the African continent.

Figure A.8: 2D-Histogramm from Rodríguez-Fernández et al. (2018)(Figure 3) showing the relationship between SMOS-IC L-VOD and the AGB maps from Baccini et al., 2012, Avitabile et al., 2016, Saatchi et al., 2011 and Bouvet et al., 2018.

	R			ρ			τ		
	IC	iL2	L3	IC	iL2	L3	IC	iL2	L3
Avitabile	0.85	0.78	0.78	0.84	0.73	0.72	0.65	0.54	0.53
Baccini	0.94	0.87	0.87	0.90	0.80	0.77	0.74	0.62	0.60

Table 5: Correlation coefficients from Table 1 in Rodríguez-Fernández et al. (2018) between L-VOD products from SMOS and AGB maps from Avitabile et al. (2016) and Baccini et al. (2012).
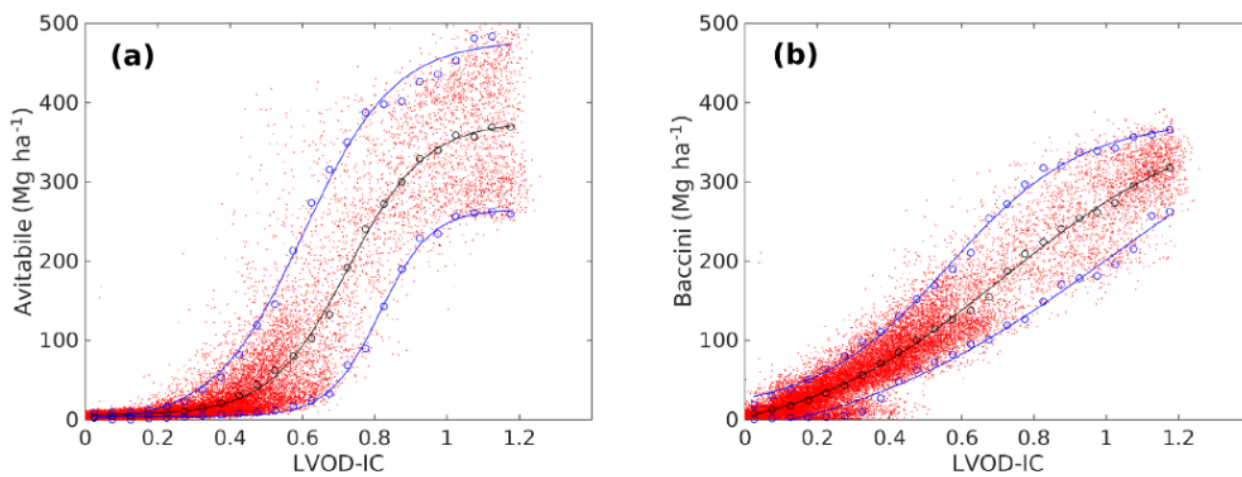
Figure A.9: Figure 5 from Rodríguez-Fernández et al. (2018) showing the fitted mean, 5th and 95th percentile curves (5) for the scatterplot between AGB (Baccini et al. (2012), Avitabile et al. (2016)) and SMOS-IC L-VOD for the years 2011-2012.
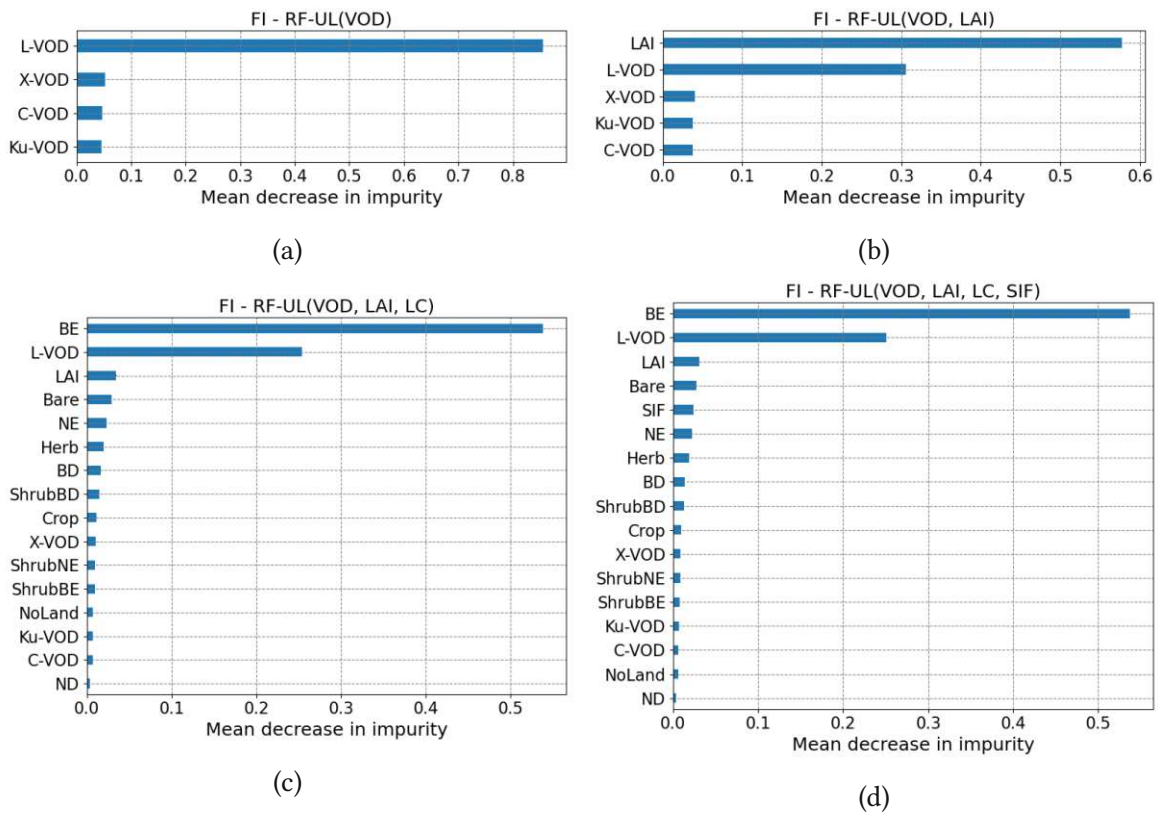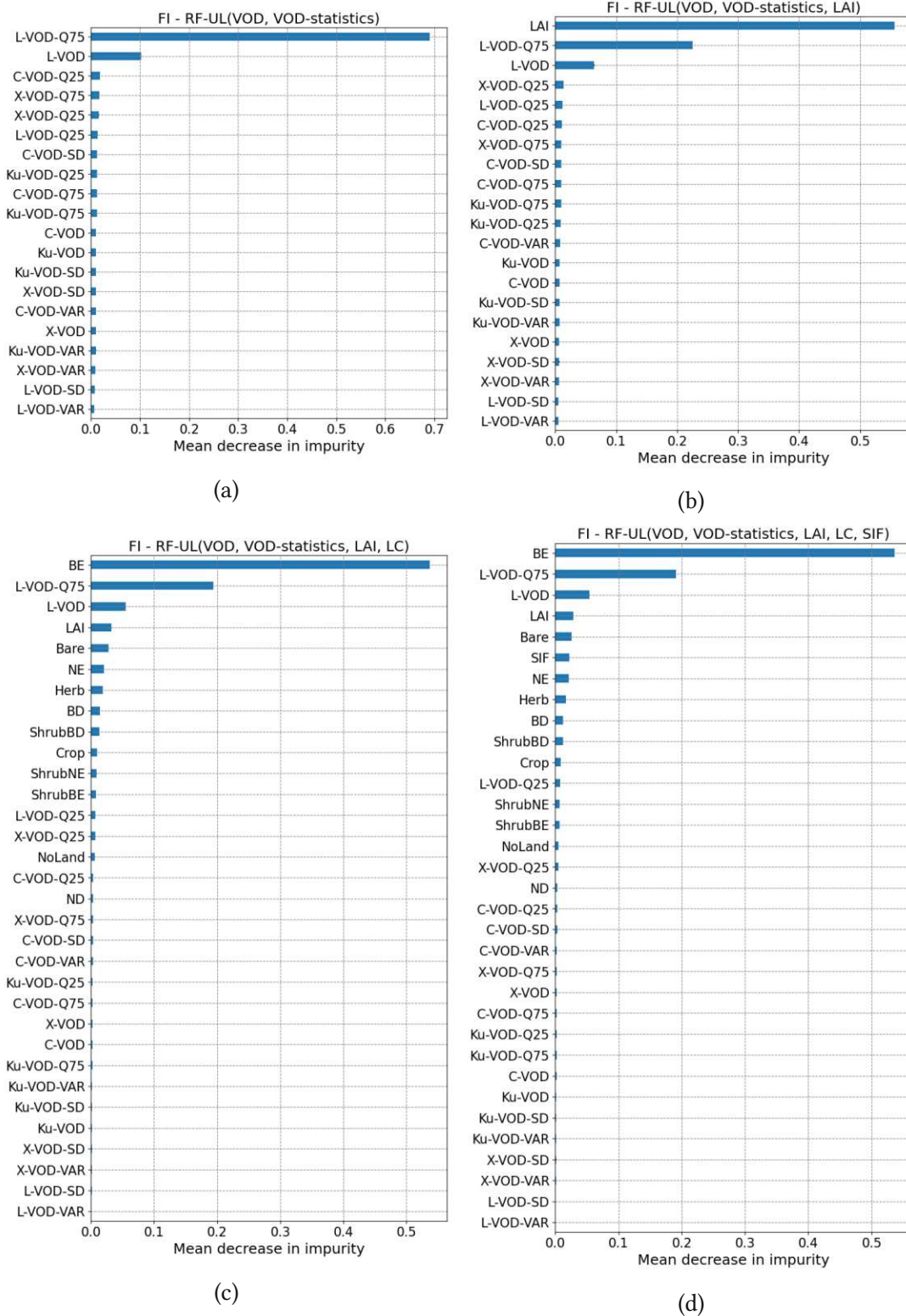
Predictor contribution

Figure A.10: Feature importances of RF models making predictions for unknown locations (RF-UL) in terms of mean decrease in impurity: a) RF-UL(VOD, VOD-statistics), b) RF-UL(VOD, VOD-statistics, LAI), c) RF-UL(VOD, VOD-statistics, LAI, LC) and d) RF-UL(VOD, VOD-statistics, LAI, LC, SIF)

Figure A.11: Feature importances of RF models making predictions for unknown locations (RF-UL) in terms of mean decrease in impurity: a) RF-UL(VOD, VOD-statistics), b) RF-UL(VOD, VOD-statistics, LAI), c) RF-UL(VOD, VOD-statistics, LAI, LC) and d) RF-UL(VOD, VOD-statistics, LAI, LC, SIF)
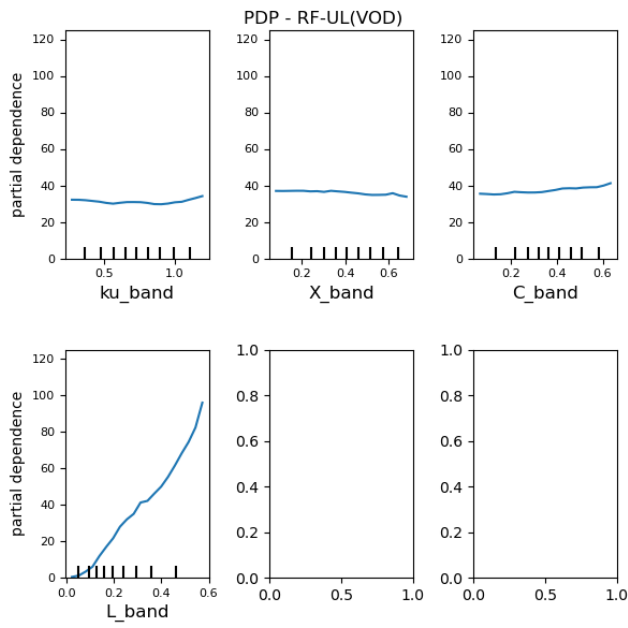
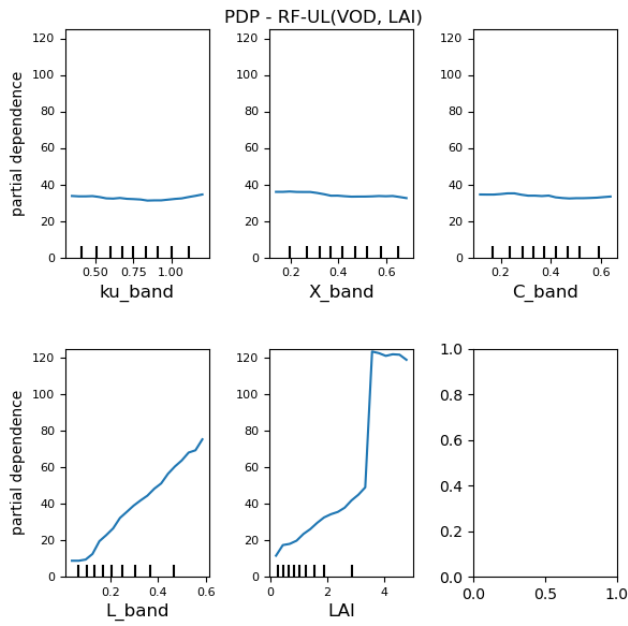Figure A.12: Partial dependencies of the model features used for RF-UL(VOD).

Figure A.13: Partial dependencies of the model features used for RF-UL(VOD, LAI).
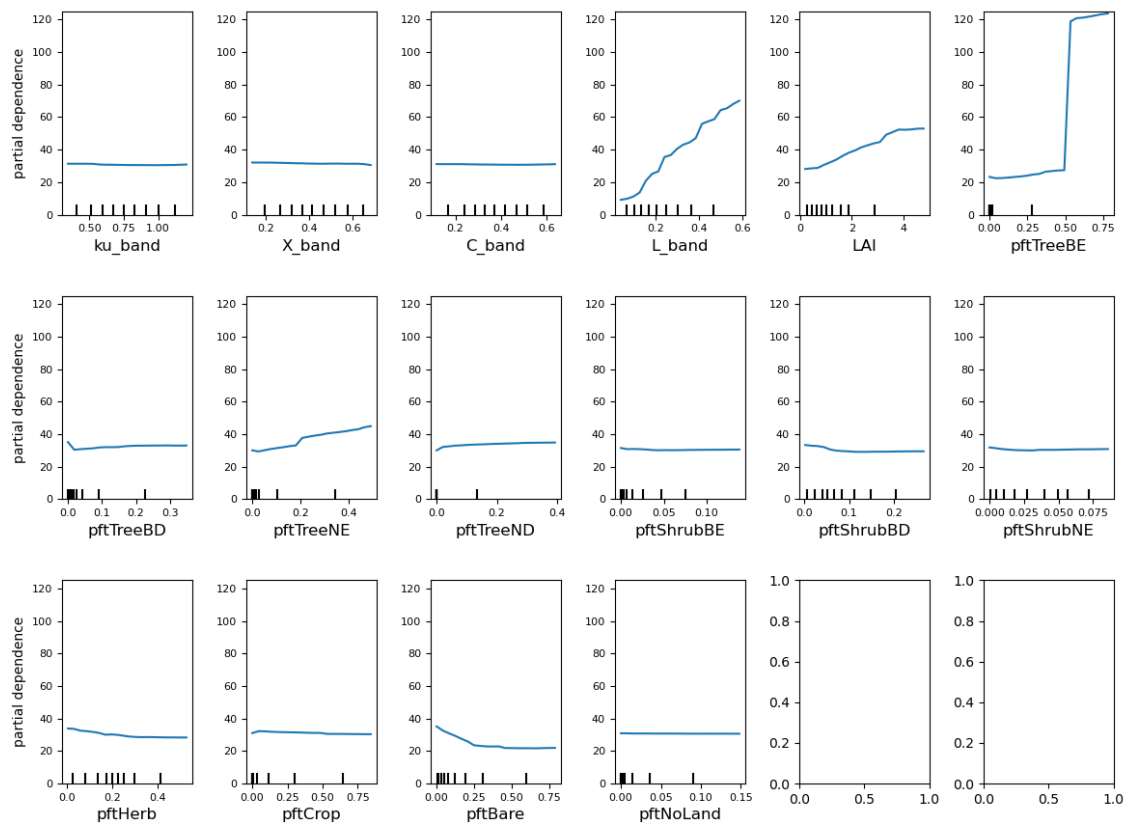
PDP - RF-UL(VOD, LAI, LC)

Figure A.14: Partial dependencies of the model features used for RF-UL(VOD, LAI, LC).
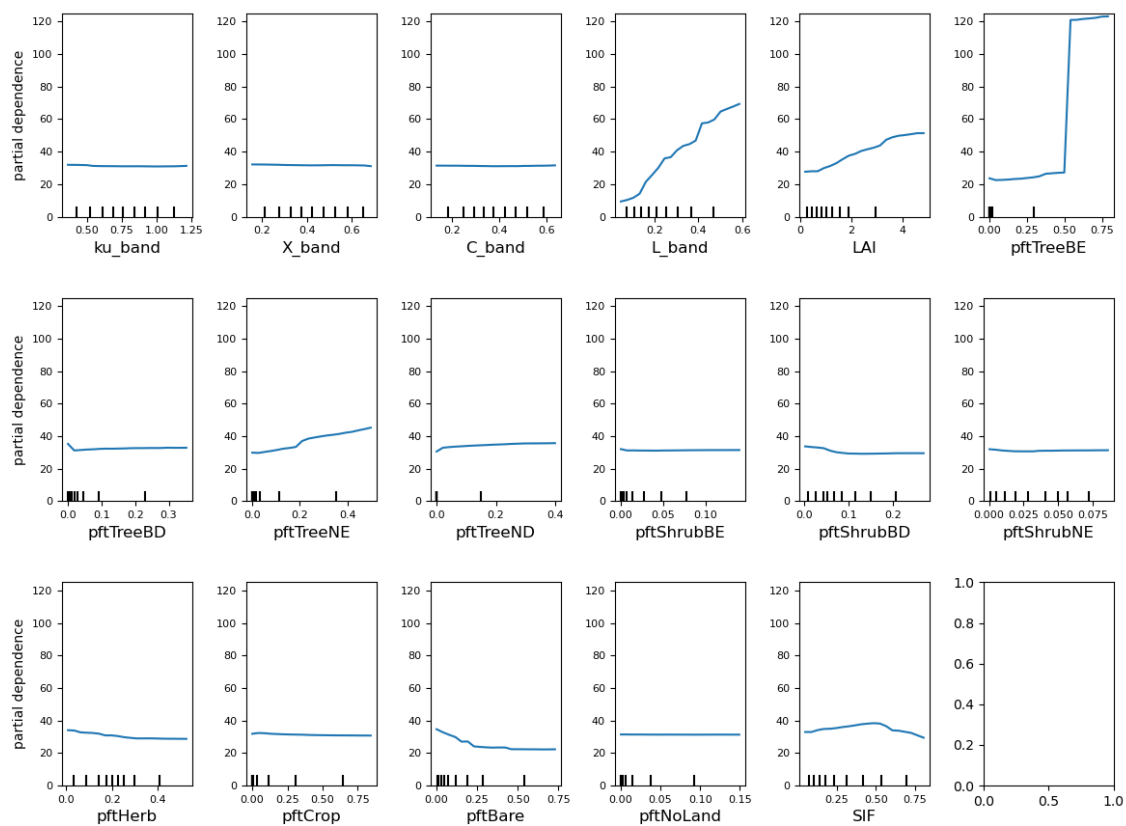
PDP - RF-UL(VOD, LAI, LC, SIF)

Figure A.15: Partial dependencies of the model features used for RF-UL(VOD, LAI, LC, SIF).
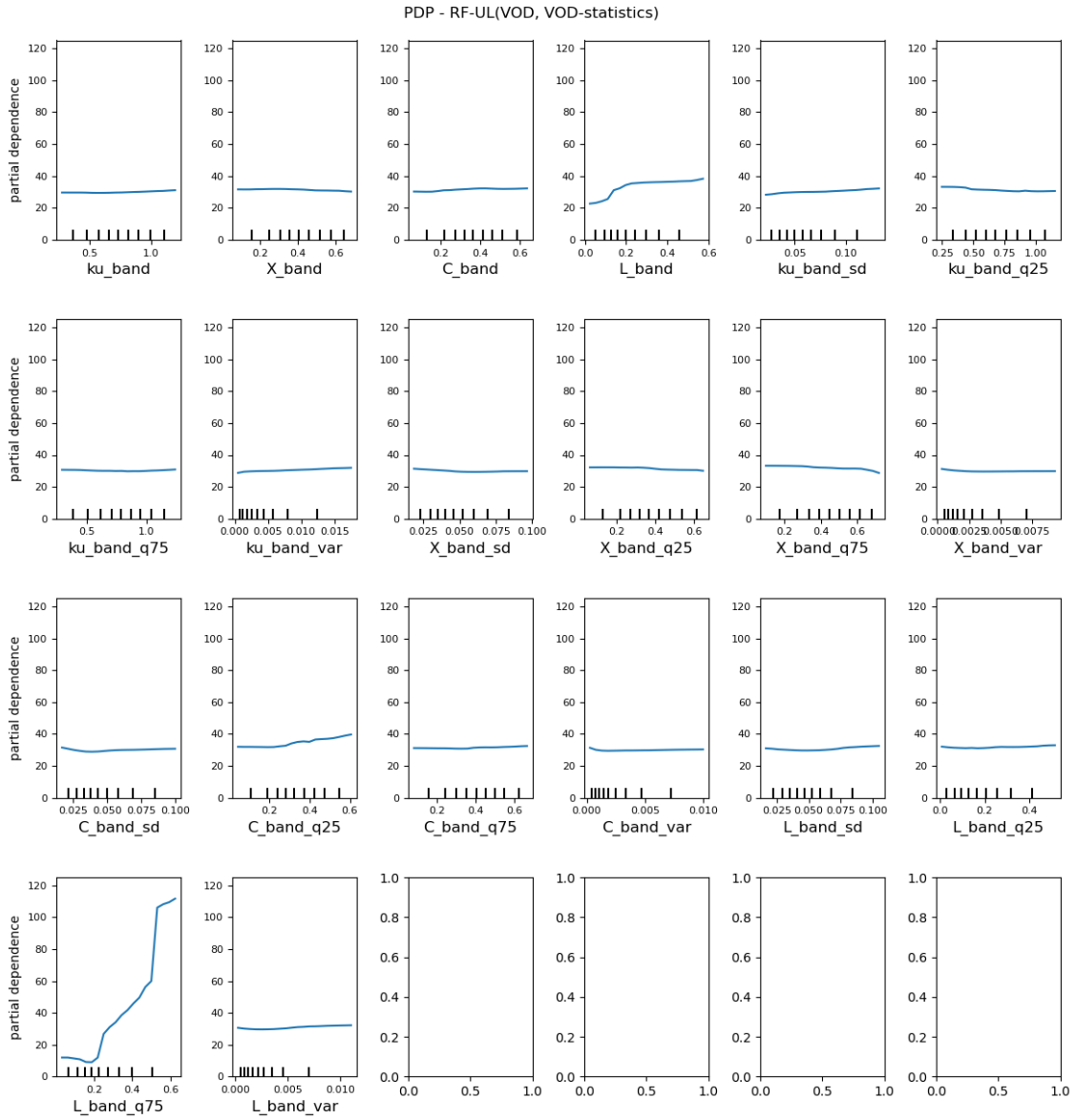
Figure A.16: Partial dependencies of the model features used for RF-UL(VOD, VOD-statistics).
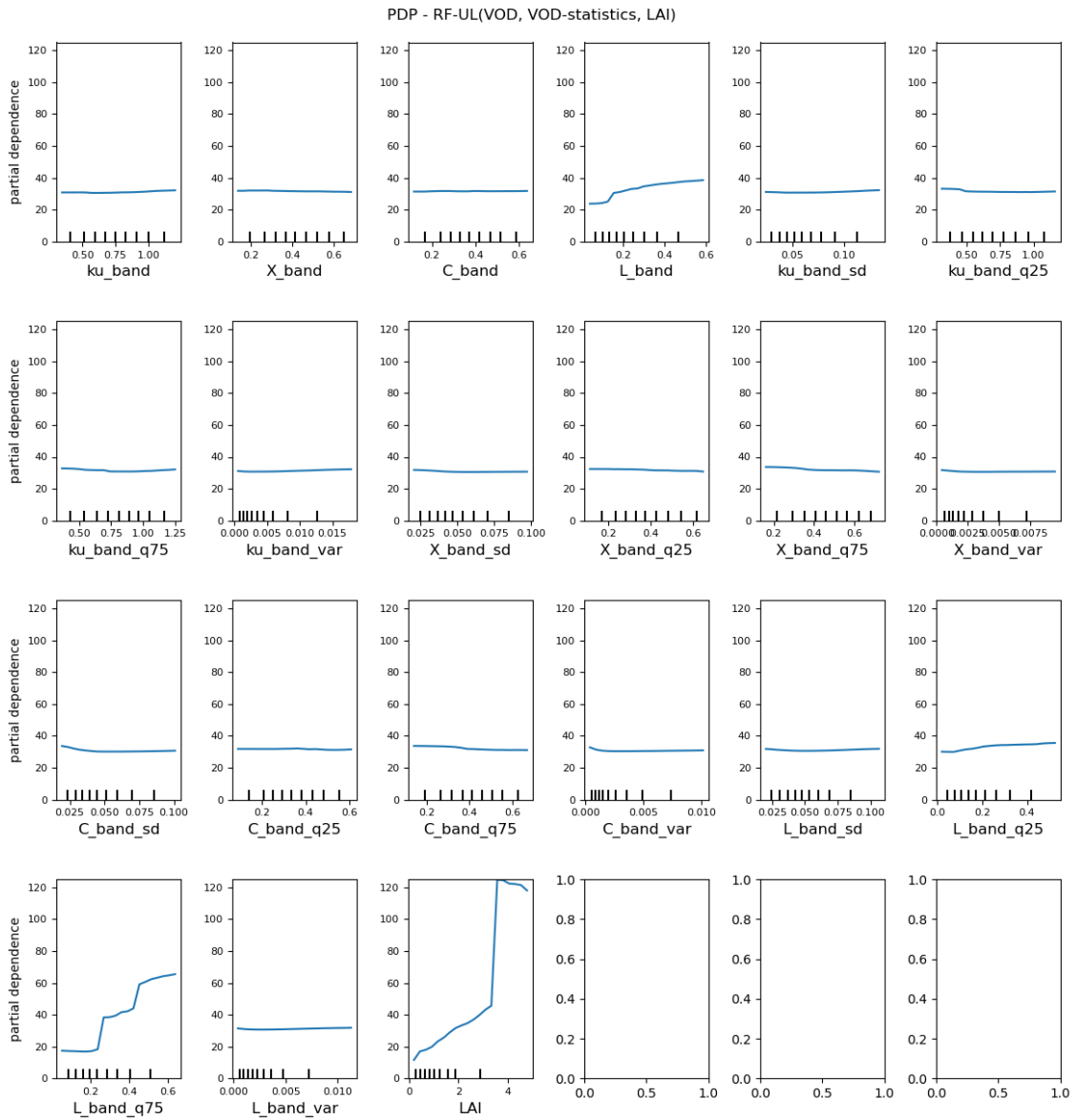
Figure A.17: Partial dependencies of the model features used for RF-UL(VOD, VOD-statistics, LAI).
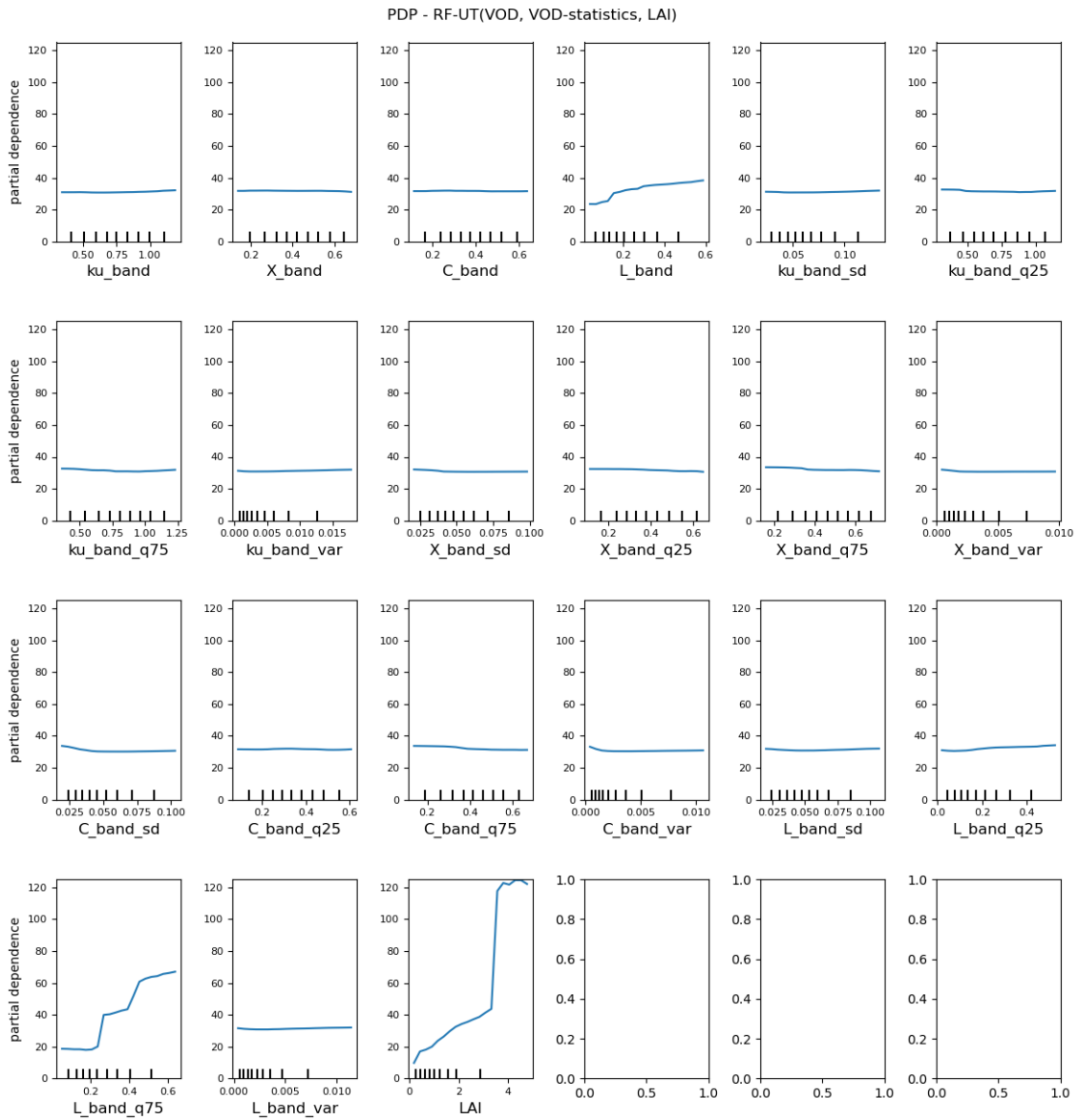
Figure A.18: Partial dependencies of the model features used for RF-UT(VOD, VOD-statistics, LAI).

Figure A.19: Partial dependencies of the model features used for RF-UL(VOD, VOD-statistics, LAI, LC).
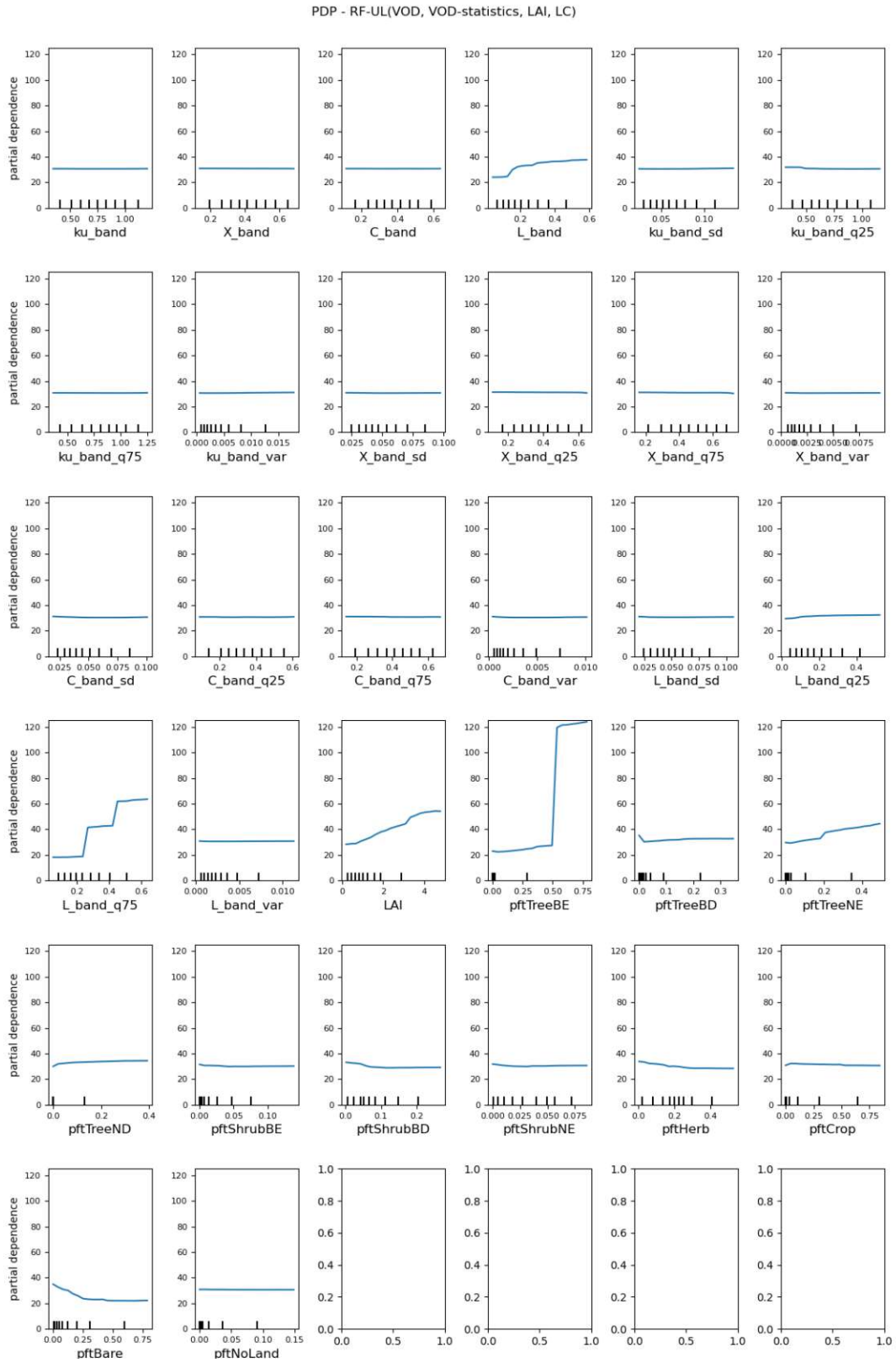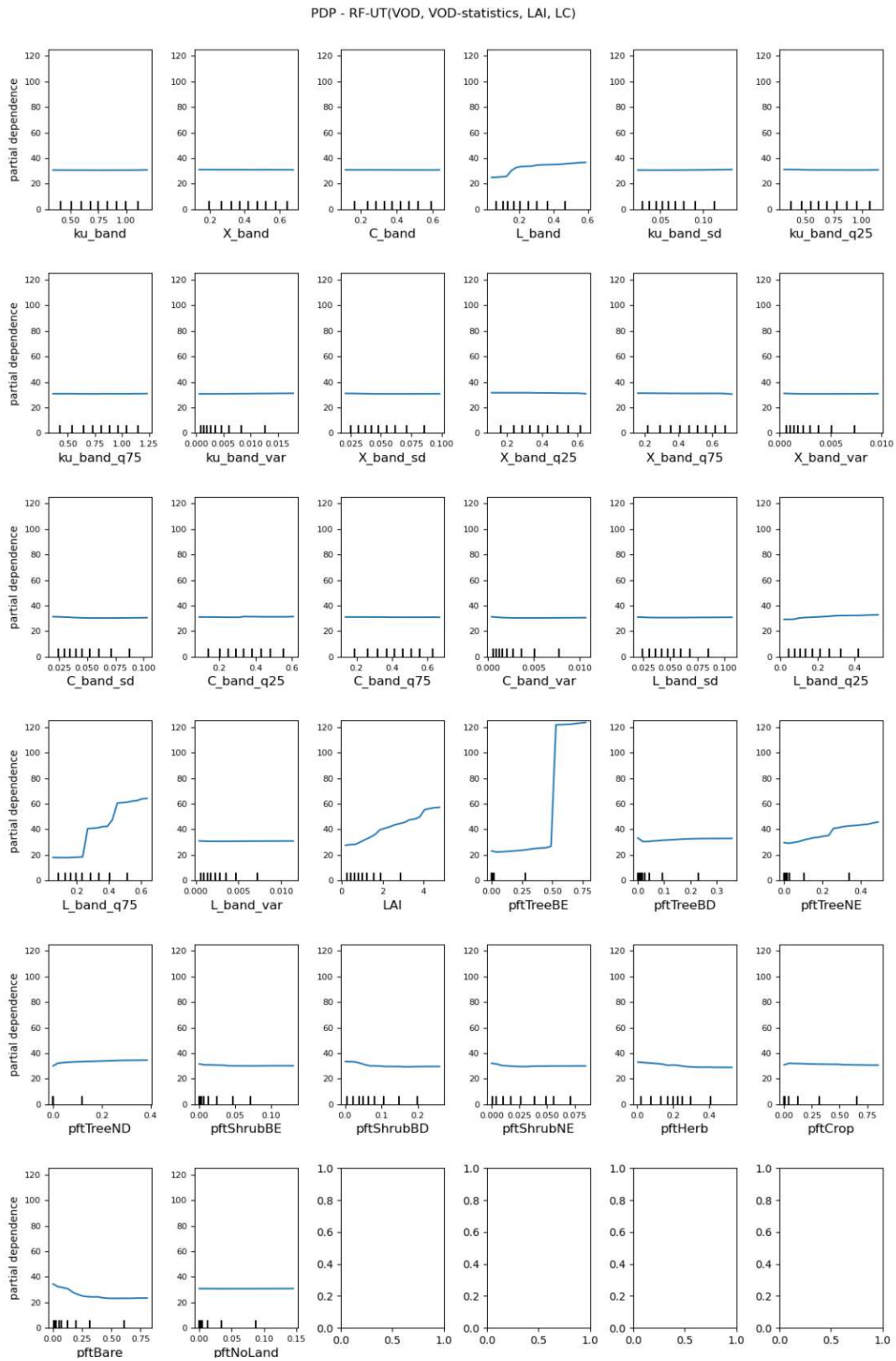
PDP - RF-UT(VOD, VOD-statistics, LAI, LC)

Figure A.20: Partial dependencies of the model features used for RF-UT(VOD, VOD-statistics, LAI, LC).
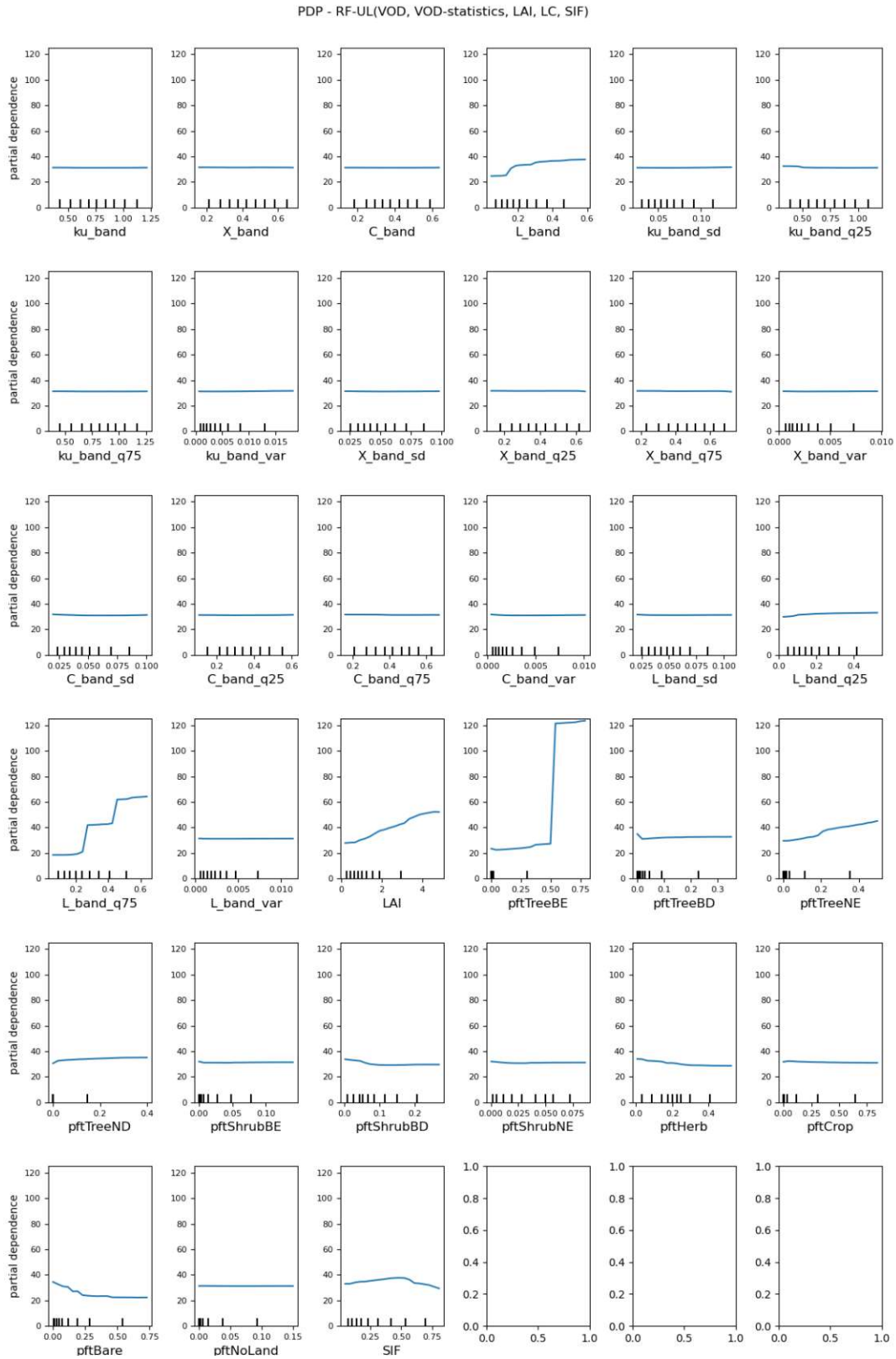
Figure A.21: Partial dependencies of the model features used for RF-UL(VOD, VOD-statistics, LAI, LC, SIF).
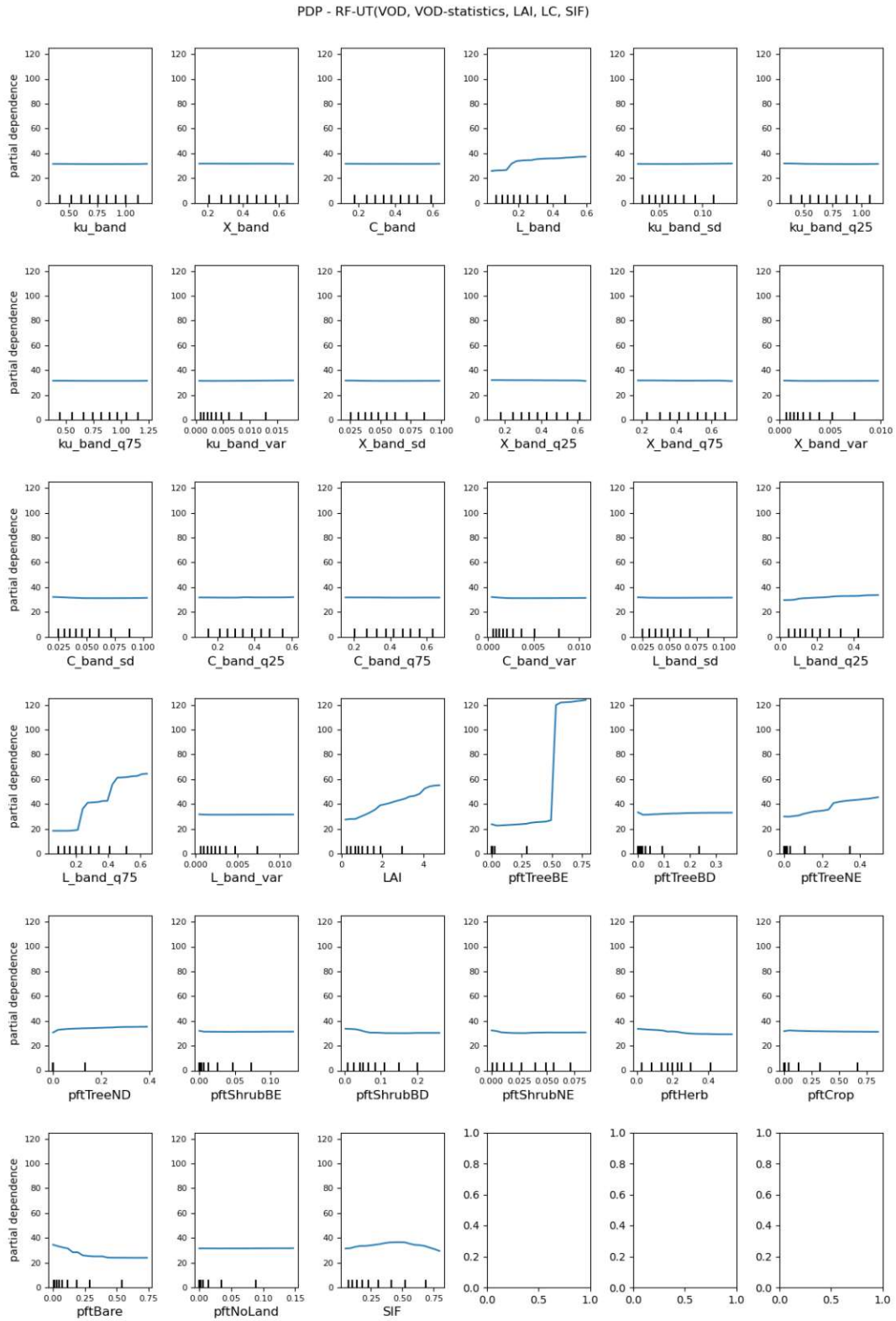
Figure A.22: Partial dependencies of the model features used for RF-UT(VOD, VOD-statistics, LAI, LC, SIF).

75

References

Avitabile, Valerio et al. (2016). "An integrated pan-tropical biomass map using multiple reference datasets". In: *Global Change Biology* 22.4, pp. 1406–1420. ISSN: 1365-2486. DOI: 10.1111/gcb.13139. URL: https://onlinelibrary.wiley.com/doi/abs/10.1111/gcb.13139 (visited on 10/13/2022).

Baccini, A. et al. (Mar. 2012). "Estimated carbon dioxide emissions from tropical deforestation improved by carbon-density maps". In: *Nature Clim Change* 2.3. Number: 3 Publisher: Nature Publishing Group, pp. 182–185. ISSN: 1758-6798. DOI: 10.1038/nclimate1354. URL: https://www.nature.com/articles/nclimate1354 (visited on 10/13/2022).

Bouvet, Alexandre et al. (Mar. 1, 2018). "An above-ground biomass map of African savannahs and woodlands at 25m resolution derived from ALOS PALSAR". In: *Remote Sensing of Environment* 206, pp. 156–173. ISSN: 0034-4257. DOI: 10.1016/j.rse.2017.12.030. URL: https://www.sciencedirect.com/science/article/pii/S0034425717306053 (visited on 10/13/2022).

Brandt, Martin et al. (May 2018). "Satellite passive microwaves reveal recent climate-induced carbon losses in African drylands". In: *Nat Ecol Evol* 2.5. Number: 5 Publisher: Nature Publishing Group, pp. 827–835. ISSN: 2397-334X. DOI: 10.1038/s41559-018-0530-6. URL: https://www.nature.com/articles/s41559-018-0530-6 (visited on 11/03/2022).

Breiman, Leo (Oct. 1, 2001). "Random Forests". In: *Machine Learning* 45.1, pp. 5–32. ISSN: 1573-0565. DOI: 10.1023/A:1010933404324. URL: https://doi.org/10.1023/A:1010933404324 (visited on 11/25/2022).

Chaparro, David et al. (June 1, 2018). "L-band vegetation optical depth seasonal metrics for crop yield assessment". In: *Remote Sensing of Environment* 212, pp. 249–259. ISSN: 0034-4257. DOI: 10.1016/j.rse.2018.04.049. URL: https://www.sciencedirect.com/science/article/pii/S0034425718302062 (visited on 11/03/2022).

Chen, Jing M. and Josef Cihlar (Feb. 1, 1996). "Retrieving leaf area index of boreal conifer forests using Landsat TM images". In: *Remote Sensing of Environment* 55.2, pp. 153–162. ISSN: 0034-4257. DOI: 10.1016/0034-4257(95)00195-6. URL: https://www.sciencedirect.com/science/article/pii/0034425795001956 (visited on 01/16/2023).

Denman, Kenneth et al. (Jan. 2007). "Couplings Between Changes in the Climate System and Biogeochemistry". In: *Climate Change 2007: The Physical Science Basis*. Vol. 2007, pp. 499–587.

Dou, Yujie et al. (Feb. 1, 2023). "Reliability of using vegetation optical depth for estimating decadal and interannual carbon dynamics". In: *Remote Sensing of Environment* 285, p. 113390. ISSN: 0034-4257. DOI: 10.1016/j.rse.2022.113390. URL: https://www.sciencedirect.com/science/article/pii/S0034425722004965 (visited on 12/26/2022).

ESA (2017). *Land Cover CCI Product User Guide Version 2. Tech. Rep. (2017). Available at:* URL: maps.elie.ucl.ac.be/CCI/viewer/download/ESACCI-LC-Ph2-PUGv22.0.pdf.

Espinoza, Jhan-Carlo et al. (Mar. 1, 2022). "The new historical flood of 2021 in the Amazon River compared to major floods of the 21st century: Atmospheric features in the context of the intensification of floods". In: *Weather and Climate Extremes* 35, p. 100406. ISSN: 2212-0947. DOI: 10.1016/j.wace.2021.100406. URL: https :

//www.sciencedirect.com/science/article/pii/S2212094721000931 (visited on 01/30/2023).

Fan, Lei et al. (Sept. 2019). "Satellite-observed pantropical carbon dynamics". In: *Nat. Plants* 5.9. Number: 9 Publisher: Nature Publishing Group, pp. 944–951. ISSN: 2055-0278. DOI: 10.1038/s41477-019-0478-9. URL: https://www.nature.com/articles/s41477-019-0478-9 (visited on 11/23/2022).

Forkel, Matthias et al. (Jan. 11, 2019). "Emergent relationships with respect to burned area in global satellite observations and fire-enabled vegetation models". In: *Biogeosciences* 16.1. Publisher: Copernicus GmbH, pp. 57–76. ISSN: 1726-4170. DOI: 10.5194/bg-16-57-2019. URL: https://bg.copernicus.org/articles/16/57/2019/ (visited on 03/06/2023).

Frappart, Frédéric et al. (Jan. 2020). "Global Monitoring of the Vegetation Dynamics from the Vegetation Optical Depth (VOD): A Review". In: *Remote Sensing* 12.18. Number: 18 Publisher: Multidisciplinary Digital Publishing Institute, p. 2915. ISSN: 2072-4292. DOI: 10.3390/rs12182915. URL: https://www.mdpi.com/2072-4292/12/18/2915 (visited on 10/19/2022).

Friedlingstein, P. et al. (Dec. 2010). "Update on CO2 emissions". In: *Nature Geosci* 3.12. Number: 12 Publisher: Nature Publishing Group, pp. 811–812. ISSN: 1752-0908. DOI: 10.1038/ngeo1022. URL: https://www.nature.com/articles/ngeo1022 (visited on 11/11/2022).

Goldstein, Alex et al. (2013). *Peeking Inside the Black Box: Visualizing Statistical Learning with Plots of Individual Conditional Expectation.* DOI: 10.48550/ARXIV.1309.6392. URL: https://arxiv.org/abs/1309.6392.

Hastie, Trevor, Robert Tibshirani, and Jerome Friedman (2009). *The Elements of Statistical Learning.* 2nd ed. Section 10.13.2: Springer.

Houghton, R. A. et al. (Dec. 13, 2012). "Carbon emissions from land use and land-cover change". In: *Biogeosciences* 9.12. Publisher: Copernicus GmbH, pp. 5125–5142. ISSN: 1726-4170. DOI: 10.5194/bg-9-5125-2012. URL: https://bg.copernicus.org/articles/9/5125/2012/ (visited on 11/11/2022).

Joiner, J. et al. (Oct. 25, 2013). "Global monitoring of terrestrial chlorophyll fluorescence from moderate-spectral-resolution near-infrared satellite measurements: methodology, simulations, and application to GOME-2". In: *Atmospheric Measurement Techniques* 6.10. Publisher: Copernicus GmbH, pp. 2803–2823. ISSN: 1867-1381. DOI: 10.5194/amt-6-2803-2013. URL: https://amt.copernicus.org/articles/6/2803/2013/ (visited on 02/22/2023).

Kokoska, Stephen and Daniel Zwillinger (Mar. 29, 2000). *CRC Standard Probability and Statistics Tables and Formulae, Student Edition.* 0th ed. CRC Press. ISBN: 978-0-429-18146-7. DOI: 10.1201/b16923. URL: https://www.taylorfrancis.com/books/9781482273847 (visited on 11/26/2022).

Li, Wei et al. (Jan. 30, 2018). "Gross and net land cover changes in the main plant functional types derived from the annual ESA CCI land cover maps (1992–2015)". In: *Earth System Science Data* 10.1. Publisher: Copernicus GmbH, pp. 219–234. ISSN: 1866-3508. DOI: 10.5194/essd-10-219-2018. URL: https://essd.copernicus.org/articles/10/219/2018/ (visited on 11/04/2022).

"Chapter 10 - Leaf area index" (Jan. 1, 2020a). In: *Advanced Remote Sensing (Second Edition).* Ed. by Shunlin Liang and Jindi Wang. Academic Press, pp. 405–445. ISBN: 978-0-12-815826-5. DOI: 10.

1016/B978-0-12-815826-5.00010-6. URL: https://www.sciencedirect.com/science/article/pii/B9780128158265000106 (visited on 01/16/2023).

"Chapter 14 - Aboveground biomass" (Jan. 1, 2020b). In: *Advanced Remote Sensing (Second Edition)*. Ed. by Shunlin Liang and Jindi Wang. Academic Press, pp. 543–580. ISBN: 978-0-12-815826-5. DOI: 10.1016/B978-0-12-815826-5.00014-3. URL: https://www.sciencedirect.com/science/article/pii/B9780128158265000143 (visited on 01/16/2023).

Liu, Yi Y. et al. (2013). "Global vegetation biomass change (1988–2008) and attribution to environmental and human drivers". In: *Global Ecology and Biogeography* 22.6, pp. 692–705. ISSN: 1466-8238. DOI: 10.1111/geb.12024. URL: https://onlinelibrary.wiley.com/doi/abs/10.1111/geb.12024 (visited on 12/22/2022).

Liu, Yi Y. et al. (May 2015). "Recent reversal in loss of global terrestrial biomass". In: *Nature Clim Change* 5.5. Number: 5 Publisher: Nature Publishing Group, pp. 470–474. ISSN: 1758-6798. DOI: 10.1038/nclimate2581. URL: https://www.nature.com/articles/nclimate2581 (visited on 10/14/2022).

Loecher, Markus (Mar. 4, 2022). "Unbiased variable importance for random forests". In: *Communications in Statistics - Theory and Methods* 51.5. Publisher: Taylor & Francis _eprint: https://doi.org/10.1080/03610926.2020.1764042, pp. 1413–1425. ISSN: 0361-0926. DOI: 10.1080/03610926.2020.1764042. URL: https://doi.org/10.1080/03610926.2020.1764042 (visited on 03/13/2023).

Moesinger, Leander et al. (Feb. 2019). *The Global Long-term Microwave Vegetation Optical Depth Climate Archive VODCA*. DOI: 10.5281/zenodo.2575599. (Visited on 05/25/2023).

Moesinger, Leander et al. (Jan. 30, 2020). "The global long-term microwave Vegetation Optical Depth Climate Archive (VODCA)". In: *Earth System Science Data* 12.1. Publisher: Copernicus GmbH, pp. 177–196. ISSN: 1866-3508. DOI: 10.5194/essd-12-177-2020. URL: https://essd.copernicus.org/articles/12/177/2020/ (visited on 10/19/2022).

Molnar, Christoph (2022). *Interpretable Machine Learning: A Guide for Making Black Box Models Explainable*. 2nd ed. URL: https://christophm.github.io/interpretable-ml-book.

Moutinho, Paulo and Stephen Schwartzman (Jan. 2005). *Tropical Deforestation and Climate Change*.

Myneni, Ranga, Yuri Knyazikhin, and Taejin Park (2015). *MCD15A2H MODIS/Terra + Aqua Leaf Area Index/FPAR 8-day L4 Global 500m SIN Grid V006*. DOI: 10.5067/MODIS/MCD15A2H.006. URL: https://lpdaac.usgs.gov/products/mcd15a2hv006/ (visited on 01/20/2023).

Pedregosa, F. et al. (2011). "Scikit-learn: Machine Learning in Python". In: *Journal of Machine Learning Research* 12, pp. 2825–2830.

Poulter, B. et al. (Nov. 16, 2011). "Plant functional type mapping for earth system models". In: *Geoscientific Model Development* 4.4. Publisher: Copernicus GmbH, pp. 993–1010. ISSN: 1991-959X. DOI: 10.5194/gmd-4-993-2011. URL: https://gmd.copernicus.org/articles/4/993/2011/ (visited on 03/06/2023).

Rodríguez-Fernández, Nemesio J. et al. (July 30, 2018). "An evaluation of SMOS L-band vegetation optical depth (L-VOD) data sets: high sensitivity of L-VOD to above-ground biomass in Africa".

In: *Biogeosciences* 15.14. Publisher: Copernicus GmbH, pp. 4627–4645. ISSN: 1726-4170. DOI: 10.5194/bg-15-4627-2018. URL: https://bg.copernicus.org/articles/15/4627/2018/ (visited on 10/13/2022).

Saatchi, Sassan S. et al. (June 14, 2011). "Benchmark map of forest carbon stocks in tropical regions across three continents". In: *Proceedings of the National Academy of Sciences* 108.24. Publisher: Proceedings of the National Academy of Sciences, pp. 9899–9904. DOI: 10.1073/pnas.1019576108. URL: https://www.pnas.org/doi/full/10.1073/pnas.1019576108 (visited on 10/13/2022).

Schalie, R. van der et al. (Feb. 1, 2017). "The merging of radiative transfer based surface soil moisture data from SMOS and AMSR-E". In: *Remote Sensing of Environment* 189, pp. 180–193. ISSN: 0034-4257. DOI: 10.1016/j.rse.2016.11.026. URL: https://www.sciencedirect.com/science/article/pii/S0034425716304734 (visited on 10/27/2022).

Schlau-Cohen, Gabriela S. and Joseph Berry (Sept. 2015). "Photosynthetic Fluorescence, from Molecule to Planet". In: *Physics Today* 68.9, pp. 66–67. ISSN: 0031-9228. DOI: 10.1063/PT.3.2924. (Visited on 05/25/2023).

Schmidt, Luisa et al. (Mar. 16, 2023). "Assessing the sensitivity of multi-frequency passive microwave vegetation optical depth to vegetation properties". In: *Biogeosciences* 20.5. Publisher: Copernicus GmbH, pp. 1027–1046. ISSN: 1726-4170. DOI: 10.5194/bg-20-1027-2023. URL: https://bg.copernicus.org/articles/20/1027/2023/ (visited on 04/06/2023).

Virtanen, Pauli et al. (Mar. 2020). "SciPy 1.0: fundamental algorithms for scientific computing in Python". In: *Nat Methods* 17.3. Number: 3 Publisher: Nature Publishing Group, pp. 261–272. ISSN: 1548-7105. DOI: 10.1038/s41592-019-0686-2. URL: https://www.nature.com/articles/s41592-019-0686-2 (visited on 11/26/2022).

Vittucci, Cristina et al. (May 1, 2019). "Vegetation optical depth at L-band and above ground biomass in the tropical range: Evaluating their relationships at continental and regional scales". In: *International Journal of Applied Earth Observation and Geoinformation* 77, pp. 151–161. ISSN: 1569-8432. DOI: 10.1016/j.jag.2019.01.006. URL: https://www.sciencedirect.com/science/article/pii/S0303243418310316 (visited on 11/23/2022).

Walker, Anthony P. et al. (2021). "Integrating the evidence for a terrestrial carbon sink caused by increasing atmospheric CO2". In: *New Phytologist* 229.5. _eprint: https://onlinelibrary.wiley.com/doi/pdf/10.1111/nph.16866, pp. 2413–2445. ISSN: 1469-8137. DOI: 10.1111/nph.16866. URL: https://onlinelibrary.wiley.com/doi/abs/10.1111/nph.16866 (visited on 11/23/2022).

Wen, J. et al. (2021). *Global High-Resolution Estimates of SIF from Fused SCIAMACHY and GOME-2, 2002-2018*. DOI: 10.3334/ORNLDAAC/1864. URL: https://daac.ornl.gov/cgi-bin/dsviewer.pl?dsid=1864.

Werf, G. R. van der et al. (Nov. 2009). "CO2 emissions from forest loss". In: *Nature Geosci* 2.11. Number: 11 Publisher: Nature Publishing Group, pp. 737–738. ISSN: 1752-0908. DOI: 10.1038/ngeo671. URL: https://www.nature.com/articles/ngeo671 (visited on 10/13/2022).

Xu, Liang et al. (July 2, 2021). "Changes in global terrestrial live biomass over the 21st century". In: *Science Advances* 7.27. Publisher: American Association for the Advancement of Science, eabe9829. DOI: 10.1126/sciadv.abe9829. URL: https://www.science.org/doi/10.1126/sciadv.abe9829 (visited on 10/19/2022).

Zotta, Ruxandra-Maria et al. (2023, in preparation). *VODCA v2: An Improved Multi-Sensor and Frequency Vegetation Optical Depth Dataset for Long-Term Vegetation Monitoring (Preliminary Title).*